Doctoral Dissertation

High Efficiency Circularly Polarized Electroluminescence Induced by Sublimable Axially Chiral Inducers

YUAN Chenyuhe

Supervisor: MURATA Hideyuki

Graduate School of Advanced Science and Technology

Japan Advanced Institute of Science and Technology

[Materials Science]

Sept. 2025

Abstract

Organic light-emitting diodes (OLEDs) capable of emitting circularly polarized (CP) light have attracted significant interest from researchers due to their potential applications, such as 3D display and optical information storage. One of the effective approaches to fabricate CP-OLEDs is to construct chiral light-emitting layers by chiral induction, where chiral small molecules are doped as chiral inducers into achiral luminescent polymers. Due to the chiral transfer, strong circularly polarized luminescence (CPL) of the polymer can be achieved. While this method can yield high asymmetry factor g, the presence of chiral inducers within the films can decrease the device performance of the CP-OLEDs. To solve this problem, it may be important to remove the chiral inducers from polymer after chiral induction is complete.

In this study, we doped the axially chiral inducers into thin films of the achiral conjugated polymers. Upon annealing the films, a clear circular dichroism (CD) signal from emitting polymer appeared, indicating the induction of chiroptical properties. Nuclear magnetic resonance (NMR) spectra of the samples before and after annealing confirmed the complete removal of chiral inducers by sublimation during annealing, resulting in the formation of neat polymer films. The red shift in absorption spectra and the fibrous morphology in atomic force microscope (AFM) after annealing indicated that the chiroptical properties were caused by intermolecular exciton coupling due to aggregation. The photoluminescence quantum yield (PLQY) of as-prepared films was remarkably low but after annealing it increased to that of neat films, suggesting that the removal of chiral inducers by high-temperature sublimation realized both high g factor and PLQY simultaneously. We applied this thin film to the emitting layer of CP-OLEDs. The device achieved a maximum external quantum efficiency (EQE) of 1.20%, The $|g_{EL}|$ of 7×10^{-3} was achieved without any optimization of the device structures. This study demonstrates for the first time a way to realize CP-OLEDs by sublimable chiral inducers.

Furthermore, the generality of the sublimation-assisted chiral induction strategy was also investigated. We confirmed that BINOL is capable of inducing CPL not only in F8BT but also in PFO. Compared to F8BT, PFO exhibited a g_{lum} value one order of magnitude lower. In addition, the CPL emission of PFO could be further red-shifted after solvent vapor annealing, which induced the β-phase crystalline structure. The chiral F8BT system was further extended to realize circularly polarized Förster resonance energy transfer (C-FRET). By replacing BINOL with a more efficient chiral inducer, R5011, and doping the blend with a red-emitting molecule DBP as both the energy and chirality acceptor, red CPL emission was successfully achieved. Notably, we also discovered that R5011 contributed to a significant enhancement in the PLQY of the films. These studies provide a new method for the preparation of high-efficiency CP-OLEDs.

Keywords: Chiral induction, Circularly polarized organic light-emitting diodes, BINOL, Polyfluorene, Circularly polarized fluorescence resonance energy transfer.

Contents

List of Figures

List of Tables

Chapter 1
Introduction

Chirality is a property wherein an object cannot be superimposed on its mirror image, is exemplified by the asymmetry between left and right-handed.[1,2] As a fundamental characteristic of both nature and biological systems,[3–5] chirality also plays a critical role in a wide range of chemical and physical systems.[6,7] Chirality exists from subatomic particles to supramolecular assemblies, macroscopic objects, and even galactic formations.[6]

The scientific significance of chirality research lies primarily in two key aspects. First, from the biological perspective, all amino acids that constitute proteins in living organisms adopt the L-configuration, while the ribose that form the backbone of DNA and RNA are in the D-configuration. Investigating the origin of such homochirality is vital for deepening our understanding of the origin of life. Second, from the application perspective, chirality at the molecular and supramolecular levels shows potential in a variety of fields, including asymmetric catalysis, enantioselective separation, chiral recognition and circularly polarized luminescent materials.[8–10]

1.1 Introduction to circularly polarized light

Chiral light-emitting systems, including organic small molecules, polymers, or supramolecular assemblies, are capable of emitting asymmetrically polarized light known as circularly polarized (CP) light.[11] CP light comprises two orthogonal linearly polarized lights that possess a phase difference of quarter wavelength. As a result, the magnitude of the electric field vector remains constant, while its direction rotates helically over time. The sense of this rotation determines the handedness of the CP light: if the electric field vector rotates counterclockwise when viewed in the direction of propagation, the light is designated as left-handed circularly polarized (LCP); conversely, if the rotation is clockwise, it is referred to as right-handed circularly polarized (RCP).[12]

The emission of left- or right-handed circularly polarized light from chiral luminescent materials is referred to as circularly polarized luminescence (CPL). Owing to its unique optical characteristics, CPL holds significant potential for applications in diverse fields, such as quantum computing, 3D displays, and optical information storage.[13–16] A common method for generating CPL involves converting isotropic light into linearly polarized (LP) light using a polarizer, followed by transformation into CPL via a quarter-wave plate (Fig. 1.1). However, this approach inevitably leads to at least 50% optical flux loss, thereby limiting its practical efficiency.[17] In comparison, chiral

luminescent materials offer a more energy-efficient approach by directly emitting circularly polarized light upon excitation, eliminating the need for additional optical modulation.

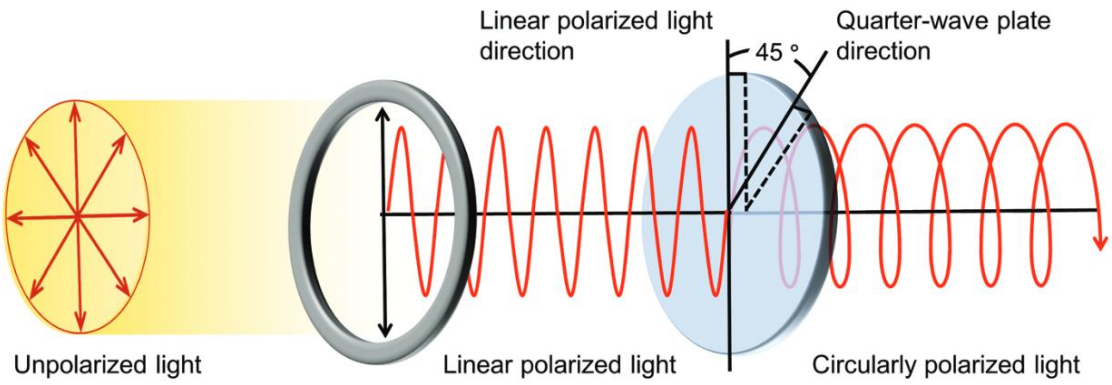

Fig. 1.1 The process of unpolarized light convers to CP light involves first passing it through a linear polarizer to produce linearly polarized light, which is then transformed into CP light using a quarter-wave plate. [17]

A fundamental characteristic of chiral luminescent materials is their chiroptical activity, which manifests in both light absorption and emission processes. These properties are typically characterized by circular dichroism (CD) spectroscopy for ground-state absorption, and CPL spectroscopy for excited-state emission.[18,19]

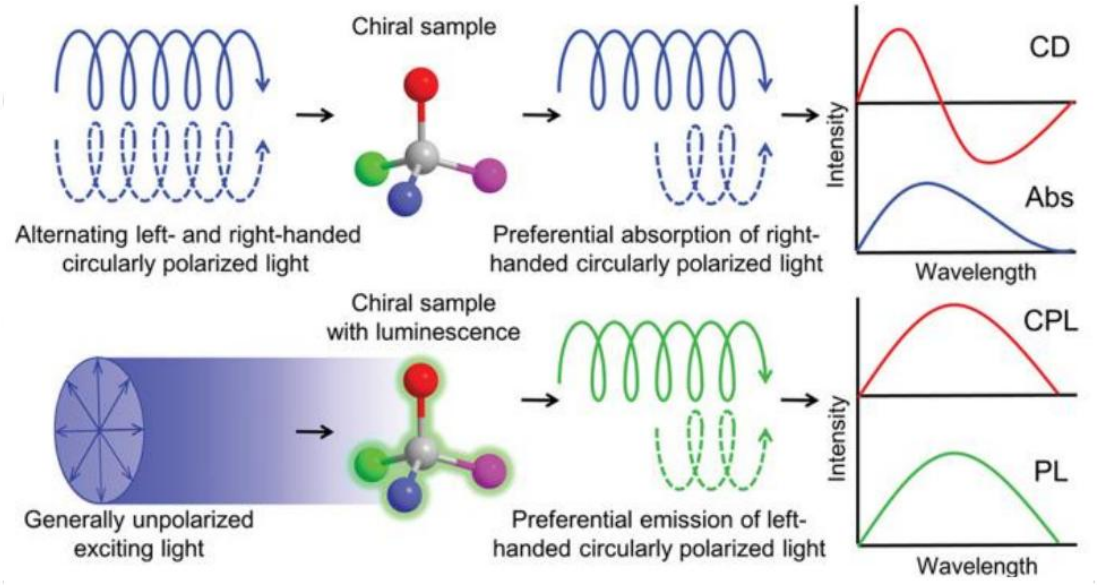

Fig. 1.2 The schematic diagram of CD and CPL measurements.[17]

CD spectroscopy probes the difference in absorption between LCP and RCP light, providing insight into the chiral structure of the ground state. When CP light passes through an optically active medium, the material exhibits differential absorption of LCP and RCP light, leading to CD signal (Fig. 1.2). The CD signal is defined as the differential absorbance:

$$\mathrm{CD} = A_L - A_R \tag{1-1}$$

Here, A_L and A_R represent the absorbance of LCP and RCP light, respectively. In most CD spectra, the difference in absorbance is typically expressed as the molar circular dichroism ($\Delta\varepsilon$) as a function of wavelength, where:

$$\Delta\varepsilon = \varepsilon_L - \varepsilon_R = \frac{\mathrm{CD}}{c*d} \tag{1-2}$$

Here, ε represents the molar extinction coefficient, c represents concentration, and d represents the optical path length. To further quantify the strength of chiroptical activity, the absorption asymmetric factor g_{abs} or g_{CD} is introduced:

$$g_{CD} = \frac{\varepsilon_L - \varepsilon_R}{1/2(\varepsilon_L + \varepsilon_R)} = 2\frac{\varepsilon_L - \varepsilon_R}{(\varepsilon_L + \varepsilon_R)} \tag{1-3}$$

For achiral materials, which absorb LCP and RCP light equally, g_{CD} equals to zero. In contrast, for ideal chiral materials with complete circular polarization selectivity, g_{CD} can theoretically reach +2 or –2.

CPL spectroscopy evaluates the difference in emission intensity of LCP and RCP light from the excited state (Fig. 1.2). This technique provides valuable information about the excited-state configuration of optically active molecules. The intensity of circular polarized emission can be quantified by the luminescence asymmetric factor g_{lum}, defined as:

$$g_{lum} = \frac{I_L - I_R}{1/2(I_L + I_R)} = 2\frac{I_L - I_R}{(I_L + I_R)} \tag{1-4}$$

Here, I_L and I_R represent the intensities of LCP and RCP light, respectively. The g_{lum} value of +2 corresponds to 100% left-handed CPL, whereas -2 corresponds to 100% right-handed CPL. A higher absolute value of $|g_{lum}|$ indicates better CPL performance.

Theoretically, g_{lum} is directly related to the vectorial relationship between the magnetic transition dipole (m) and electric transition dipole (μ) moments, as described by:

$$g_{lum} \cong 4\cos\theta \frac{|m||\mu|}{|m|^2+|\mu|^2} \quad (1\text{-}5)$$

Where θ represents the angle between m and μ. In systems where $|m| \ll |\mu|$, this can be simplified as:

$$g_{lum} \cong 4\cos\theta \frac{|m|}{|\mu|} \quad (1\text{-}6)$$

This equation indicates that g_{lum} is positively correlated with the magnitude of the magnetic dipole moment and inversely correlated with the electric dipole moment. Chiral lanthanide complexes often exhibit relatively high g_{lum} values due to their small electric dipole transitions. However, the parity-forbidden nature of their *f-f* transitions typically leads to low photoluminescence quantum yields, limiting their practical application. In contrast, organic luminophores generally exhibit much smaller $|m|$ compared to $|\mu|$, resulting in modest g_{lum} values. Moreover, high photoluminescence quantum yields (Φ) are usually associated with large electric dipole moments, since the radiative decay rate (kr) scales with $|\mu|^2$. Therefore, achieving simultaneously high g_{lum} and high Φ remains one of the major challenges in CPL materials research.

Since g_{lum} does not relate to emission efficiency, it is insufficient for evaluating the

overall performance of CPL materials in practical applications. A more comprehensive parameter luminescence brightness (B),[20] defined as the product of the molar extinction coefficient (ε_λ) at the excitation wavelength (λ) and the photoluminescence quantum yield (Φ):

$$B = \varepsilon_\lambda \times \Phi \tag{1-7}$$

To further evaluate CPL materials holistically, the CPL brightness (B_{CPL}) is defined as the product of brightness and the absolute value of g_{lum}, normalized by a factor of 2:

$$B_{CPL} = B \times \frac{|g_{lum}|}{2} = \varepsilon_\lambda \times \Phi \times \frac{|g_{lum}|}{2} \tag{1-8}$$

This parameter allows for a balanced assessment of both chiroptical intensity and emission efficiency of CPL-active materials.[21]

1.2 Introduction to organic light emitting diodes (OLEDs)

Organic light-emitting diodes (OLEDs) have been widely applied in display and lighting technologies, and they are good candidates for circularly polarized electroluminescence (CPEL). OLEDs are electroluminescent devices composed of multiple nanometer-scale organic thin films caught between a reflective metal cathode and a semi-transparent anode deposited on a transparent substrate (Fig. 1.3 a).[22] The

development of OLEDs has progressed significantly over the past decades, leading to the adoption of heterojunction multi-layer structures designed to optimize charge injection, transport, exciton formation, and recombination, thereby enhancing device efficiency and stability.[23]

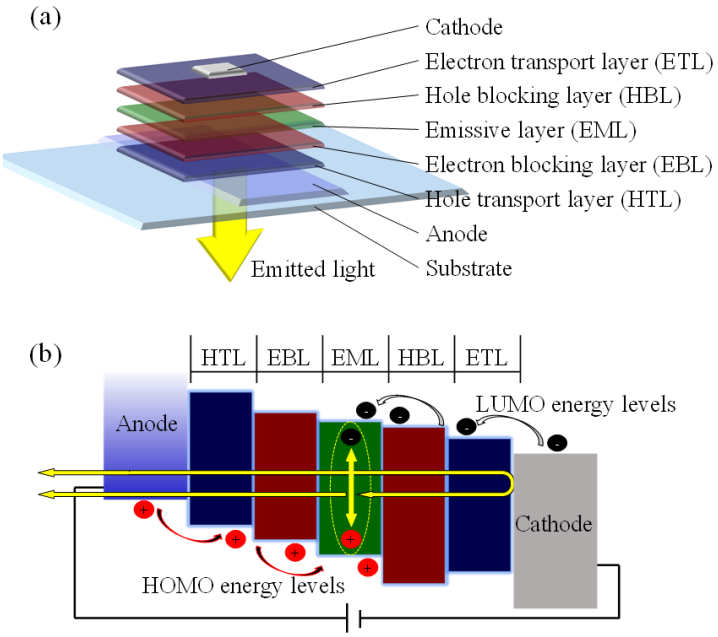

Fig. 1.3 Schematic illustration of (a) typical OLED architecture and (b) charge injection, transport, exciton generation, radiative recombination, and emission pathway.

As illustrated in Fig. 1.3 b, when a bias voltage is applied across the electrodes, holes are injected from the anode into the highest occupied molecular orbital (HOMO), while electrons are injected from the cathode into the lowest unoccupied molecular orbital

(LUMO).[24] These charge carriers are transported through hole transport layers (HTLs) and electron transport layers (ETLs) by hopping mechanisms, converging in the emissive layer (EML), where they recombine to form excitons. To ensure recombination occurs primarily within the EML, hole-blocking layers (HBLs) and electron-blocking layers (EBLs) are employed. The subsequent radiative decay of excitons results in the emission of photons, a portion of which escape into free space after passing through the semi-transparent electrode and substrate and being reflected by the metal cathode.[25]

External quantum efficiency (EQE or η_{ext}) is a critical parameter in OLED performance evaluation. It is defined as the ratio of the number of photons emitted in the forward viewing direction to the number of charge carriers injected into the device and can be expressed as:

$$\eta_{ext} = \eta_{int} \times \eta_{out} \tag{1-9}$$

Here, η_{int} represents the internal quantum efficiency, denoting the ratio of generated photons to injected electrons, while η_{out} represents the outcoupling efficiency, denoting the fraction of photons that escape from the device.[25–27] The internal quantum efficiency itself can be decomposed as:

$$\eta_{int} = \gamma \times \eta_{exc} \times \phi_{PL} \tag{1-10}$$

Where γ represents the charge balance factor, η_{exc} represents the exciton formation ratio for radiatively allowed states, and ϕ_{PL} represents the photoluminescence quantum yield (PLQY).[28–30] In practice, ϕ_{PL} is significantly influenced by the optical environment within the device due to microcavity effects, including the Purcell effect, which alters the radiative decay rate. To account for this, the effective photoluminescence efficiency (ϕ_{eff}) is introduced:

$$\eta_{ext} = \gamma \times \eta_{exc} \times \phi_{eff}(\phi_{PL}, \Gamma) \times \eta_{out}(\Theta, \Gamma) \tag{1-11}$$

Here, Γ represents the Purcell factor, which depends on parameters such as the emitter's spatial location within the cavity, its distance from the reflective electrode, and the local electric field distribution.

The outcoupling efficiency η_{out} is also affected by the orientation of the transition dipole moments (TDMs). The orientation factor Θ quantifies the fraction of horizontally aligned dipoles relative to the substrate plane, and can be described as:

$$\Theta = {p_{\parallel}}/{p_{\parallel} + p_{\perp}} \tag{1-12}$$

Here, $p_{\parallel}$ and $p_{\perp}$ represent the horizontal and vertical components of the emitting dipole, respectively.[28,31,32] Since emission from horizontally oriented dipoles couples more efficiently to optical modes that can escape the device, a higher Θ leads to increased

η_{out}.

Through advancements in materials and device engineering, internal quantum efficiencies approaching 100% have been achieved. Optimizing charge balance (γ) through tailored energy level alignment at electrode interfaces and mobility-matched transport layers enables near-unity charge recombination. The exciton formation ratio (η_{exc}) is determined by the nature of the emitter. Under electrical excitation, excitons are generated in a ratio of 1:3 between singlet and triplet states. Conventional fluorescent materials can only utilize singlet excitons, capping η_{exc} at 25%. In contrast, phosphorescent emitters, often based on metal-organic complexes, allowing both singlet and triplet excitons to emit radiatively, thereby achieving $\eta_{exc} \approx 100\%$.[33,34] High ϕ_{PL} (almost 100%) has been achieved in thermally activated delayed fluorescent (TADF) materials through the reverse intersystem crossing (RISC) mechanism that up-converts triplets to singlet excitons,[35,36] representing a significant advancement in the development of highly efficient OLED systems.

Despite the high η_{int}, the outcoupling efficiency remains a significant limiting factor. For conventional bottom-emitting OLEDs with a reflective cathode, isotropic dipole distribution, and no external light extraction structures, the outcoupling efficiency can be

approximated as:

$$\eta_{out} = 1 - \sqrt{1 - \left(\frac{1}{n_{org}^2}\right)} \approx \frac{1}{2n_{org}^2} \tag{1-13}$$

Here, n_{org} represents the refractive index of the emitting layer, typically ranging from 1.7 to 1.8 for organic semiconductors. This gives a theoretical maximum η_{out} of approximately 20%,[27,37–39] thus constraining the overall external quantum efficiency to this value even with perfect internal efficiency. Overcoming this bottleneck requires deliberate optical design and the integration of outcoupling enhancement strategies to approach the theoretical limits of OLED performance.

1.3 Introduction to circularly polarized OLEDs (CP-OLEDs)

Traditionally, CPL can be generated from unpolarized light by sequentially passing through a linear polarizer to produce linearly polarized light, which is then transformed into CP light using a quarter-wave plate (Fig. 1.1). However, this indirect optical approach inherently leads to significant loss of brightness and increased system complexity due to the added optical components.

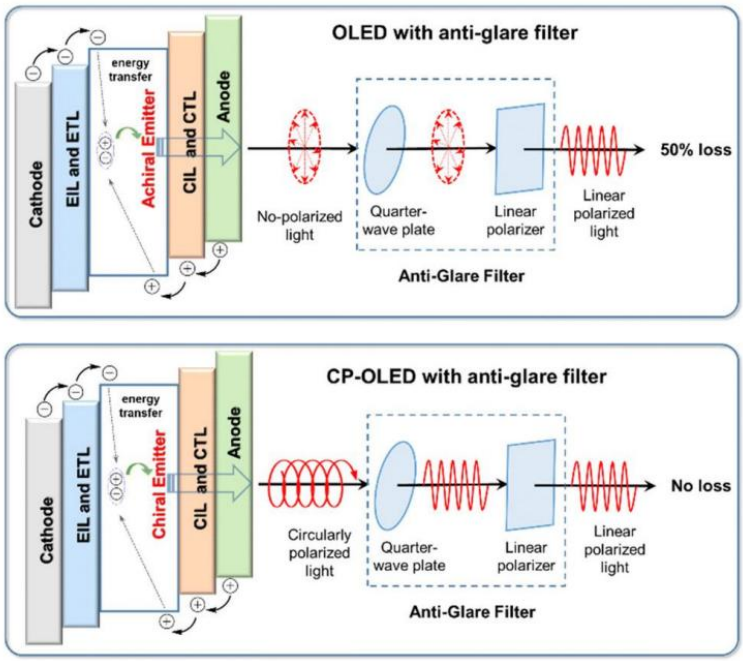

Fig. 1.4 Schematic diagram of conventional OLEDs and CP-OLEDs with the anti-glare filter.[40]

Notably, when the emitting layer is replaced by a chiral luminescent material, CPEL can be achieved intrinsically, eliminating the need for external optical modulation. In OLED displays, anti-glare filters are indispensable components, serving to suppress ambient light reflections and enhance display contrast. However, the inherently unpolarized emission from standard OLEDs leads to at least 50% energy loss when passing through these filters. CP-OLEDs equipped with anti-glare filters and intrinsically polarized emission can operate without additional energy loss (Fig. 1.4).[40] Therefore, the development of high-performance CP-OLEDs is practical for both energy-efficient and

polarization-selective optoelectronic applications.

The performance assessment of CP-OLEDs has two aspects: (1) the general electroluminescent device performance, and (2) the CPEL-specific characteristics.

The evaluation of general electroluminescent device performance is analogous to those of conventional OLEDs. The parameters include electroluminescence (EL) spectra, turn-on voltage (V_{on}), luminance, efficiency roll-off, current efficiency (η_{CE}), power efficiency (η_{PE}), and operational lifetime. The key parameter is EQE as mentioned in chapter 1.2. Luminance means the luminous intensity emitted per unit area (typically 2 mm × 2 mm). V_{on} means the voltage required to achieve a luminance of 1 cd m^{-2}. It is influenced by charge transport efficiency and the energy gap of the emitting material. Current density means the electric current passing through a unit area of the device per unit time. η_{CE} means the ratio between luminance and current density under a given operating condition.

To assess the CPEL-specific of devices and determine the electroluminescence asymmetric factor (g_{EL}), a common measurement setup involves placing a quarter-wave plate and a linear polarizer in sequence between the CP-OLED and the detector. The angle between the fast axis of the quarter-wave plate and the transmission axis of the linear

polarizer is typically set as 45° or 135°. Upon electric excitation, the emitted CPL is converted into linearly polarized light. By measuring the transmitted intensity before and after rotating the polarizer by 90°, I_L and I_R can be determined (Fig. 1.5).[41]

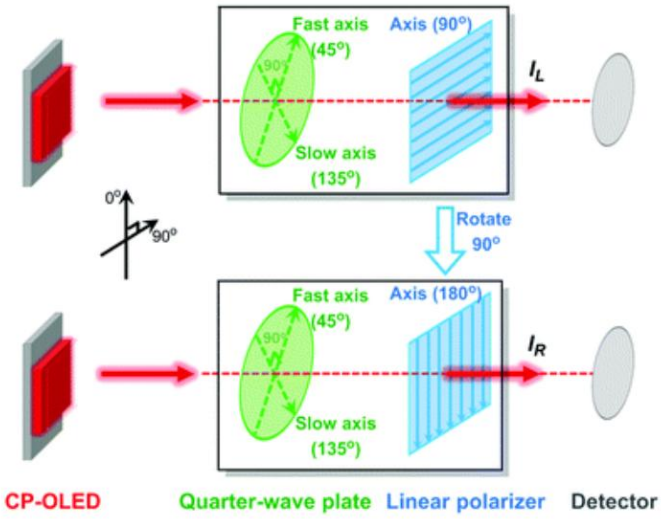

Fig. 1.5 Schematic diagram of CPEL measurement mechanism.[41]

The g_{EL} value is then calculated using the previously introduced equation:

$$g_{EL} = \frac{I_L - I_R}{1/2(I_L + I_R)} = 2\frac{I_L - I_R}{(I_L + I_R)} \quad (1\text{-}14)$$

Commercial instruments such as the CPL-300 spectrometers can be used for direct and precise CPEL measurements by vertically mounting the electrically driven device onto the measurement stage.

g_{EL} quantifies the degree of handedness in CPEL. A high g_{EL} value is desirable for applications requiring circularly polarized emission. Therefore, CP-OLEDs with both high device efficiency and strong CPEL activity is essential for commercial viability.

To comprehensively evaluate CPEL device performance, a practical figure of merit-referred to as the Q-factor-has been introduced. It is defined as the product of the external quantum efficiency and the absolute value of the electroluminescence asymmetric factor:

$$Q = |EQE \times g_{EL}| \tag{1-15}$$

The Q-factor serves as a single parameter that captures both brightness efficiency and chiroptical intensity. Theoretically, for an ideal CP-OLED with EQE=1 and $|g_{EL}|$=2, the Q-factor would reach a maximum of 2, providing a benchmark for future material and device design.

1.4 Methods to realize CPEL

A common method to realize CP-OLEDs is to construct the light-emitting layer of chiral luminescent materials. Luminescent materials encompass several systems, including conjugated polymers, metal complexes and organic small molecules. To endow these materials with chiroptical activities, the incorporation of chirality is typically

required.

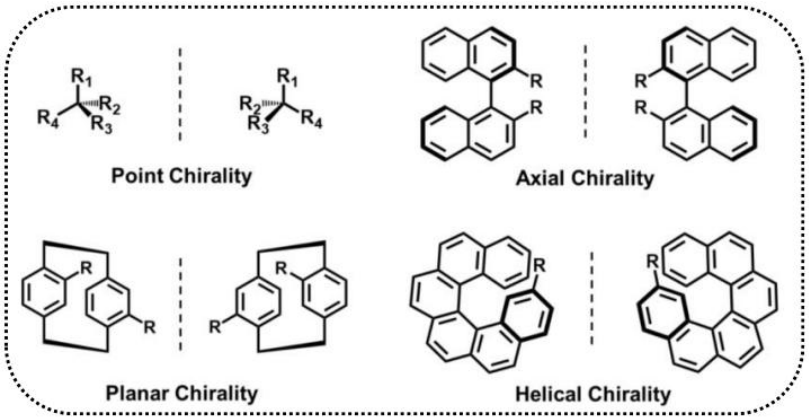

Fig. 1.6 Schematic diagram of four common chirality: point, axial, planar and helical chirality.[42]

CPL-active molecules can be categorized into four classes: point, axial, planar and helical chirality (Fig. 1.6).[42] Each of these chiral motifs imposes unique stereochemical constraints on the molecular structure, influencing the polarization characteristics of the emitted light.

Several strategies have been developed to introduce chirality into emissive layers, including direct chemical synthesis of chiral emitters, construction of chiral frameworks, and chiral induction methods. These approaches offer diverse pathways to achieve CPL and have been extensively explored in the design of high-performance CPEL.

1.4.1 Chemical synthesis of luminescent chiral molecules

Chemical synthesis is a common strategy to introduce chirality into organic molecules, including chiral small molecules and chiral conjugated polymers. Compared with chiral polymers and chiral metal complexes, chiral organic small molecules offer several advantages such as structural tunability, synthetic accessibility, high PLQY, solution processability, and the absence of costly metal components. These features make them attractive candidates for developing metal-free, low-cost, and efficient CP-OLEDs.

Dhbaibi *et al.*[43] reported a series of novel "push-pull" type 2,15-dialkynyl-substituted helicene derivatives based on chiral carbo[6]helicenes. In these systems, the extended conjugated helicene core can act either as electron donors or acceptors. Experimental results and theoretical studies confirmed that the relative orientation between the electric and magnetic transition dipole moments in the excited state is a critical factor governing CPL intensity. Optimal orientation was achieved when the substituents on the helicene scaffold exhibited weak electron-donating or -withdrawing characteristics, leading to a g_{lum} value as high as 3-4 × 10^{-3}. Top-emitting CP-OLEDs fabricated via vacuum deposition exhibited g_{EL} of approximately 8 × 10^{-4}.

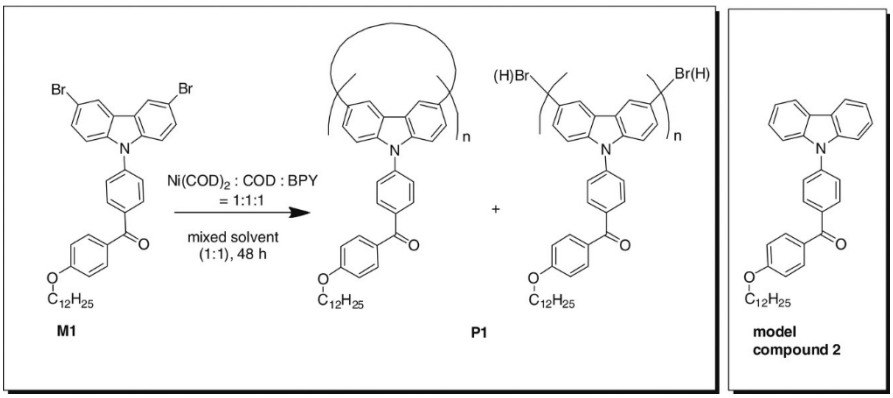

Fig. 1.7 The synthesis process of polymer P1 and the structure of model compound 2.[44]

TADF materials are particularly attractive for CPEL applications due to their potential to achieve theoretical internal quantum efficiencies (IQEs) of 100%, provided that the energy gap (ΔE_{ST}) between the lowest singlet and triplet states is sufficiently small. This allows RISC to efficiently up-convert non-radiative triplets into emissive singlet excitons.[44] Recent advances in TADF-based CPEL emitters have primarily relied on chiral perturbation strategies, often involving point chirality or axial chirality. In contrast, Zhang *et al.*[45] proposed a novel donor–planar chiral–acceptor (D–π–A*) design concept. They synthesized a pair of TADF enantiomers, R/S-PXZ-PT, by introducing donor and acceptor units at the 4,7-positions of a [2.2] paracyclophane core. This molecular design successfully suppressed racemization caused by σ-bond rotation during vacuum deposition, resulting in robust CPL activity, with $|g_{PL}|$ reaching 1.9×10^{-3}. CP-OLEDs

based on R/S-PXZ-PT demonstrated high performance, with a EQE_{max} of 20.1%, current efficiency of 48.4 cd A^{-1}, and a $|g_{EL}|$ value of 1.5×10^{-3} at 557 nm.

Despite their potential, most chiral small molecules exhibit very weak CPL activity, with typical g_{lum} ranging from 10^{-5} to 10^{-3}. Chiral conjugated polymers were gradually selected as candidates for CPEL applications, due to their excellent thermal stability, low cost, and ease of processability.

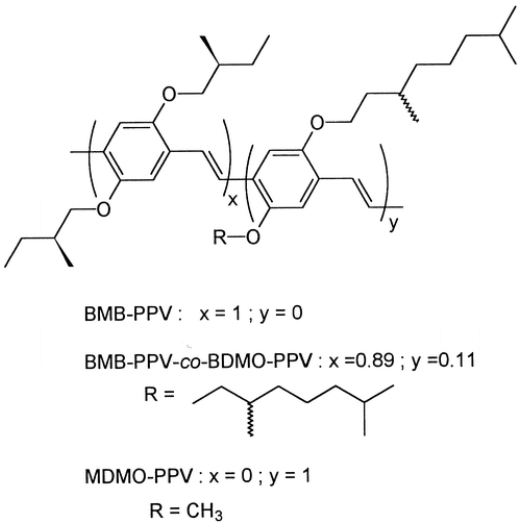

Fig. 1.8 Structure of PPV polymers with chiral alkyl side chains.[46]

To directly achieve CPEL from CP-OLEDs using conjugated polymers, Peeters *et al.*[46] first reported poly(p-phenylenevinylene) (PPV)-based polymers functionalized with chiral alkyl side chains (Fig. 1.8). The enantiomers of BMB-PPV exhibited both CD and

CPL in 1,2-dichlorobenzene solution, accompanied by aggregation phenomena. While no CPL was observed in the conventional MDMO-PPV, incorporation of the chiral side chain in BMB-PPV induced chirality in the copolymer BMB-PPV-co-BDMO-PPV, improving its solubility and enabling CP-OLED fabrication. Devices using this copolymer as the emissive layer displayed CP-EL emission with a maximum g_{EL} of 1.7×10^{-3}, thus creating a new path for solution-processed CP-OLEDs, although the overall device performance was modest.

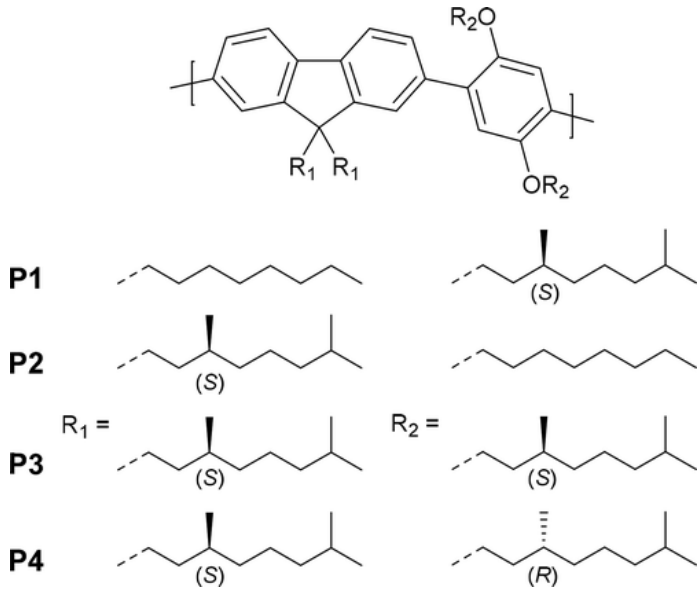

Fig. 1.9 Chemical structures of polyfluorene copolymers P1-P4.[47]

In 2019, Kulkarni *et al.* developed a series of copolymers P1-P4 based on fluorene and dialkoxyphenyl derivatives (Fig. 1.9).[47] The influence of the configuration and

position of side chains on the liquid crystalline order and chiroptical properties was systematically studied. Among these, P2-P4 exhibited strong CPL signals after thermal annealing, with g_{lum} of 0.33, 0.62, and 0.30, respectively. These results demonstrated that chiral alkyl side chains on the fluorene units was critical for forming ordered cholesteric liquid crystalline films and enhancing CD and CPL. CP-OLEDs fabricated from P2–P4 via solution processing showed distinct CP-EL. Notably, the P2-based device achieved a g_{EL} of ~0.2 at 400 nm, although device brightness and efficiency remained limited.

Another important class of chiral conjugated polymers is based on polyfluorene backbones, which differ significantly from the earlier PPV derivatives reported by Meijer in 1997. These differences include: (1) the presence of thermotropic liquid crystallinity in the main chain, (2) the ability to form helical conformations, and (3) a dramatic enhancement of CD and CPL signals upon thermal annealing.[48] Such properties favor the realization of high g_{lum} in the solid state.

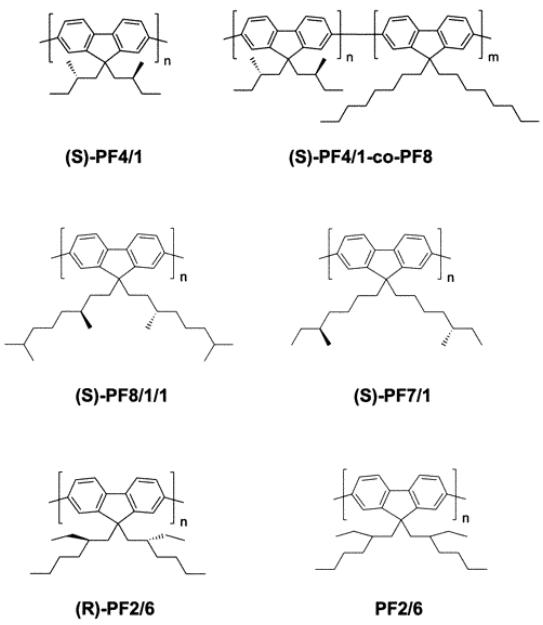

Fig. 1.10 Chemical structures of polyfluorenes with chiral side chains.[49]

Neher *et al.* reported a series of polyfluorene derivatives functionalized with chiral side chains.[49] CD signals became evident only after annealing at 200 °C. Interestingly, despite both (S)-PF4/1 and (S)-PF4/1-co-PF8 sharing S-configured side chains, they exhibited opposite CD signs, suggesting a parity (odd-even) effect, possibly linked to the distance between the chiral center and the main chain. CP-OLEDs based on these materials demonstrated promising g_{EL} values of 0.16 for (S)-PF4/1, 0.25 for (S)-PF8/1/1, and 0.25 for (S)-PF7/1.

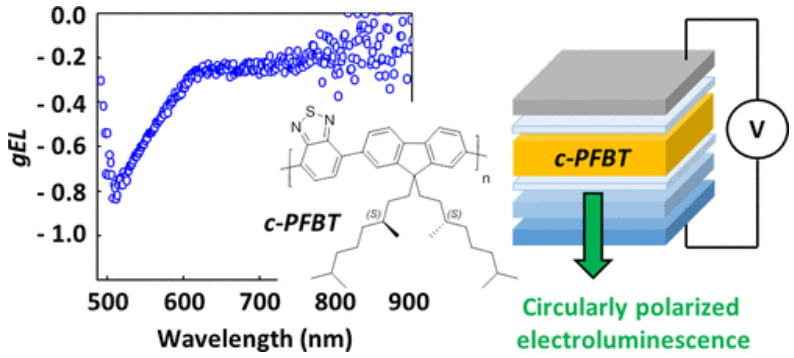

Fig. 1.11 Schematic diagram of the molecular structure and device of c-PFBT and the g_{EL} results.[50]

Nuzzo *et al.*[50] developed a donor-acceptor type chiral polyfluorene, c-PFBT, bearing chiral side chains. CP-OLEDs were fabricated using c-PFBT films of various thicknesses (100-400 nm) as the emitting layer (Fig. 1.10). Mueller matrix ellipsometry revealed strong optical anisotropy in annealed c-PFBT films, suggesting that the observed CPL originated primarily from selective scattering and birefringence associated with the film's intrinsic alignment. By adjusting the EML thickness and applying pulsed voltages, the authors achieved enhanced CP-EL with g_{EL} values as high as 0.8. However, due to the unusually thick EML, the device suffered from poor electrical performance, with a maximum luminance of only 80 cd m^{-2}.

1.4.2 Chiral framework

The construction of intrinsically chiral molecular frameworks represents an effective strategy for developing CPL materials. Among the various emitters, lanthanide (Ln) complexes have long been an important part of CPL research, owing to their unique coordination chemistry and exceptional photophysical properties. These include well-defined molecular structures, narrow-band emissions, long excited-state lifetimes, emission tunability across the visible spectrum, and even magnetic functionalities.[51,52] Due to the parity-forbidden nature of *f-f* transitions, which are electric dipole forbidden but magnetic dipole allowed, lanthanide complexes typically exhibit low absorption coefficients and low radiative rates. However, these same transitions confer relatively high g_{lum}, typically in the range of 0.05 to 0.5,[53,54] making them ideal candidates for chiroptical applications despite their historically low PLQY and labile coordination geometries.[55]

Zhou *et al.*[53] reported the synthesis of enantiomeric tetrahedral lanthanide cages Eu_4L_4[(R/S)-BINAPO]$_4$. These cages exhibited strong CPL activity, with a maximum g_{lum} of 0.2 at 592 nm and a high QY of 81% in $CHCl_3$. Moreover, the complex still exhibited a PLQY of 68% and a g_{lum} of 0.11.

1.4.3 Chiral induction

Beyond chemical synthesis and chiral framework, chiral induction is another effective alternative strategy for achieving CPEL, involves doping achiral conjugated polymers with chiral inducers. This method offers notable advantages, including synthetic simplicity, diverse material compatibility, and scalability, making it highly promising for practical CP-OLEDs fabrication.

Among emitting polymers, poly(9,9-dioctylfluorene) (PFO), poly[(9,9-dioctylfluorene-alt-benzothiadiazole)] (F8BT), and other fluorene-based derivatives have demonstrated excellent charge-carrier mobility and thermotropic liquid crystalline behavior at elevated temperatures. These features render them particularly suitable as emissive layers (EMLs) in OLEDs.[56] Blending such polymers with chiral inducers provides a pathway to realize CP-OLEDs combining strong chiroptical activity and favorable electronic performance.

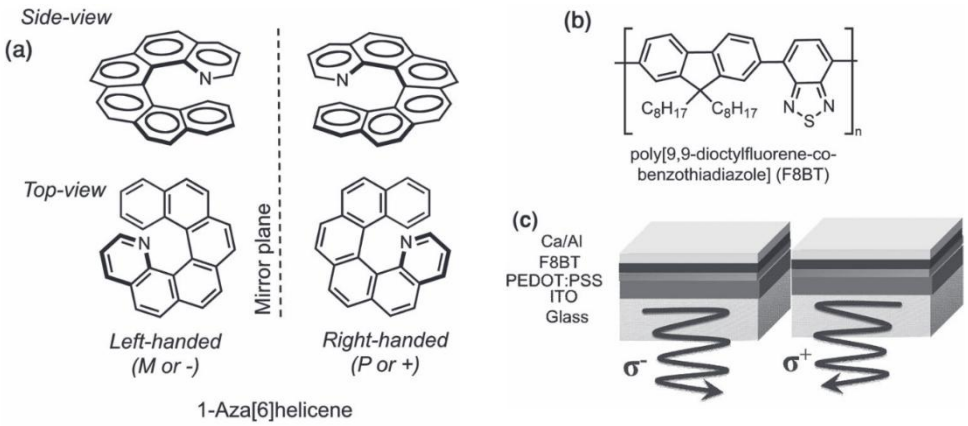

Fig. 1.12 (a) Molecular structures of 1-aza[6]helicene and (b) Molecular structures of F8BT. (c) Single-layer PLED device structure consisting of a 1-aza[6]helicene-doped F8BT emitting layer.[57]

Yang *et al.*[57] reported CP-OLEDs based on the chiral induction of F8BT by doping with helicene (Fig. 1.12). When 1-aza[6]helicene was blended into F8BT at a weight ratio of 7%, the resulting CP-OLEDs displayed a $|g_{EL}|$ value up to 0.2. In a subsequent study,[58] they investigated the influence of EML thickness on the CPL response. Notably, a sign inversion in g_{lum} was observed as the EML thickness increased from 100 nm to 200 nm. Specifically, g_{lum} decreased from +0.35 to 0 near 120 nm, and then reversed to –0.35 at 200 nm. A corresponding sign inversion in g_{EL} was also observed, with a peak g_{EL} of –1.05 at 160 nm thickness. While early CP-OLEDs achieved high g_{EL} values, their brightness and efficiency remained poor.

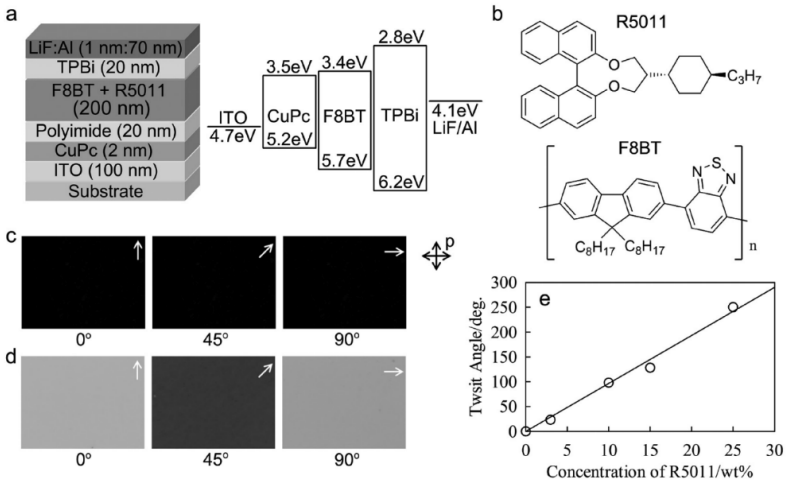

Fig. 1.13 Schematic diagram of CP-OLED structure and molecular structure for F8BT and R5011. The twist angle increased with the blending concentration of R5011.[59]

In another study, Lee *et al.*[59]used a strongly twisted chiral small molecule (R5011) as an inducer to create a chiral emissive blend with F8BT (Fig. 1.13). The resulting CP-OLEDs exhibited an exceptionally high g_{EL} of 1.13, attributed to the helical stacking of F8BT induced by R5011. Computational analysis revealed that the key parameters affecting high g_{lum} and g_{EL} in such systems include delayed emission (related to film thickness), torsion angle, and degree of linear polarization. Additionally, they found the position of recombination zone within the EML is a critical factor contributing to differences between CPL and CPEL. This design led to a 60% improvement in luminous efficiency.

Jung *et al.* further investigated the role of the recombination zone position on g_{EL}.[60] By tuning the thickness of the electron injection TPBi, they shifted the recombination zone toward the cathode and enhanced g_{EL}. However, excessive TPBi thickness (e.g. 50 nm) caused a decrease in g_{EL} due to parasitic emission from unpolarized TPBi. The ratio of unpolarized to polarized intensity, along with the spectral overlap between TPBi

and EML, was used to quantitatively describe this trade-off, providing a new route to optimize g_{EL} and directly probe recombination zone dynamics.

In addition to chemical doping, external physical stimuli can also induce chirality in otherwise achiral conjugated polymers. Polyfluorene derivatives exhibit thermotropic liquid crystalline phases and possess unstable chain conformations in the solid state, making them susceptible to structural perturbation by external fields. Cheng *et al.*[61] irradiated films of achiral F6BT with LCP or RCP light, triggering a transformation into a supramolecular chiral helical conformation (Fig. 1.14). The handedness and strength of the resulting CPL were dependent on the wavelength and polarization direction of the incident CPL. Devices fabricated using the irradiated F6BT films yielded CP-OLEDs with $|g_{EL}| = 4.16 \times 10^{-3}$, confirming the viability of photoinduced chiral induction as a strategy for CPEL materials.

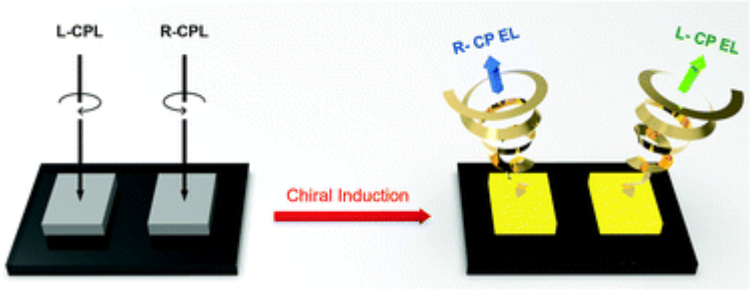

Fig. 1.14 The schematic diagram of CP light triggered CPEL.[61]

1.5 Issues in chiral induced CPEL

Chiral induction is a convenient and efficient approach to construct the emitting layer of CP-OLEDs by mixing achiral luminescent polymers with chiral small molecules, where the polymer luminescence can be affected by the chiral inducer to form CPL.[62] While this method can obtain high asymmetry factors, achieving high device performance still facing challenges.[57,59] Yang *et al.* reported $|g_{EL}|$ above 1.05 using F8BT and chiral inducer 1-[aza]H, but the device performance was significantly limited with EQE lower than 1%.[57,58] Despite their efforts to optimize device structure and dope ionic liquids, the performance remained inferior to that of neat F8BT OLEDs due to the chiral inducer aggregated close to the hole injection interface and acted as hole traps.[63–66] Zhang *et al.* attempted to improve device performance by modifying chiral inducers to enhance the hole injection, but this approach resulted in relatively low asymmetry factors of 10^{-2} level.[67,68]

If the chiral inducer can be effectively removed after chiral induction, its impact on device performance can be minimized. In our previous research[69], we reported that the axially chiral inducer BINOL could induce CD signal of F8BT, and BINOL was sublimated during the annealing process. This provides a viable approach for eliminating chiral inducers from the emitting layer.

1.6 Aims of research

This study aims to find a way to realize CP-OLEDs by sublimable chiral inducers to avoid the negative impact of chiral inducers on the device performance.

In chapter 2, we choose BINOL as the chiral inducer to induce the chiroptical properties of F8BT. After optimizing the experimental conditions to get the strongest CD and CPL signal, we explained the mechanism of chiral induction combined with the aggregation structure. Finally, we studied the influence of PLQY after the sublimation of chiral inducer.

In chapter 3, we applied these chiral-induced F8BT films as the emitting layer of CP-OLEDs to realize high efficiency CPEL with the similar EQE to that of devices based on neat F8BT.

In chapter 4, we applied BINOL to induce chiroptical signals in other polyfluorene derivatives, such as PFO. Solvent vapor exposure also be used to change the crystal phase of PFO.

In chapter 5, The chiral F8BT system was further extended to realize circularly polarized Förster resonance energy transfer (C-FRET). By replacing BINOL with a more

efficient chiral inducer, R5011, and doping the blend with a red-emitting molecule DBP as both the energy and chirality acceptor, red CPL emission was successfully achieved. Notably, we also discovered that R5011 contributed to a significant enhancement in PLQY.

Chapter 2
CPL of F8BT induced by BINOL

2.1 Introduction

CPL has attracted growing attention in recent years due to its potential applications in diverse fields. A practical and efficient strategy to realize CPL involves blending achiral emitting polymers with chiral small-molecule additives, which serve as chiral inducers. Among various emissive materials, F8BT has emerged as a promising candidate for application in chiroptical light-emitting layers, as its chiroptical activity can be effectively induced through such chiral induction methods. In this chapter, we applied the commercially available binaphthyl derivatives BINOL as the chiral inducer to interact with F8BT in thin films. BINOL, as the raw material of BINOL derivatives, can avoid the complicated chemical synthesis process. Upon annealing the films, the CD signal associated with BINOL disappeared and the clear CD and CPL signal from F8BT appeared, indicating the induction of chiroptical properties in F8BT.

NMR spectra before and after annealing confirmed the complete removal of BINOL by sublimation during annealing, resulting in the formation of pure F8BT films. PLQY of as-prepared F8BT/BINOL films was remarkably low but after annealing it increased

to that of pure F8BT films, suggesting that the removal of chiral inducers by high-temperature sublimation realized both high g factor and PLQY simultaneously.

The red shift of F8BT in absorption spectra and the fibrous morphology in AFM after annealing indicated that the chiroptical properties of F8BT were caused by intermolecular exciton coupling due to J-aggregate.

2.2 Experimental section

2.2.1 Experimental materials

R/S-BINOL (purity > 99%, Fig. 2.1a and 2.1b) were purchased from Tokyo Chemical Industry. F8BT (Mn < 25,000, Fig. 2.1c) and polymethyl methacrylate (PMMA; Mn = 46,000, Mw = 97,000) were purchased from Sigma-Aldrich. Toluene (purity > 99.9%) was purchased from Kanto chemical. All materials and reagents were used without further purification.

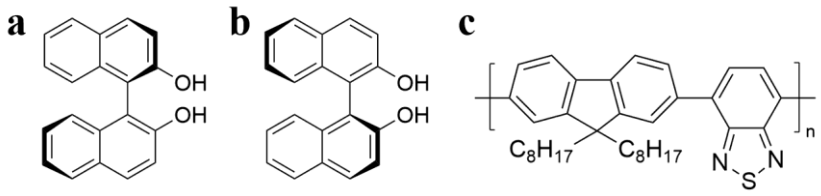

Fig. 2.1 Chemical structures of (a) R-BINOL, (b) S-BINOL and (c) F8BT.

2.2.2 Sample preparation

F8BT/BINOL blend solutions were prepared at concentrations of 10 mg/mL and 20 mg/mL, with BINOL doping levels ranging from 10 wt% to 50 wt% relative to F8BT. The solutions were stirred at 80 °C for 12 hours to ensure complete dissolution. Thin films were fabricated by spin-coating 100 μL of the solution onto quartz substrates at a spin speed of 1000 rpm for 90 s. The resulting film thicknesses were approximately 60 nm for the 10 mg/mL solution and 150 nm for the 20 mg/mL solution. Thermal annealing was performed at various temperatures ranging from 100 °C to 220 °C using both an oven and a hot plate.

For comparison, PMMA/R-BINOL thin films were prepared following the same procedure, except that F8BT was replaced with PMMA and the concentration of R-BINOL was fixed at 25 wt%.

2.2.3 Characterization instruments

CD spectra were recorded using a JASCO J-820 CD spectrometer, with UV–Vis absorption spectra acquired simultaneously during the measurements. CPL spectra were

measured using a JASCO CPL-300 spectrometer. Proton nuclear magnetic resonance (^{1}H NMR) spectra were obtained using a Bruker Avance III 400 MHz spectrometer with DMSO-d_6 as the solvent. Surface morphologies of thin films were analyzed via atomic force microscopy (AFM; Hitachi AFM5100N/5000II) operated in dynamic-force mode with a silicon cantilever under ambient conditions. Phase images were captured in tapping mode. PLQY was measured using an absolute PL quantum yield measurement system (Hamamatsu C9920-02).

2.2.4 Calculation of asymmetric factor g

The asymmetric factor g_{CD} indicates the different absorption capacity of LCP and RCP light of the sample. The fundamental principle is based on the differential absorption (ΔA) of LCP and RCP light, defined as:

$$\Delta A = A_L - A_R = \log (I_R/I_L) \quad (2\text{-}1)$$

Here, A_L and A_R represent the absorbance of LCP and RCP light, respectively; I_L and I_R represent the transmitted light intensities. This difference in molar absorption coefficients, denoted as $\Delta\varepsilon$, can be related to the molar ellipticity [θ] through the following expression:

$$[\theta] = 32982 \times \Delta\varepsilon \tag{2-2}$$

Here, $\Delta\varepsilon$ represents the molar absorption coefficients for LCP and RCP light, respectively. To evaluate the relative magnitude of CD at a particular wavelength, the absorption asymmetric factor g_{CD} is also defined as the ratio of $\Delta\varepsilon$ to the average unpolarized molar absorption coefficient ε:

$$g_{CD} = \frac{\Delta\varepsilon}{\varepsilon} = \frac{\varepsilon_L - \varepsilon_R}{(\varepsilon_L + \varepsilon_R)/2} \tag{2-3}$$

Experimentally, g_{CD} can also be calculated using the ellipticity θ and the absorbance A obtained from CD spectroscopy, based on the following equation:

$$g_{CD} = \frac{\theta/32980}{A} \tag{2-4}$$

While CD reflects the chiral activity in the ground state, CPL provides insight into the chiral nature of the excited state. The intensity of CPL is quantified by asymmetric factor g_{lum}, defined as:

$$g_{lum} = \frac{I_L - I_R}{1/2(I_L + I_R)} = 2\frac{I_L - I_R}{(I_L + I_R)} \tag{2-5}$$

Here, I_L and I_R represent the emission intensities of LCP and RCP light, respectively. g_{lum} can be obtained directly through CPL-300.

2.3 Results and discussion

2.3.1 CD signal of F8BT induced by BINOL and the sublimation of BINOL

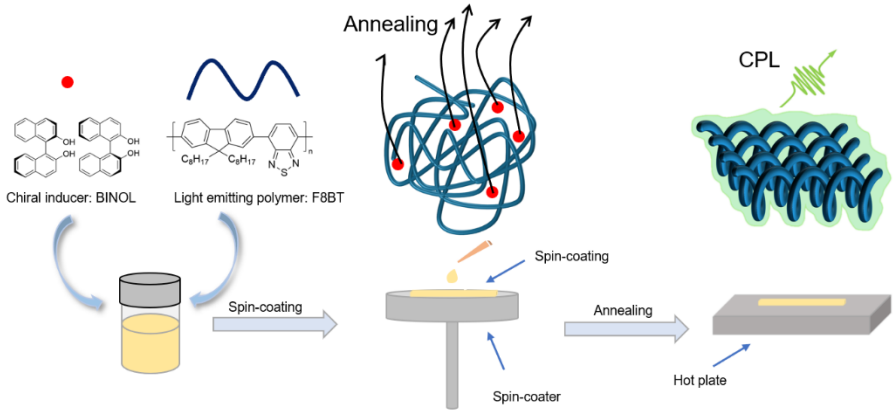

Fig. 2.2 Experimental schematic of chiroptical signals of F8BT was induced by BINOL through annealing.

As shown in Fig. 2.2, F8BT/BINOL films were prepared by spin-coating and the chiroptical signal of F8BT was induced by BINOL through an annealing process. Figure 2.3a presents CD and UV–Vis absorption spectra of thin films composed of F8BT/R-BINOL, F8BT/S-BINOL, and neat F8BT, measured before and after annealing at 140 °C for 10 minutes in an oven. In these figures, dashed lines represent spectra obtained before annealing, while solid lines correspond to those after annealing. The concentration of BINOL in the blend films was fixed at 20 wt%. Figure 2.3b shows the CD spectra of

PMMA films doped with R- and S-BINOL, along with the UV – Vis absorption spectrum of the PMMA/R-BINOL film.

By comparing the CD spectra of F8BT/BINOL and PMMA/BINOL systems, it is evident that the CD signals below 350 nm originate from BINOL. Prior to annealing, no CD signal attributable to F8BT was observed. However, after thermal treatment, new CD signals emerged at 215 nm, 345 nm, and 475 nm, corresponding well with the UV–Vis absorption peaks at 207 nm, 323 nm, and 467 nm, respectively. These results indicate that thermal annealing facilitates chiral induction in the F8BT matrix.[57] The CD spectra confirm that BINOL functions effectively as a chiral inducer for F8BT upon thermal annealing.

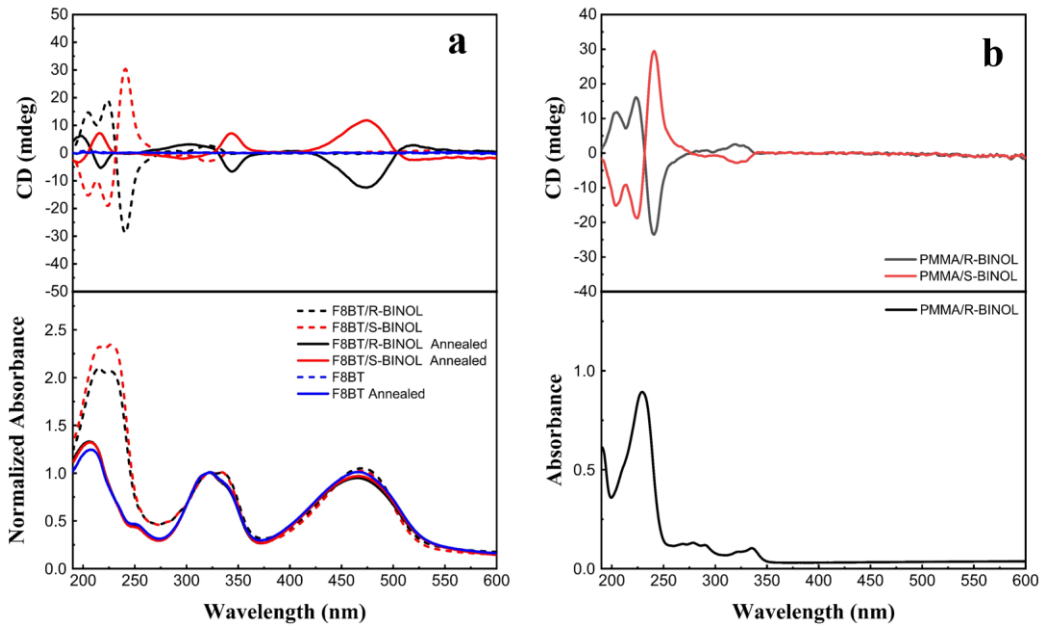

Fig. 2.3 CD and UV-Vis absorption spectra of thin films: (a) F8BT/R-BINOL, F8BT/S-BINOL, and neat F8BT before and after annealing at 140 °C for 10 minutes in oven, and (b) PMMA/R-BINOL and PMMA/S-BINOL.

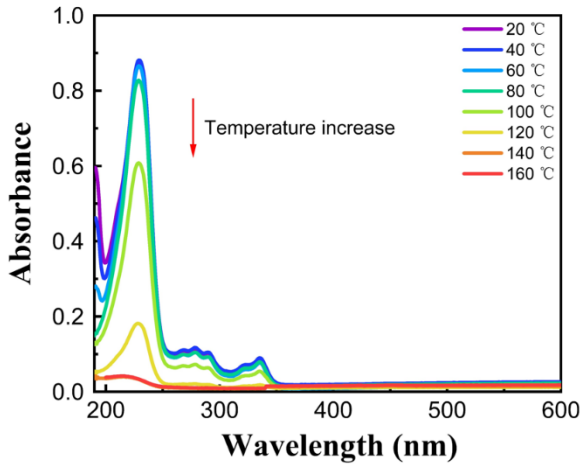

Fig. 2.4 UV-Vis absorption spectra of R-BINOL doped PMMA films after annealing at different temperatures for 10 minutes.

Table 2.1 Relative peak intensity at 230 nm in the UV-Vis absorption spectra of PMMA/R-BINOL thin films before and after annealing at various temperatures.

Annealing temperatures	Unannealed	80 °C	100 °C	120 °C	140 °C
UV-Vis intensity (230 nm)	100%	94%	69%	20%	3.7%

Another noteworthy observation is the disappearance of characteristic absorption peaks of BINOL in both the CD and UV-Vis absorption spectra after annealing at 140 °C for 10 minutes. Because the BINOL absorption peak around 230 nm overlaps with that of F8BT at 207 nm, it is difficult to precisely quantify the change in peak intensity during the annealing process from the blended films alone. To clarify this phenomenon, we measured the UV-Vis absorption spectra of PMMA/R-BINOL thin films annealed at various temperatures (Fig. 2.4). A gradual decrease in BINOL absorption peak was observed beginning at 80 °C, with a significant reduction occurring beyond 140 °C. This suggests that BINOL may be removed from the film through either thermal decomposition or sublimation during annealing.

To differentiate between these two possibilities, we investigated the thermal stability of BINOL by conducting ^{1}H NMR measurements of S-BINOL powders annealed at various temperatures, using petri dishes as containers (Fig. 2.5-2.9). The NMR spectra showed no change in chemical shifts or integration ratios between the hydroxyl and aromatic proton signals across all temperature conditions (Table 2.2), indicating that the molecular structure of BINOL remained intact. These results confirm that BINOL does not undergo thermal decomposition under the annealing conditions used, and that the

observed decrease in optical signals is attributable to sublimation of the BINOL from the thin film.

During the annealing of S-BINOL powders, visible deposition of S-BINOL was observed on the inner surface of the petri dish lid at temperatures above 140 °C, indicating a phase transition consistent with sublimation. Notably, the ^{1}H NMR spectrum of the S-BINOL collected after annealing at 220 °C was identical to that of the pristine sample (Fig. 2.9, Table 2.2), confirming that the molecular structure remained unchanged during the thermal process. Based on these results, we conclude that the reduction in BINOL-related signals in the CD and UV-Vis absorption spectra of F8BT/BINOL thin films after annealing is primarily due to the sublimation of BINOL, rather than thermal decomposition.

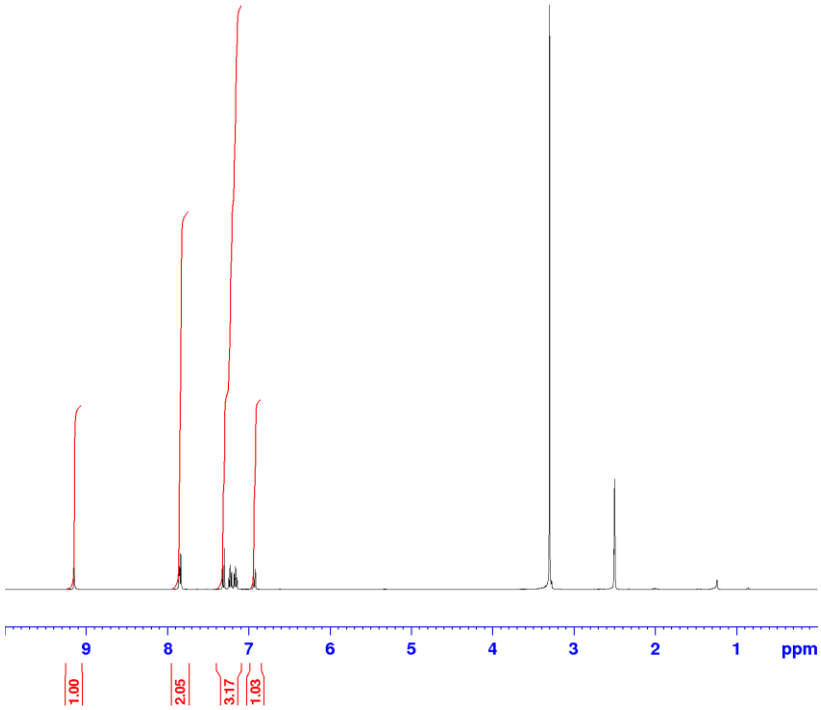

Fig. 2.5 The ^{1}H NMR (DMSO-d6, 22 °C) of S-BINOL.

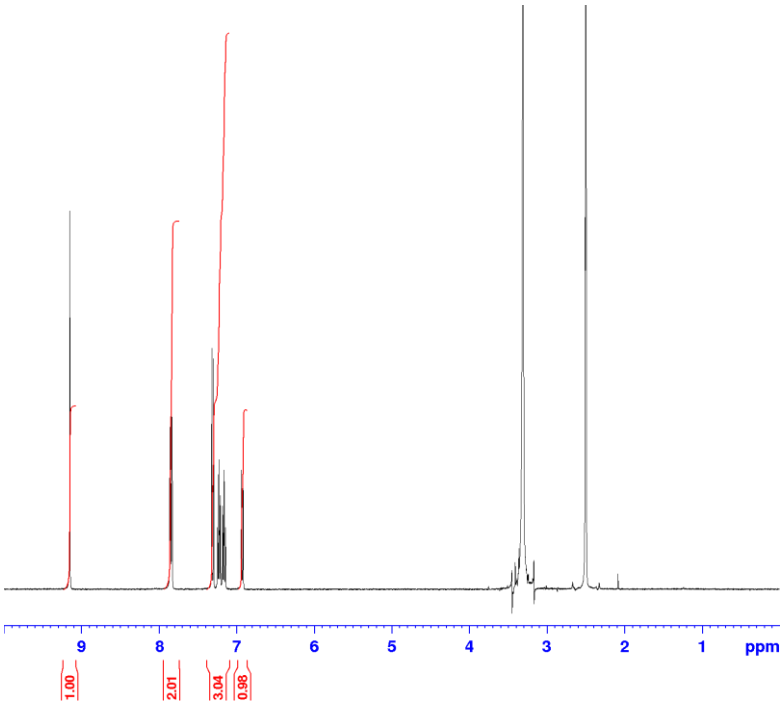

Fig.2.6 The ^{1}H NMR (DMSO-d6, 22 °C) of S-BINOL after annealing at 140 °C for 10 min.

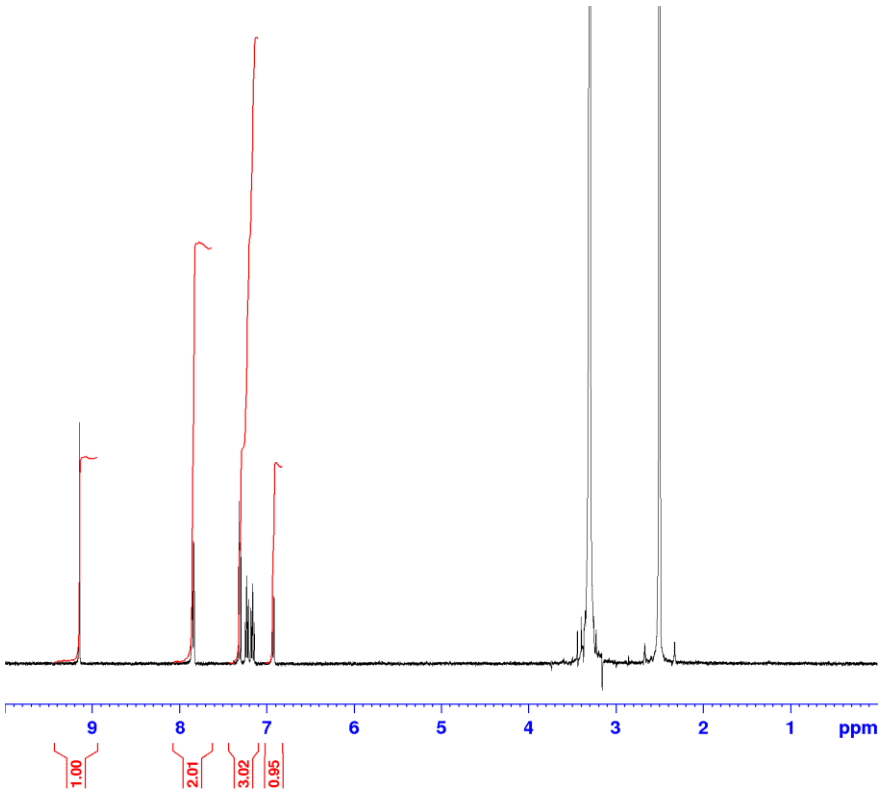

Fig. 2.7 The ^{1}H NMR (DMSO-d6, 22 ℃) of S-BINOL after annealing at 200 ℃ for 10 min.

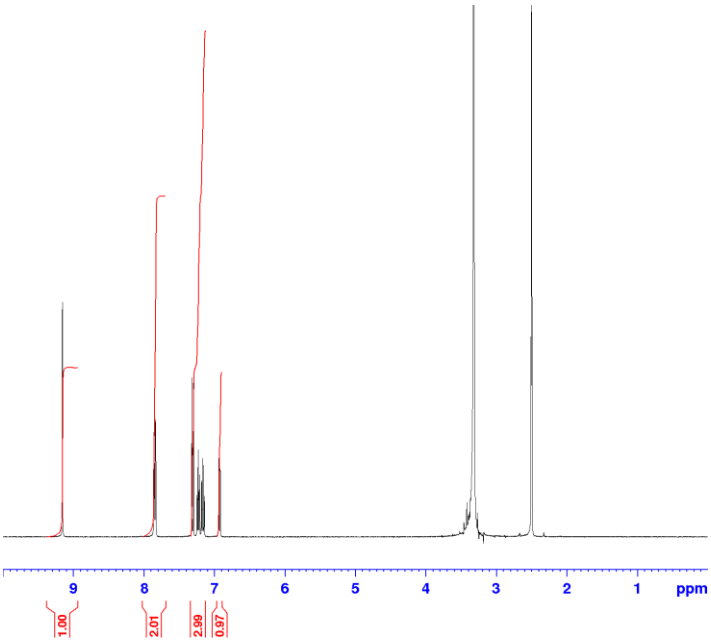

Fig. 2.8 The ^{1}H NMR (DMSO-d6, 22 ℃) of S-BINOL after annealing at 220 ℃ for 10 min.

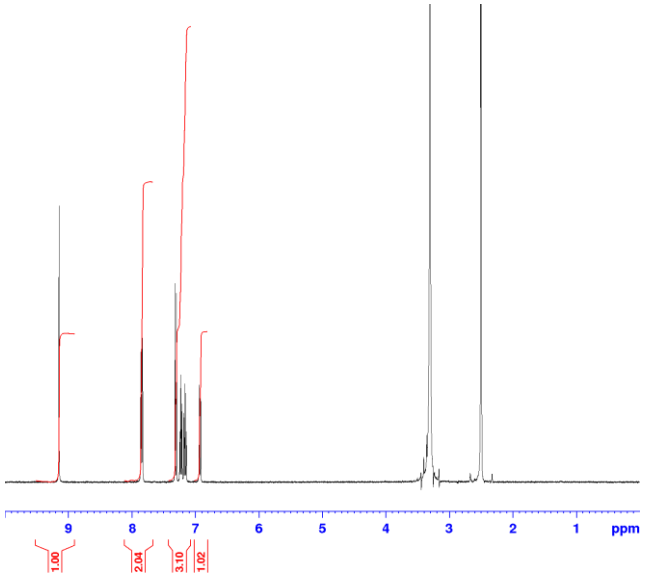

Fig. 2.9 The ^{1}H NMR (DMSO-d6, 22 °C) of S-BINOL S-BINOL that was recrystallized after sublimation after annealing at 220 ℃ for 10 min.

Table 2.2 The integration ratio of protons between the hydroxyl proton and aromatic protons of pure S-BINOL, after annealing at different temperatures and sublimated samples.

	Unannealed	140 ℃	200 ℃	220 ℃	220 ℃ (deposited)
Integration ratio	6.25	6.03	5.98	5.97	6.16

Fig. 2.10a and 2.10b present the CD and UV-Vis absorption spectra of F8BT/R-BINOL and F8BT/S-BINOL thin films annealed at various temperatures ranging from 100 °C to 220 °C. The CD signal corresponding to BINOL in films annealed at 100 °C (blue line) was reduced to less than half of that observed in the unannealed films (black line), and disappeared entirely upon annealing above 120 °C. This behavior corresponds well with the UV-Vis spectral changes observed in PMMA/R-BINOL films and is attributed to the sublimation of BINOL during thermal treatment. Meanwhile, a weak CD

signal corresponding to F8BT emerged at 475 nm after annealing at 100 °C and progressively intensified with increasing temperature up to 200 °C, indicating gradual induction of chirality in the F8BT matrix.

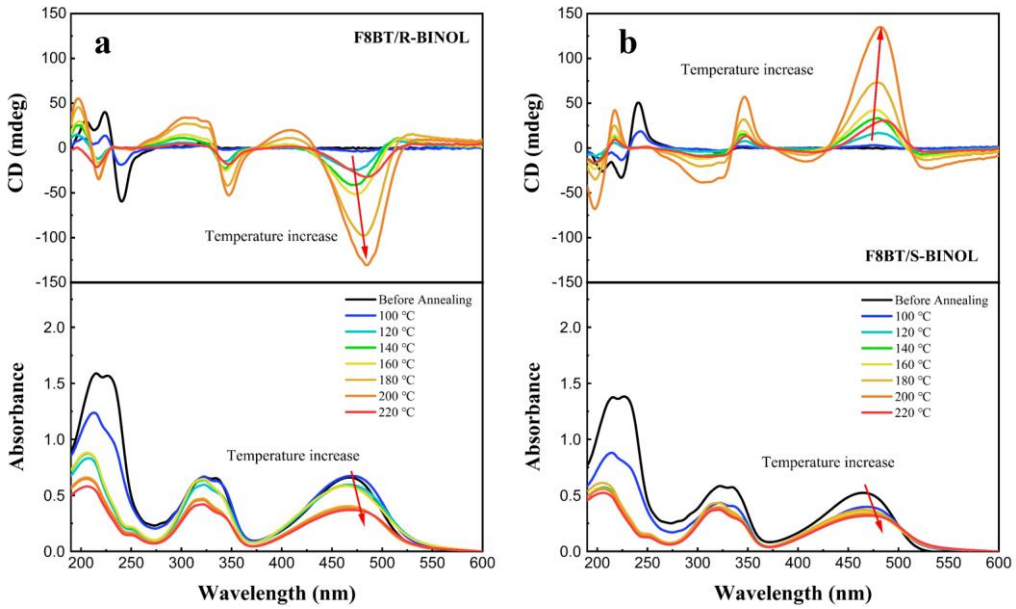

Fig. 2.10 CD spectra and UV-Vis absorption spectra of thin films of (a) F8BT/R-BINOL and (b) F8BT/S-BINOL before and after annealing at various temperatures for 10 minutes.

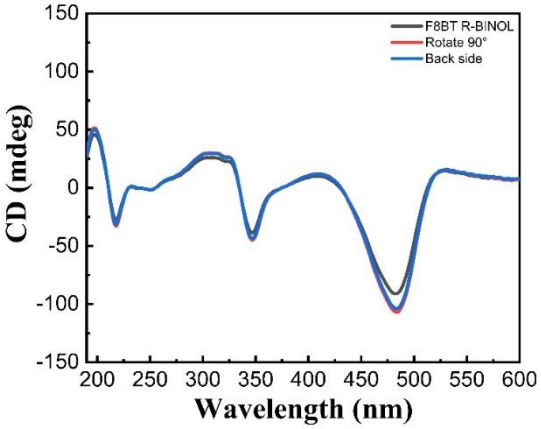

Fig. 2.11 CD spectra of the F8BT/R-BINOL thin film annealed at 200 °C for 10 minutes, measured under different orientations: with the film surface facing the detector ("F8BT/R-BINOL"), with the back side facing the detector ("Back side"), and after rotating the sample by 90° ("Rotate 90").

Figure 2.11 shows the CD spectra of the F8BT/R-BINOL thin film annealed at 200 °C for 10 minutes, measured with the film facing the detector ("F8BT/R-BINOL"), reversed ("Back side"), and rotated by 90° ("Rotate 90"). The negligible changes in CD signal across different orientations indicate minimal contributions from linear polarization (LP) and linear dichroism (LD) effects.[60] The CD spectra of F8BT/R-BINOL and F8BT/S-BINOL thin films at various annealing temperatures exhibited nearly perfect mirror-image symmetry, consistent with the Cotton effect and indicative of excellent experimental reproducibility.

The UV-Vis absorption and CD signals of F8BT exhibited a pronounced red shift and spectral broadening at around 490 nm after annealing, with the degree of red shift increasing at higher annealing temperatures. This absorption band corresponds to the HOMO–LUMO transition between the electron-donating fluorene (F8) unit and the electron-accepting benzothiadiazole (BT) unit in the donor–acceptor copolymer

backbone of F8BT, where the HOMO is primarily localized on the F8 moiety and the LUMO on the BT unit.[70,71] The red-shift observed in the absorption peak suggests an increase in the effective conjugation length along the main chain of F8BT, due to enhanced molecular ordering or planarization within the chiral F8BT polymer chains.

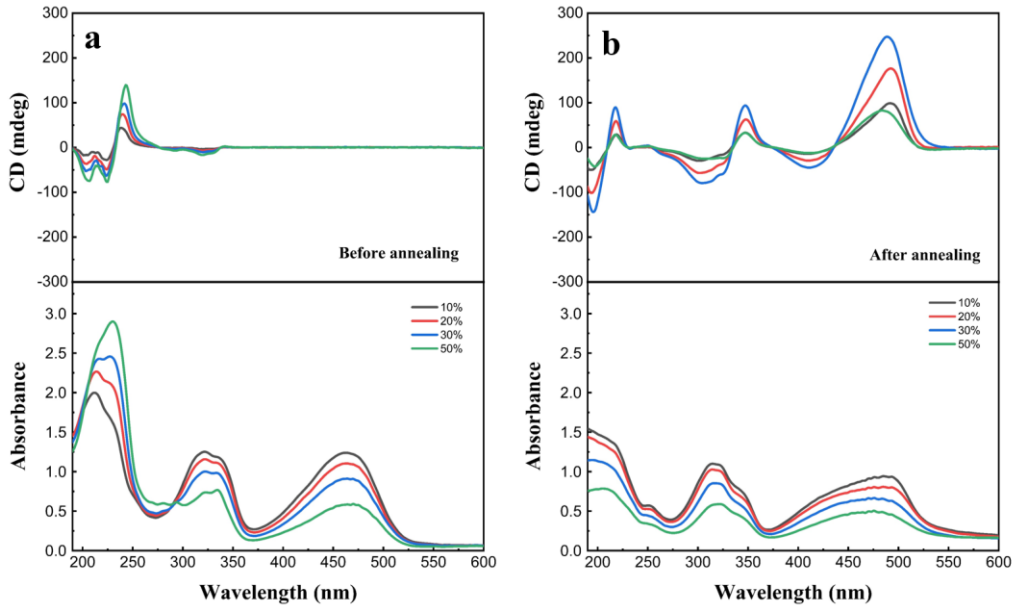

Fig. 2.12 CD and UV-Vis absorption spectra of F8BT/S-BINOL thin films with varying BINOL concentrations: (a) before annealing and (b) after annealing at 200 °C for 10 minutes.

The effect of BINOL concentration on the chiroptical properties of F8BT/BINOL composite films was systematically investigated by varying the BINOL content from 10

to 50 wt%. As illustrated in Fig. 2.12a, the CD spectra of the films before annealing exhibited no significant chiral features. However, upon annealing at 200 °C for 10 minutes (Fig. 2.12b), pronounced CD signals emerged, confirming the successful induction of chirality in the F8BT matrix. The corresponding dissymmetry factors (g_{CD}) are summarized in Table 2.3. Notably, the film containing 30 wt% BINOL exhibited the highest g_{CD} value of 0.012, indicating that this concentration is optimal for maximizing chiral induction under the given thermal treatment. This g_{CD} value is lower than that reported for F8BT induced by 1-aza[6]helicene,[57] but is comparable to those obtained using other binaphthyl derivative chiral inducers.[72–74] Additionally, both the UV-Vis absorption and CD peaks of F8BT exhibited a noticeable blue shift with increasing BINOL concentration, suggesting changes in the molecular environment and packing of the polymer chains.

Table 2.3 The g_{CD} values of F8BT/BINOL thin films with varying BINOL doping concentrations after annealing at 200 °C for 10 minutes.

Concentration of S-BINOL	10 wt%	20 wt%	30 wt%	50 wt%
g_{CD}	0.003	0.007	0.012	0.005

Due to the sublimation of BINOL during the annealing process, we decided to anneal the samples on the hot plate rather than oven to avoid the contamination. Another advantage of the hot stage is that the actual annealing temperature can be directly measured. To balance film preparation and asymmetric factors, we chose to dope 33 wt% BINOL in F8BT films in this work. Since the glass transition temperature (T_g) of F8BT characterized by differential scanning calorimetry (DSC) is 115 ℃ (Fig. 2.13), the best annealing temperatures were explored between 140 ℃ and 200 ℃. The strongest CD signal appeared after annealed at 180 ℃ for 10 min (Fig. 2.14a) with the maximum g_{abs} value of -5.3×10^{-2} for F8BT R-BINOL system and 6.1×10^{-2} for F8BT S-BINOL system at 495 nm (Fig. 2.14b). These results are slightly different with the samples annealed in the oven; the reason may be that the temperature set in the oven was different from the actual temperature.

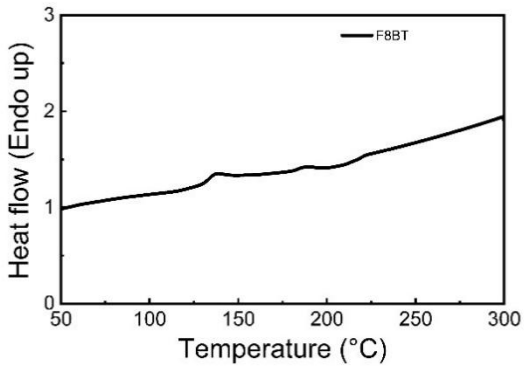

Fig. 2.13 Differential scanning calorimetry data for neat F8BT indicated the Tg at 115 ℃ and the melting point at 225 ℃.

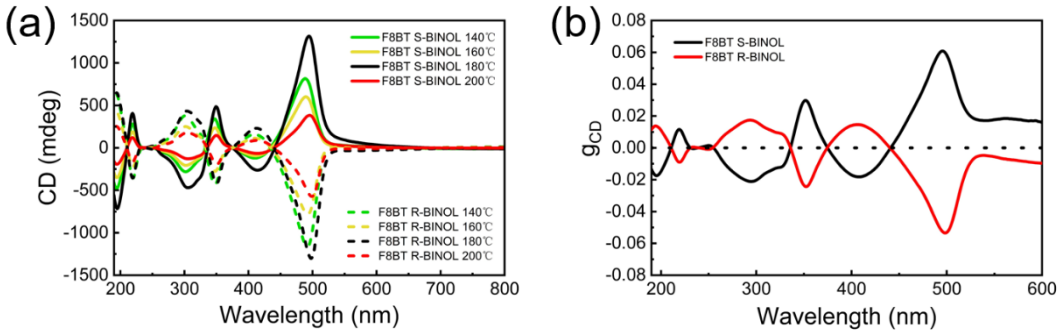

Fig. 2.14 (a) CD spectra of F8BT/R-BINOL and F8BT/S-BINOL thin films after annealing at different temperatures. (b) The g_{CD} of F8BT/R-BINOL and F8BT/S-BINOL thin films after annealing at 180 ℃.

2.3.2 CPL signal of F8BT induced by BINOL and increased PLQY

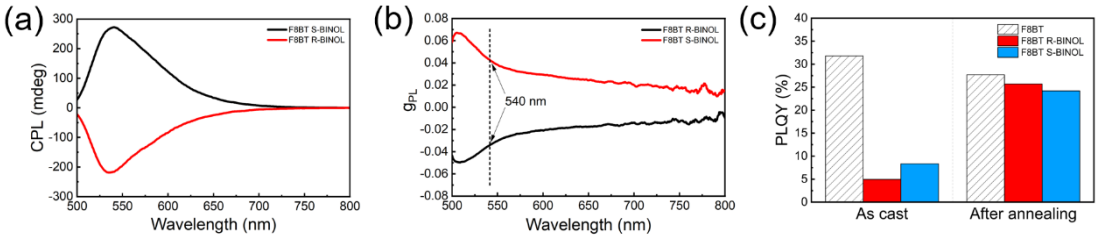

Fig. 2.15 CPL spectra (a) and corresponding g values (b) of F8BT/R-BINOL and F8BT/S-BINOL thin films after annealing. (c) PLQY of neat F8BT, F8BT/R-BINOL and F8BT/S-BINOL thin films before

and after annealing.

Table 2.4 PLQY of F8BT, F8BT/R-BINOL, and F8BT/S-BINOL thin films before and after annealing at 200 °C for 10 minutes.

PLQY	F8BT	F8BT/R-BINOL	F8BT/S-BINOL
Before annealing	31.8%	4.95%	8.35%
After annealing	27.7%	25.70%	24.20%

While CD reflects the chirality in the ground state, CPL provides information into the chiral nature of the excited state. The CPL spectra and corresponding g_{lum} of F8BT/BINOL system are shown in Fig. 2.15a and 2.15b. Both F8BT/R-BINOL and F8BT/S-BINOL thin films showed strong CPL signal, and the CPL signals between the enantiomers show almost perfect symmetry. The CPL peak position of F8BT/BINOL system located at 540 nm and matched well with the PL spectra. The maximum g_{PL} reached -5.0×10^{-2} for F8BT/R-BINOL system and 6.7×10^{-2} for F8BT/S-BINOL. The g_{PL} at the strongest CPL wavelength 540 nm are -3.5×10^{-2} and 4.3×10^{-2}, respectively.

An application of F8BT/BINOL films is applied as the emitting layer in CP-OLEDs

to achieve CPEL. One of the most important parameters for CP-OLEDs is EQE, which is directly proportional to the PLQY of the emitting layer. PLQY of thin films of F8BT, F8BT/R-BINOL, and F8BT/S-BINOL before and after annealing are summarized in Table 2.4. Prior to annealing, the F8BT/BINOL composite films exhibited significantly lower PLQY compared to the pristine F8BT films. However, after annealing, the PLQY of the composite films recovered to levels comparable with those of the pure F8BT films. This recovery in PLQY appears to correlate with the disappearance of BINOL-related absorption signals after thermal treatment, suggesting that the removal of BINOL via sublimation may mitigate non-radiative pathways introduced by its presence. According to our previous research,[69] BINOL mixed in F8BT films sublimated during the annealing process. The NMR spectra of F8BT/BINOL before and after annealing (Fig. 2.16) proved the complete removal of BINOL during annealing process and remained neat F8BT films. In other words, after the chiral induction during the annealing process, we achieved CPL emission from the neat F8BT films. Besides, the PLQY of F8BT/BINOL films was fully recovered to the same level as that of neat F8BT films after annealing (27.7%, 25.7% and 24.2% for neat F8BT, F8BT/R-BINOL and F8BT/S-BINOL, respectively). Theoretically, CP-OLEDs utilizing F8BT/BINOL as the emitting layer have the potential to achieve an EQE comparable to that of neat F8BT OLEDs. Removal of chiral inducers by sublimation

is not due to any unique property of BINOL but rather to its low molecular weight, and similar phenomena were also reported previously with other chiral inducers.[75,76] Currently, achieving both high luminescence efficiency and a high asymmetry factor still remains challenging.[77] The removal of small-molecule chiral inducers from chiral induction systems via high-temperature sublimation could represent as a general strategy. This approach enables the achievement of high asymmetry factors while eliminating the adverse effects of chiral inducers on luminescence efficiency, thereby chasing the upper limit of the EQE of neat emitting materials.

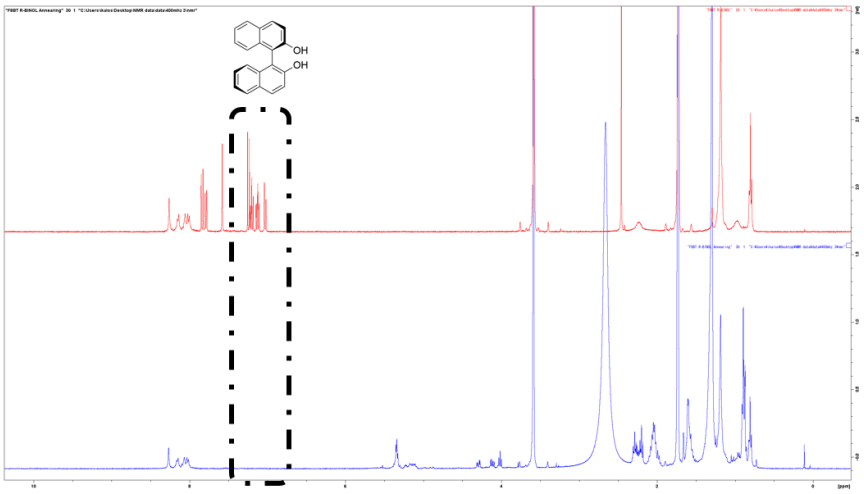

Fig. 2.16 NMR spectra of F8BT/R-BINOL before and after annealing. BINOL's signal completely disappeared after annealing indicated complete removal of BINOL by sublimation.

2.3.3 Mechanism of chiral induction and morphology research

Based on the CD and CPL results of the F8BT/BINOL system, the temperature dependence of the CD intensity of F8BT can be rationalized by a two-step chiral induction process occurring at different thermal conditions. The initial induction stage, taking place below 120 °C, is likely driven by π–π interactions between the axially chiral BINOL molecules and the achiral F8BT chains.[11,59,78] The second stage of chiral induction in achiral F8BT is proposed to occur above 120 °C, mediated by the already chiralized F8BT matrix. For instance, the theoretically predicted glass transition temperature (T_g) of F8BT is approximately 103 °C, while the experimentally determined T_g is around 112 °C.[79] Above T_g, the polymer chains of F8BT gain increased mobility and conformational flexibility. As discussed in Fig. 2.2, BINOL likely remains within the F8BT matrix at temperatures below 120 °C, allowing sufficient interaction with the polymer chains. These interactions may influence the torsional angles between the F8 and BT units, thereby enhancing chiral organization within the polymer backbone during subsequent annealing.[80] Although BINOL may be removed from the F8BT thin films at temperatures above 120 °C, the induced chirality within the F8BT chains could serve as a secondary chiral source, further propagating chiral organization among the remaining achiral F8BT

segments. As the annealing temperature increases, the enhanced chain mobility of F8BT facilitates the formation of more ordered chiral domains, potentially leading to supramolecular self-assembly. Considering the melting point of BINOL is around 205-210 °C, rapid sublimation is likely to occur at 220 °C. Under such high-temperature conditions, the residence time of BINOL within the film may become too short to effectively induce further chiral structuring in F8BT, resulting in a sudden decline in the observed CD intensity. In other words, an optimal balance between the initial chiral induction by BINOL and the secondary amplification by chiralized F8BT chains appears to be achieved at annealing temperatures of approximately 200 °C (oven) and 180 °C (hot plate).

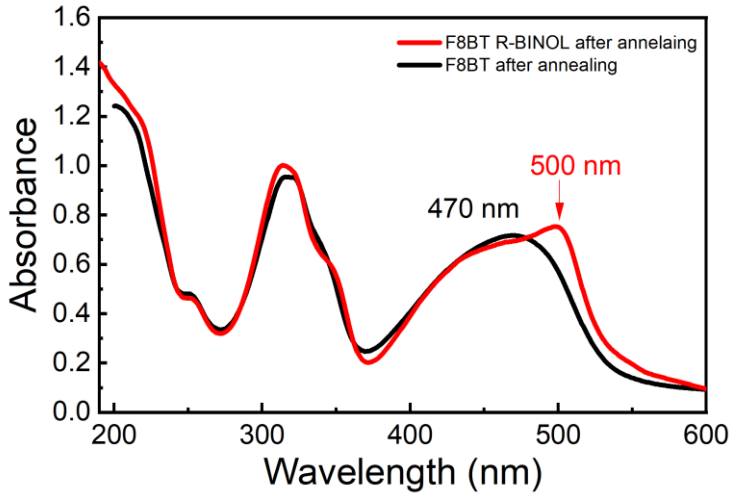

Fig. 2.17 UV-Vis absorption spectra of F8BT/R-BINOL and neat F8BT films after annealing.

Compare the absorption spectra of neat F8BT film and F8BT/R-BINOL film after annealing at 180 ℃, F8BT/BINOL system showed a clear red shift from 470 nm to 500 nm (Fig. 2.17). Since F8BT is a donor-acceptor copolymer, where the HOMO is located on the F8 unit and the LUMO is localized on the accepting BT unit, the absorption peak at 470 nm attributed to the HOMO-LUMO transition between the F8 and BT units.[81,82] The clear red shift indicated the longer π conjugation length of F8BT backbone induced by BINOL. Chiral inducers have the ability to change the twisting angle between F8 and BT units as reported before.[58,63]

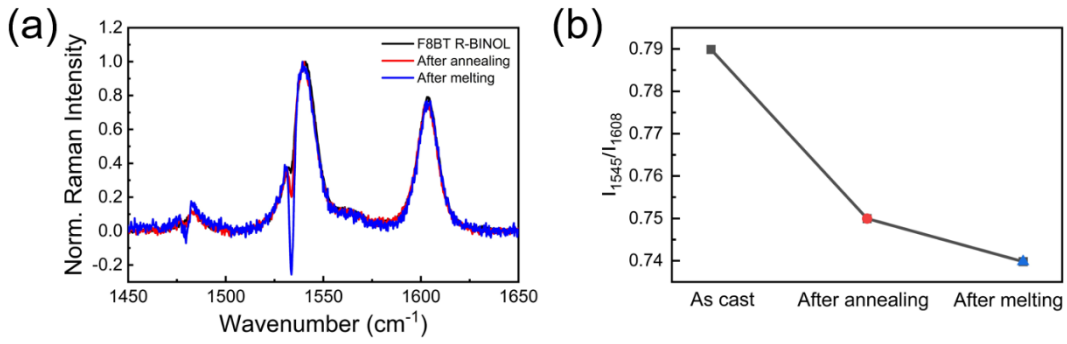

Fig. 2.18 (a) Normalized Raman spectra of F8BT/R-BINOL thin films as cast, after annealing and after melting. (b) Raman intensity ratios of I_{1545}/I_{1608}, indicates that F8BT/R-BINOL showed smaller dihedral angle after annealing and maintained it after melting.

The Raman peaks located at 1545 cm^{-1} and 1608 cm^{-1} are attributed to the characteristic backbone ring stretching vibrations of the BT and F8 units, respectively.[81,83] The twisting angle between F8 and BT units can be characterized by the relative intensity of these two peaks (I_{1608}/I_{1545}), and I_{1608}/I_{1545} decreases as the mainchain of F8BT becomes more planar (and vice versa). The small changes of I_{1608}/I_{1545} before and after annealing indicated that BINOL only slightly changed the dihedral angle of F8BT (Fig. 2.18). Compared with the as cast samples, I_{1608}/I_{1545} of annealed samples slightly decreased from 0.79 to 0.75, which indicated the smaller dihedral angle between F8 and BT units. This resulted in a more planar structure leading to longer π conjugations, this consists of the red-shift observed in UV-Vis spectra. The red-shifted peaks and the split CD spectra are typical features of exciton coupling and J-aggregates formed in F8BT induced by BINOL.[84,85] The planer structure of F8BT induced by BINOL enhanced the intermolecular exciton coupling between adjacent polymer chains,[86,87] thereby leaded to the strong chiroptical signals.

Fig. 2.19 POM of F8BT/BINOL as cast, after annealing and after melting.

Morphology research clearly revealed the chiral aggregates of F8BT induced by BINOL. Polarized optical microscope (POM) photos of F8BT/R-BINOL film showed birefringence after annealing compared with the total dark field of as cast film (Fig. 2.19), demonstrated the oriented structure of F8BT formed after chiral induction.

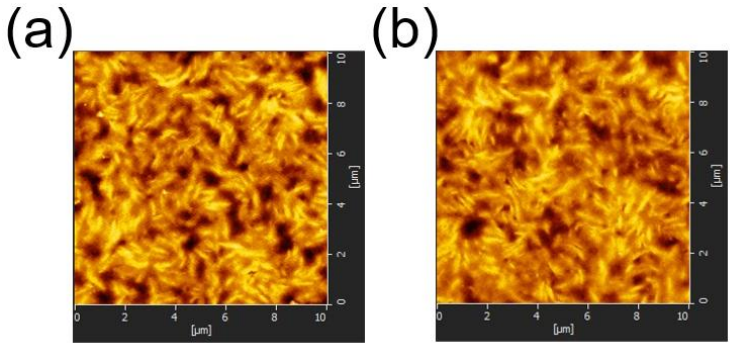

Fig. 2.20 AFM topography of F8BT/R-BINOL (a) and F8BT/S-BINOL (b) thin films after annealing.

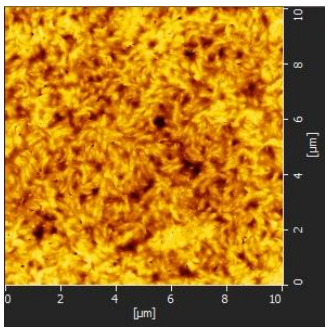

Fig. 2.21 AFM topography of neat F8BT films after annealing.

AFM topography figures of annealed F8BT/BINOL films clearly indicated the twisted cluster-like aggregate structures (Fig. 2.20a and 2.20b). The aggregates in F8BT/R-BINOL and F8BT/S-BINOL films exhibited clockwise and counterclockwise helical arrangements, respectively, indicating that the chiral inducers successfully induced the formation of chiral aggregates in F8BT. Even if neat F8BT showed similar aggregates after annealing (Fig.2.21), but the chiral symmetry cannot be broken without chiral inducer and there is no chiroptical signal. Due to the sergeants and soldiers effect, even a small amount of chiral inducers (BINOL) can sufficiently break the chiral symmetry of the polymer hosts (F8BT) and reveal the single-handed chiral structure.[88,89] Furthermore, the presence of aggregates amplified the size of the chiral structures in F8BT to match better with the wavelength of visible light, enhancing its interaction with circularly polarized light and thereby increasing the intensity of chiroptical spectra, such as CD and CPL.[90]

2.3.4 Chiral robustness of F8BT/BINOL system

The mechanism of chiral induction in polyfluorene derivatives with chiral small molecules is still unclear. Wade et al. proposed that the chiroptical signals arise from the natural optical activity caused by interchain twisting and the formation of blue phase

liquid crystals.[91] In contrast, Lee et al. attributed the chiral induction to cholesteric liquid crystal-like layered helical arrangements.[59,92] To further investigate the mechanism of chiral induction in this system, we attempted to disrupt the aggregates of F8BT induced by BINOL through melting and quenching. Based on DSC results, the melting point of F8BT is characterized as 225°C (Fig. S2). Accordingly, the films were melted and quenched twice at 240°C and 260°C, respectively. The specific experimental process is shown in Fig. 2.22.

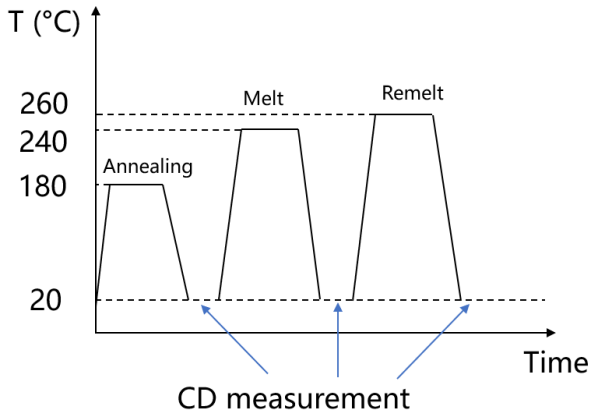

Fig. 2.22 Schematic diagram of the annealing and twice melting processes of F8BT/ BINOL films.

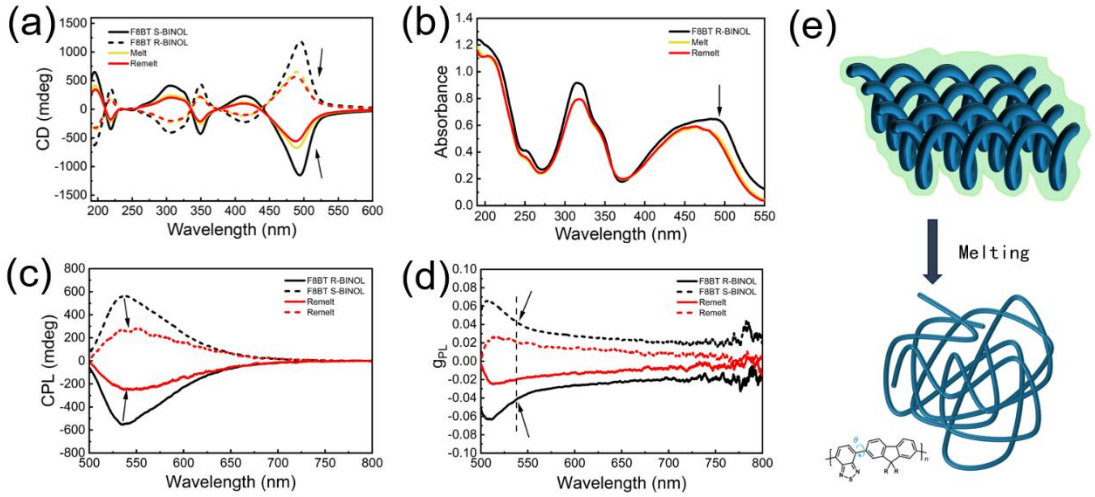

Fig. 2.23 CD spectra (a), UV-Vis absorption spectra (b), CPL spectra (c) and corresponding g values (d) of F8BT/R-BINOL and F8BT/S-BINOL thin films after annealing and after melting twice. (e) Schematic diagram of the aggregate structure of the F8BT/BINOL system was broken after melting, but the intramolecular torsion was retained.

Remarkably, neither the first nor the second melting completely eliminated the CD and CPL signals of F8BT samples. Even after the second complete melting, F8BT retained approximately 50% of g_{lum} than the maximum value (Fig. 2.23a, 2.23c and 2.23d). Following melting and quenching, the birefringence of the films disappeared completely (Fig. 2.24), and the aggregation structures were destroyed confirmed by AFM. UV-vis absorption spectra also supported these phenomena, the red-shift at 500 nm after

annealing vanished after melting and the absorption peak returned to 470 nm. It indicated that the J-aggregates and interchain exciton coupling were destroyed after melting.

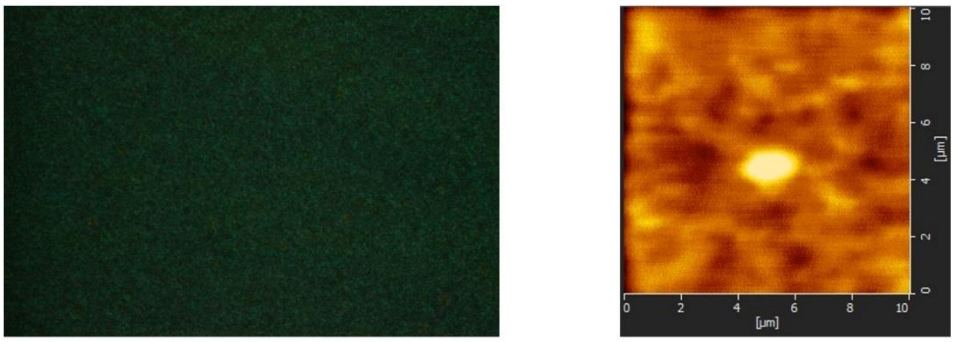

Fig. 2.24 POM and AFM topography of F8BT/R-BINOL films after melting twice.

Based on these results, we suppose that the chiral induction of F8BT/BINOL system includes a two-step mechanism. The chiroptical signals originated from the twisting between F8 and BT units induced by BINOL, which was subsequently amplified by aggregation and interchain exciton coupling. The melting process disrupted the aggregation structures but didn't break the intrachain twisting of F8BT. The Raman spectroscopy results also confirmed this speculation, I_{1608}/I_{1545} remained a relatively low value (0.74) after melting compared with the as cast film (0.79), indicating that the twisting between F8 and BT units induced by BINOL remained after melting.

Consequently, the chiroptical signals of F8BT were weakened due to the loss of amplification but did not vanish entirely after melting. Combined with previous experimental results, we not only achieved CPL of neat achiral polymers, but also achieved partial chiral memory without any crosslinking. We call it the high-temperature chiral robustness of the F8BT/BINOL system.

2.4 Conclusions

In this chapter, we demonstrated that BINOL effectively induces chirality in F8BT within thin films. Prior to annealing, the F8BT/BINOL films exhibited CD signals corresponding only to BINOL. However, upon annealing at 180 °C, the CD signals associated with BINOL disappeared, while a pronounced CD signal from F8BT emerged, accompanied by a notable increase in PLQY. These observations suggest a two-step chiral induction process: initially, BINOL interacts with F8BT polymer chains, inducing a twist via π-π interactions; subsequently, at elevated temperatures, the twisted F8BT chains undergo supramolecular self-assembly into chiral nanofiber bundles. The strong CD and CPL signal was achieved after annealing reached the maximum g_{lum} of 4.3×10^{-2}at 540 nm. The complete sublimation of BINOL during annealing resulted in the CPL from neat

achiral polymer with improved PLQY. By researching the high-temperature chiral robustness, we found that the chiroptical signals of F8BT originate from the twisting between F8 and BT units then enlarged by intermolecular exciton coupling and aggregates. This research provides a general strategy for removing chiral inducers to achieve neat emitting layers, offers a potential approach for achieving both high asymmetric factors and high EQE in future CP-OLEDs.

Chapter 3
CP-OLEDs made of F8BT/BINOL system as the emitting layer

3.1 Introduction

CPEL has garnered significant interest due to its promising applications in areas such as 3D displays and optical information storage. One of the effective strategies to realize CP-OLEDs is the construction of chiral light-emitting layers by chiral induction, where chiral small molecules are doped as chiral inducers into achiral luminescent polymers. Due to the chiral transfer, strong circularly polarized luminescence of the polymer can be achieved. While this method can yield high asymmetry factor g, the presence of chiral inducers within the film can decrease the device performance of the CP-OLEDs. To address this issue, it may be important to remove the chiral inducers from the emitting polymer after chiral induction is complete.

One of the most important parameters for CP-OLEDs is EQE. In the previous chapter, we have introduced the chiroptical signals of F8BT induced by BINOL. The high-PLQY films with strong CPL signals prepared in Chapter 2 are promising candidates for the emitting layer of CP-OLEDs with high EQE. In this chapter, we applied the

F8BT/BINOL films as the emitting layer of CP-OLEDs and F8-TFB was applied as the electron blocking layer, which was utilized to adjust the exciton recombination zone to achieve higher EQE. A summary of the specific performance of the CP-OLEDs is provided below.

The device after removing the chiral inducer achieved a maximum current efficiency (CE_{max}) of 1.46 cd/A and 1.45 cd/A for R-BINOL and S-BINOL samples. The g_{EL} of -5×10^{-3} and 7×10^{-3} for R-BINOL and S-BINOL samples were achieved without any optimization of the device structures yet. The CP-OLEDs using neat F8BT, F8BT/R-BINOL, and F8BT/S-BINOL as the emissive layers achieved EQE_{max} of 1.09%, 1.20%, and 1.01%, respectively. This indicates that the chiral induction system can achieve similar EQE of the pure F8BT devices after the sublimation removal of the chiral inducer. Notably, the removal of BINOL via sublimation does not rely on the specific properties of BINOL but is applicable to a wide range of small-molecule chiral inducers. Therefore, this method holds the potential for universal applicability in enhancing the efficiency of CP-OLEDs.

3.2 Experimental section

3.2.1 Experimental materials and device structure

In addition to the materials described in Chapter 2, the following materials were employed in the preparation of thin films and fabrication of devices in this chapter.

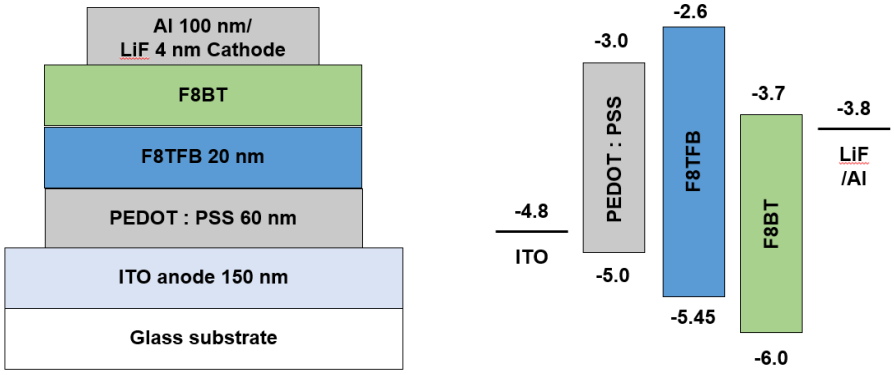

Fig. 3.1 The device structure and energy levels of CP-OLEDs.

CP-OLEDs were fabricated using a multilayer architecture, as illustrated in Fig. 3.1. Pre-patterned glass substrates coated with indium tin oxide (ITO) are widely employed as the anode in OLED devices due to their high optical transparency in the visible spectrum and relatively deep work function (~ -4.8 eV).[93] These properties enable efficient hole injection from ITO into the adjacent organic layers, while maintaining minimal optical loss from the substrate.

Poly(3,4-ethylenedioxythiophene):polystyrene sulfonate (PEDOT:PSS) is a conductive polymer mixture commonly used either as a hole transport layer (HTL) or a complementary anode interlayer in OLEDs. Its high conductivity, up to 10^3 S/cm following secondary doping or solvent treatments that reduce insulating PSS content[94,95]—and deep work function (~ –5.2 eV)[96,97] make it ideal for promoting efficient hole injection. In this study, PEDOT:PSS was also used to simulate OLED configurations with reduced intrinsic transmittance.

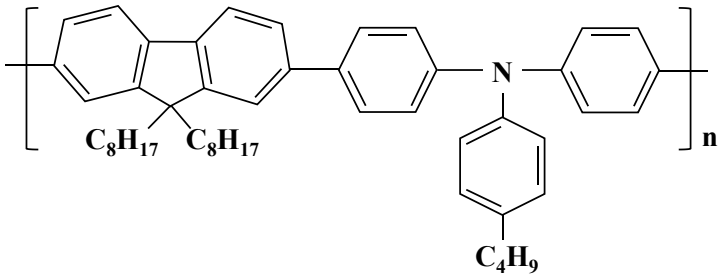

Fig. 3.2 Chemical structure of F8-TFB.

Poly(9,9-dioctylfluorene-co-N-(4-butylphenyl)-diphenylamine) (F8-TFB), the molecular structure is shown in Fig. 3.2, is commonly employed as a hole transport and electron blocking layer in solution-processed OLEDs. Its HOMO and LUMO energy levels are approximately –5.3 eV and –2.3 eV, respectively[98], making it suitable for hole conduction while effectively blocking electron transport from the emissive layer to the

anode.

F8BT is a solution-processable conjugated polymer frequently used as a fluorescent emissive material in OLEDs. It exhibits good solubility in a wide range of organic solvents with both low and high boiling points.[99] Its HOMO and LUMO energy levels lie at approximately –5.9 eV and –3.5 eV, respectively,[100] which are favorable for electron injection and hole confinement, thus facilitating efficient exciton formation.

Lithium Fluoride (LiF) is an insulating material typically used as an interfacial electron injection layer between the emissive layer (EML) and the metallic cathode. Upon deposition of aluminum over the LiF layer, interfacial reactions yield Li atoms and AlF_3 species. The dissociation of Li atoms facilitates n-type doping by donating electrons to Alq_3, forming Alq_3^- anions. This process significantly reduces the electron injection barrier and promotes effective contact with the cathode.[101,102]

Aluminum (Al) serves as the cathode due to its high reflectivity (>90%) in the visible region and a moderate work function (~ –4.2 eV).[103] These characteristics make Al well-suited for both electron injection and light reflection, contributing to enhanced device efficiency in bottom-emitting OLED architectures.

3.2.2 Preparation process of CP-OLEDs

All devices were constructed on indium tin oxide (ITO)-coated glass substrates with an ITO thickness of 150 nm.

Glass substrates pre-coated with 150 nm of indium tin oxide (ITO) were sequentially ultrasonicated in acetone, semicoclean solution, deionized water, and isopropyl alcohol. All cleaning procedures were carried out in a cleanroom environment. To enhance the work function of ITO and remove residual organic contaminants, the substrates were treated with UV–ozone irradiation for 30 minutes in a sealed chamber.[104]

After cleaning, PEDOT:PSS was filtered by 0.45 μm PVDF filters and spin-coated onto the ITO surface at 1600 rpm for 90 seconds. The films were subsequently annealed at 200 °C for 10 minutes. The resulting PEDOT:PSS layer, with an approximate thickness of 20 nm, served as the hole injection layer.

All substrates were then transferred into a nitrogen-filled (N_2) glovebox for the deposition of the emissive layers. Two polymer solutions were prepared in p-xylene: F8-TFB (10 mg/mL) and F8BT (20 mg/mL). Prior to deposition, both solutions were filtered through 0.2 μm PTFE filters to remove particulates.

F8-TFB was first deposited onto the PEDOT:PSS layer by spin-coating at 1600 rpm

for 90 seconds, followed by annealing at 180 °C for 15 minutes. Then toluene was spin-coated on samples to remove the extra F8-TFB. The resulting F8-TFB film, approximately 20 nm thick, functioned as the hole transport and electron-blocking layer. Subsequently, F8BT was spin-coated onto the F8-TFB layer at 2000 rpm for 30 seconds and annealed at 180 °C for 10 minutes, served as the emissive layer.

Following the solution-processing steps, the substrates were transferred to an ultra-high vacuum (UHV) thermal evaporation chamber with a base pressure of 1×10^{-8} Torr for cathode deposition. A 3 nm-thick LiF layer was deposited at a rate of 0.01 nm/s, followed by the deposition of a 100 nm-thick aluminum (Al) layer at 0.2 nm/s.

After cathode deposition, the devices were transferred via a vacuum-compatible shuttle to a nitrogen-filled glovebox, where they were encapsulated using glass covers, desiccant films, and UV-curable epoxy resin. This encapsulation step was essential to prevent degradation from ambient oxygen and moisture, thereby ensuring reliable device performance during subsequent measurements.[105]

3.2.3 Characterization methods of CP-OLEDs

The current density-voltage-luminance (J-V-L) characteristics of the OLED devices

were measured using a source meter (Keithley 2400) in conjunction with a luminance meter (Topcon BM-910D) equipped with an attachment lens (AL-8) and a solid measurement angle of 1°. Electroluminescence (EL) spectra were recorded using a spectrophotometer (PMA-11, Hamamatsu Photonics). The external quantum efficiency (η_{ext}) was determined using an integrating sphere system coupled with a calibrated silicon photodiode detector.

The outcoupling efficiency difference ($\Delta\eta_{out}$) was calculated based on η_{ext} measurements, following a procedure analogous to that described in Equation 3.8. Similarly, the luminance enhancement (ΔL) was computed by comparing the luminance values of the reference and patterned devices using the same equation.

The CPEL spectra was characterized by a customized CPL spectrometer (CPL-300, JASCO) in Nagoya University. The intensity of CPEL is quantified using a asymmetric factor, g_{EL}, defined as:

$$g_{EL} = \frac{I_L - I_R}{1/2(I_L + I_R)} = 2\frac{I_L - I_R}{(I_L + I_R)} \quad (3\text{-}1)$$

Here, I_L and I_R represent the emission intensities of LCP and RCP light, respectively. g_{EL} can be obtained directly through CPL-300.

3.3 Results and discussion

3.3.1 CPEL of CP-OLEDs with F8BT/BINOL system as the light-emitting layer

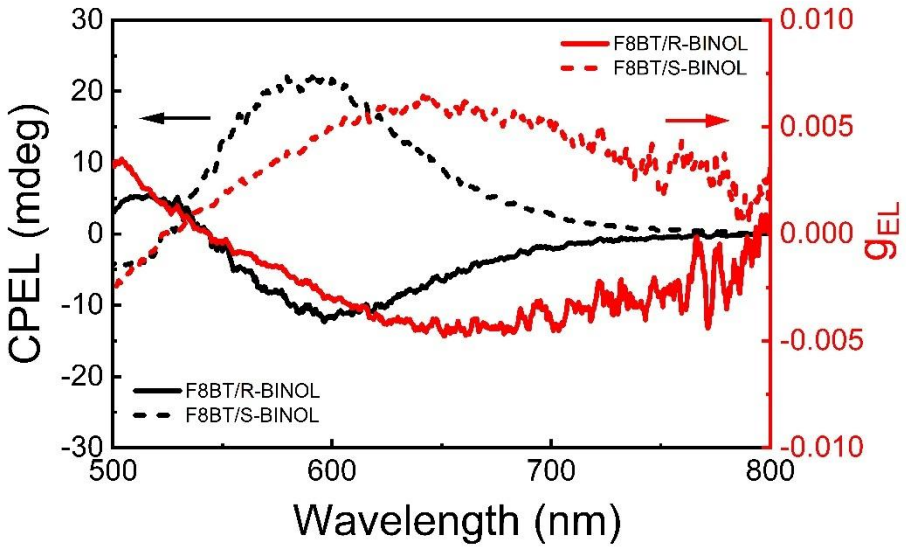

Fig. 3.3 CPEL spectra and corresponding g_{EL} of CP-OLEDs.

The device fabrication process was illustrated in Chapter 3.2. Following the traditional design, we applied F8BT/BINOL chiroptical system as the emitting layer of CP-OLEDs. We used F8BT/R-BINOL and F8BT/S-BINOL as the emitting layer, respectively. The CPEL spectra was measured with a CPL spectrometer (CPL-300, JASCO), which was customized to characterize CP-OLEDs. The CPEL spectra and

corresponding g_{EL} is shown in Fig. 3.3. g_{EL} can be obtained directly through CPL-300.

The CPEL spectra of CP-OLEDs performed very good symmetry between F8BT/R-BINOL and F8BT/S-BINOL as the emitting layer. The CPEL peak position of F8BT/BINOL system located at around 600 nm. The peak position was much red-shifted compared with the PL luminescence. The maximum g_{EL} reached -4.8×10^{-3} for F8BT/R-BINOL and 6.4×10^{-3} for F8BT/S-BINOL CP-OLEDs at around 650 nm. It showed further red-shifted compared with CPEL spectra. The g_{EL} at the strongest CPEL wavelength 600 nm reached -3×10^{-3} and 5.1×10^{-3}, respectively. CPEL results proved The results of CPEL spectra proved that CP-OLEDs constructed by F8BT/BINOL system can achieve circularly polarized electroluminescence successfully. However, the g_{EL} produced by both F8BT/R-BINOL and F8BT/S-BINOL CP-OLEDs are one order of magnitude less than the g_{lum} obtained from CPL spectra. This result was measured when we first prepared the device, and there is still room for improvement. In any case, this result proves the great potential of F8BT/BINOL system for application in the emitting layer of CP-OLEDs.

3.3.2 Device performance of CP-OLEDs with

F8BT/BINOL system as the light-emitting layer

Besides the CPEL-specific characteristics, the general electroluminescent device performance is also important. In addition to the above-mentioned CP-OLEDs with F8BT/R-BINOL and F8BT/S-BINOL as the emitting layer, we also prepared conventional OLEDs with neat F8BT as the emitting layer to compare the device performance. According to previous studies, BINOL completely sublimates and disappears after annealing, remained the neat F8BT. Therefore, CP-OLEDs should theoretically perform similar device performance with conventional OLEDs with neat F8BT as the emitting layer.

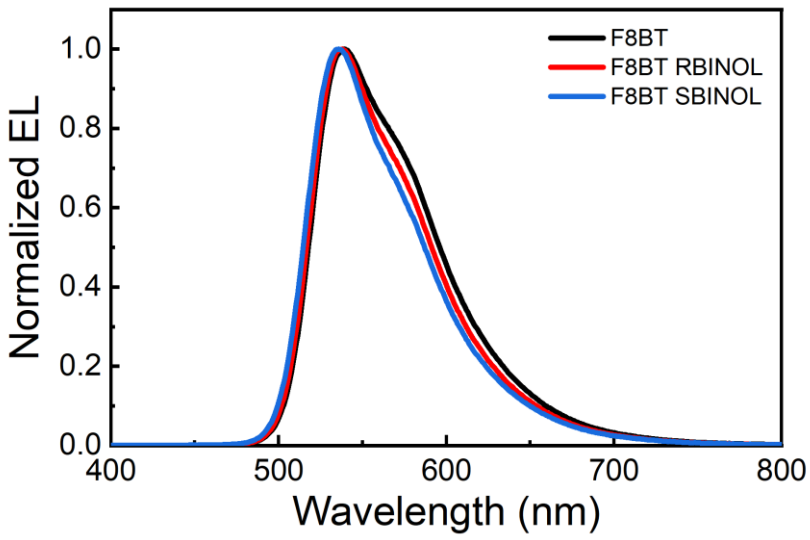

Fig. 3.4 EL spectra of F8BT/BINOL CP-OLEDs and F8BT OLEDs.

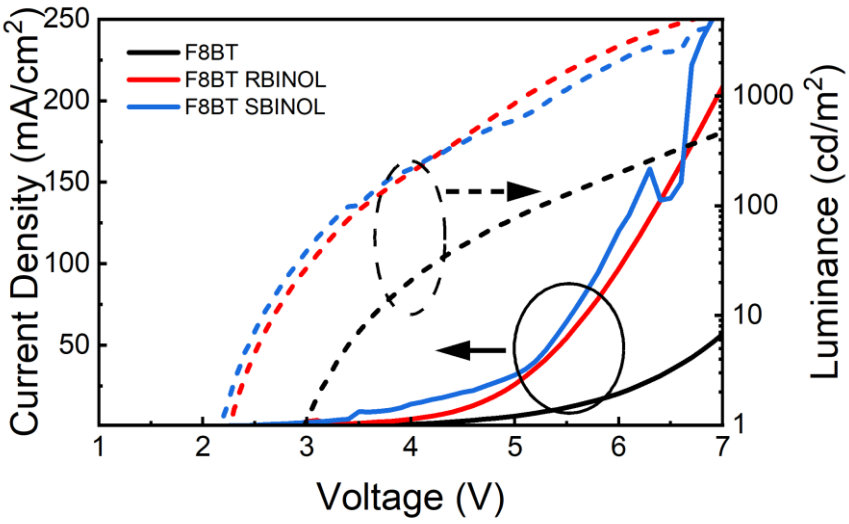

Fig. 3.5 J-V-L curves of F8BT/BINOL CP-OLEDs and F8BT OLEDs.

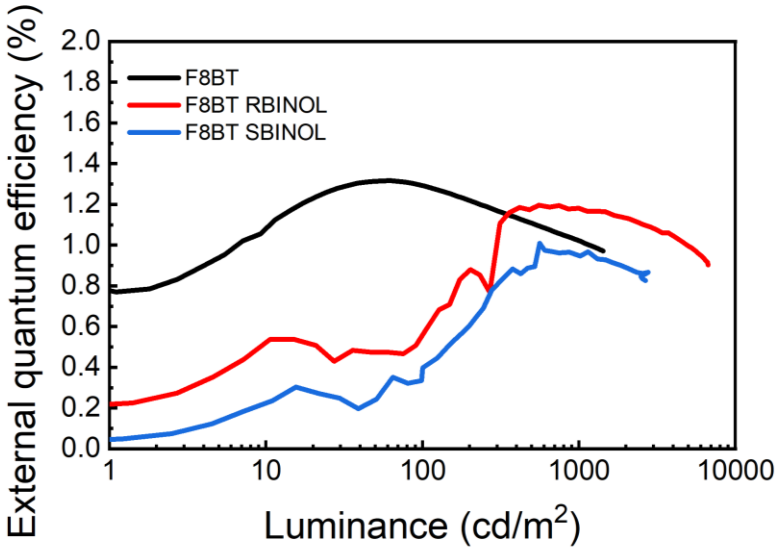

Fig. 3.6 EQE of F8BT/BINOL CP-OLEDs and F8BT OLEDs.

Table 3.1 Summary of device performance of F8BT/BINOL CP-OLEDs and F8BT OLEDs.

	λ_{EL} (nm)	V_{on} (V)	CE_{max} (cd/A)	EQE_{max} (%)
F8BT	540	2.6	1.36	1.09
F8BT/R-BINOL	536	2.2	3.15	1.20
F8BT/S-BINOL	538	2.1	1.81	1.01

The EL spectra of F8BT/BINOL CP-OLEDs and F8BT OLEDs are shown in Fig. 3.4. The J-V-L curve and EQE performance are shown in Fig. 3.5 and Fig. 3.6. All the device performance is summarized in Table 3.1. Compare with the neat F8BT OLED, F8BT/BINOL CP-OLEDs showed similar electroluminescence peak position. The 2 nm and 4 nm blue-shifted can be ignored. All OLEDs showed similar turn-on voltage around 2 V and F8BT/BINOL CP-OLEDs even showed smaller turn-on voltage than neat F8BT OLED. The highest current efficiency 3.15 cd/A was achieved by F8BT/R-BINOL CP-OLED. F8BT OLED and F8BT/S-BINOL CP-OLED showed similar current efficiency 1.36 cd/A and 1.81 cd/A, respectively. Finally, all the F8BT based OLEDs showed EQE higher than 1% and F8BT/BINOL CP-OLEDs showed comparable EQE than neat F8BT OLED. Even though there is still room for improvement of device fabrication, this is still

a relatively high luminous efficiency for polyfluorene based CP-OLEDs. Attribute to the sublimation of BINOL during annealing process, the actual light-emitting layer of F8BT/BINOL CP-OLEDs is pure F8BT, so it shows the same performance as neat F8BT OLED. High-temperature sublimation is not a unique property of BINOL, but a common property of small molecule chiral inducers, which is only related to the molecular weight. It is feasible to remove small molecule chiral inducers through high-temperature sublimation to achieve CPEL from neat achiral polymers. This design idea showed high potential for commercial CP-OLEDs.

3.4 Conclusions

This chapter demonstrates the first try to realize CP-OLEDs by sublimable chiral inducers to avoid the negative impact of chiral inducers on the device performance. The F8BT/BINOL films were selected as the emitting layer of CP-OLEDs. The CPEL signal was achieved successfully from the CP-OLEDs. The maximum g_{EL} reached -4.8×10^{-3} for F8BT/R-BINOL and 6.4×10^{-3} for F8BT/S-BINOL CP-OLEDs at around 650 nm. However, the g_{EL} produced by both F8BT/R-BINOL and F8BT/S-BINOL CP-OLEDs are one order of magnitude less than the g_{PL} obtained from CPL spectra. The general

electroluminescent device performance of CP-OLEDs has also been studied. The device after removing the chiral inducer achieved a CE_{max} of 1.46 cd/A and 1.45 cd/A for R-BINOL and S-BINOL samples. The g_{EL} of -5×10^{-3} and 7×10^{-3} for R-BINOL and S-BINOL samples were achieved without any optimization of the device structures yet. The CP-OLEDs using neat F8BT, F8BT/R-BINOL, and F8BT/S-BINOL as the emissive layers achieved EQE_{max} of 1.09%, 1.20%, and 1.01%, respectively. This indicates that the chiral induction system can achieve similar EQE of the pure F8BT devices after the sublimation removal of the chiral inducer. Notably, the removal of BINOL via sublimation does not rely on the specific properties of BINOL but is applicable to a wide range of small-molecule chiral inducers. Therefore, this method holds the potential for universal applicability in enhancing the efficiency of CP-OLEDs.

Chapter 4
Generalized chiral induction between polyfluorene derivatives and chiral inducer BINOL

4.1 Introduction

In previous chapters, we focused on the chiral induction effect of BINOL on F8BT. However, it remains unknown whether BINOL induces chirality in other polyfluorene derivatives. In this chapter, we investigate the chiral induction effect of BINOL on another polyfluorene derivative material PFO. Although the signal is weak, BINOL is still able to induce PFO to generate CD and CPL signals, with corresponding g values on the order of 10^{-3}. When PFO is treated with solvent vapor exposure (SVE) to produce the β-phase, the CD spectra shape changed, resulting in a shoulder peak.

Thermal annealing at 140 °C and the optimal BINOL concentration was identified as 22.8 wt%, yielding the highest CD signal. NMR analysis confirmed that BINOL sublimates completely above 180 °C. Film thickness also exhibited a strong impact on chiroptical properties. CD and CPL analysis revealed that films spin-coated at 500 rpm showed the strongest CD signals. These results demonstrate that precise control of

BINOL concentration, annealing parameters, and film thickness is critical for optimizing CPL performance in PFO/BINOL systems. Furthermore, β-phase formation via SVE serves as an effective post-treatment strategy to enhance CPL, particularly in thick films where thermal annealing alone is insufficient.

4.2 Experimental section

4.2.1 Experimental materials

In addition to the materials previously mentioned in Chapter 2, the following materials were used in the film preparation processes throughout this chapter. PFO (Mn < 25,000) was purchased from Sigma-Aldrich. All materials and reagents were used without further purification.

4.2.2 Sample preparation

PFO/BINOL blend solutions with a concentration of 20 mg/mL were prepared by doping BINOL into PFO at a weight ratio of 30 wt%. The solutions were stirred at 80 °C for 12 hours to ensure complete dissolution. Thin films were fabricated by spin-coating 100 μL of the solution onto quartz substrates at 1000 rpm for 90 seconds. The resulting

films were subsequently annealed on a hotplate at the designated temperature for 10 minutes in ambient air to promote molecular reorganization.

PFO is known to exhibit multiple crystalline phases, among which the β-phase offers superior chiroptical activity and device performance. To induce the α-to-β phase transition, SVE was applied following the setup illustrated in Fig. 4.1.[106]

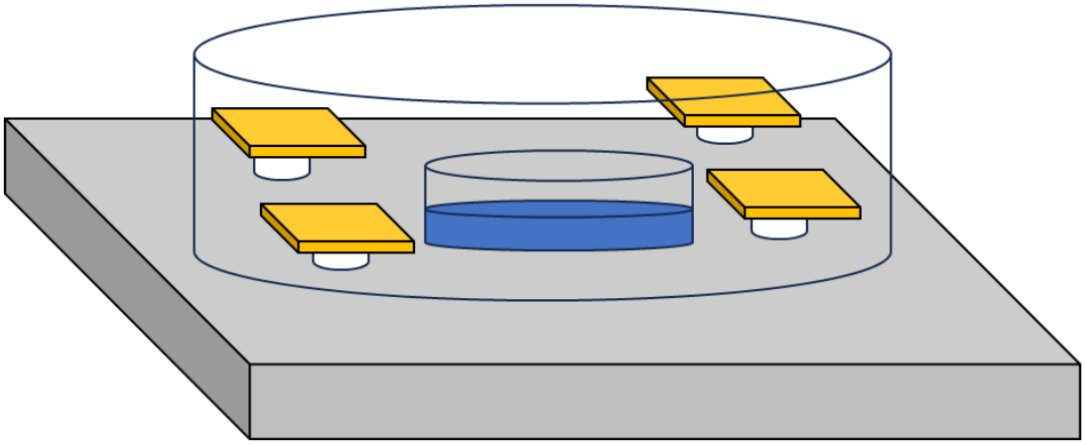

Fig. 4.1 The schematic diagram of SVE process.

In this procedure, a small Petri dish containing toluene was placed on a hotplate preheated to 50 °C. PFO-coated substrates were arranged around the dish using Teflon spacers to prevent direct heat transfer. The system was then sealed with a larger Petri dish and maintained at 50 °C for 1 hour, allowing toluene vapor to permeate and trigger phase

transition in the films.

4.2.3 Characterization methods

All characterization instruments and methods were the same as described in Chapter 2.

4.3 Results and discussion

4.3.1 Chiral induction of PFO by BINOL

Based on previous study, chiral inducer BINOL could induce the chiroptical properties of F8BT. However, it remains unknown whether BINOL induces chirality in other polyfluorene derivatives. To investigate the influence of BINOL as a chiral inducer on the PFO, a series of thin films were prepared with varying BINOL concentrations. Specifically, 20 mg of PFO was dissolved in toluene (1 mL) with the addition of 2-10 mg of S-BINOL, corresponding to BINOL weight fractions of 10%-50% relative to PFO. After preparation, the films were annealed at 160 °C for 10 minutes.

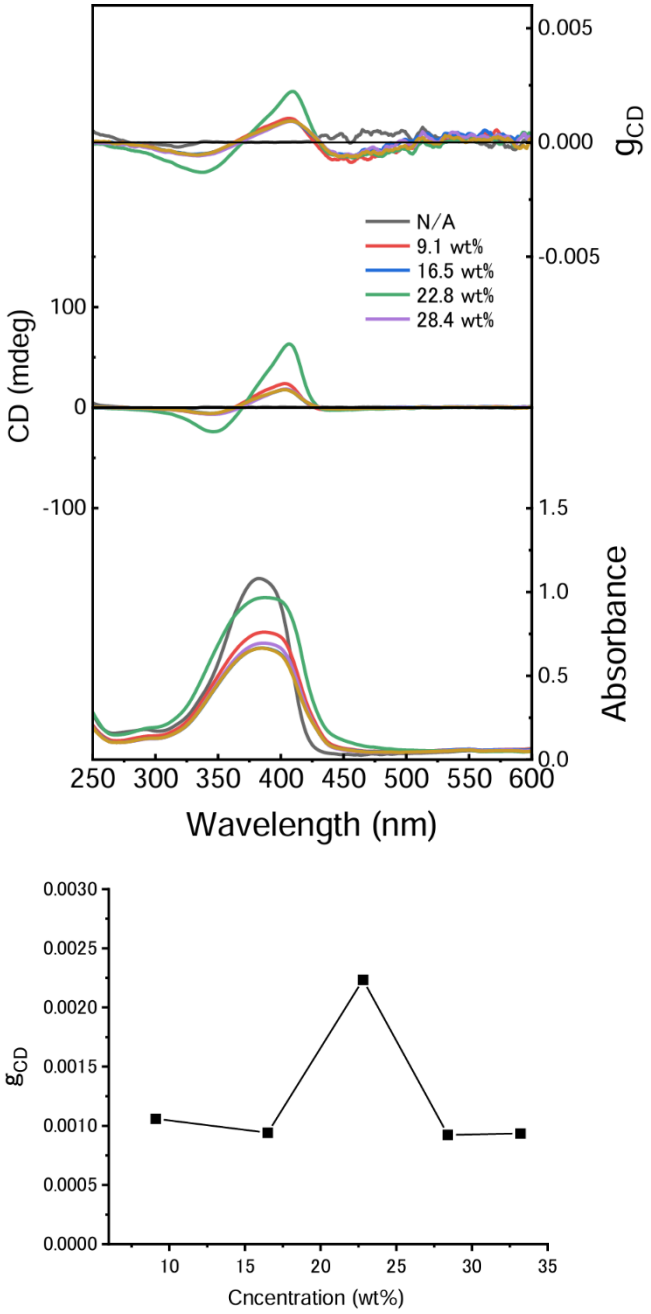

Fig. 4.2 The g_{CD} and CD spectra of PFO/BINOL thin films with different concentration of BINOL.

As shown in Fig. 4.2, the PFO/BINOL contained 22.8 wt% of BINOL exhibited the

strongest CD signal. This trend was consistent with previous results of F8BT-based systems. Therefore, 22.8 wt% BINOL was identified as the optimal concentration for inducing maximum CD in PFO/BINOL system.

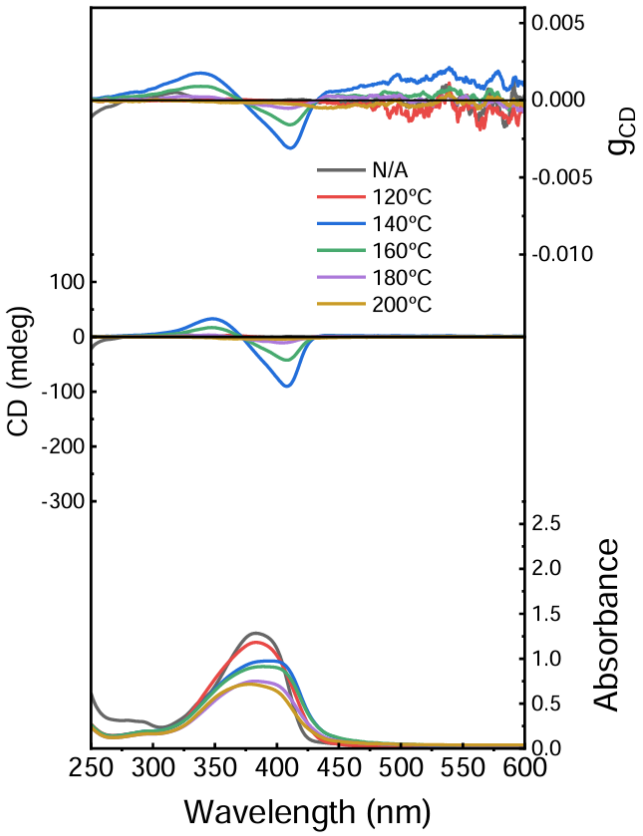

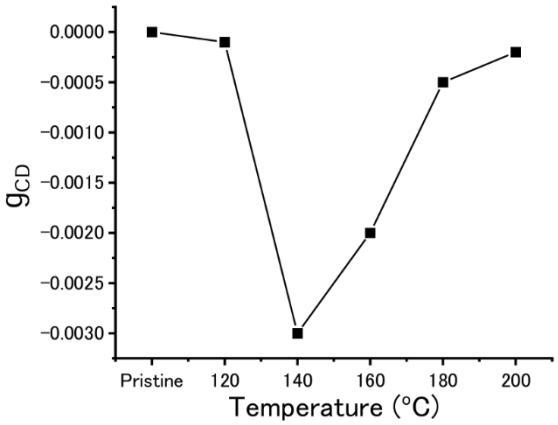

Fig. 4.3 The g_{CD} and CD spectra of PFO/BINOL thin films after different annealing temperatures.

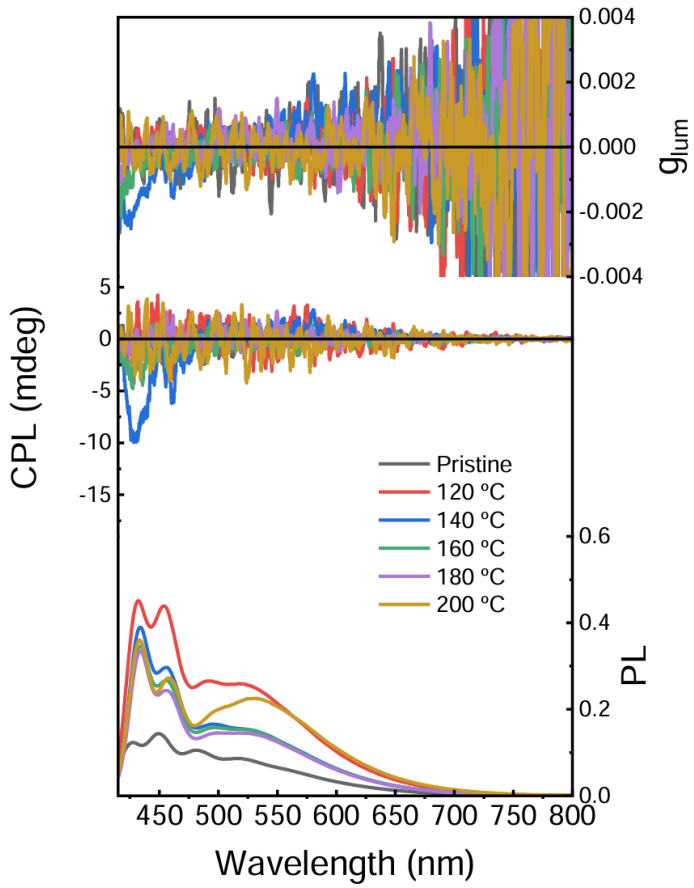

Fig. 4.4 The CPL spectra of PFO/BINOL thin films after different annealing temperatures.

As shown in Fig. 4.3, CD intensity exhibited a distinct annealing temperature dependence: it increased with temperature up to 140 °C, where it reached a maximum, and then declined at higher temperatures. The highest g_{CD} value was measured as -3.1 ×

10^{-3} at 413 nm, indicating optimal chiral ordering at this temperature. The CPL spectra are shown in Fig. 4.4, the maximum g_{lum} was observed as -2.4 × 10^{-3} at 426 nm.

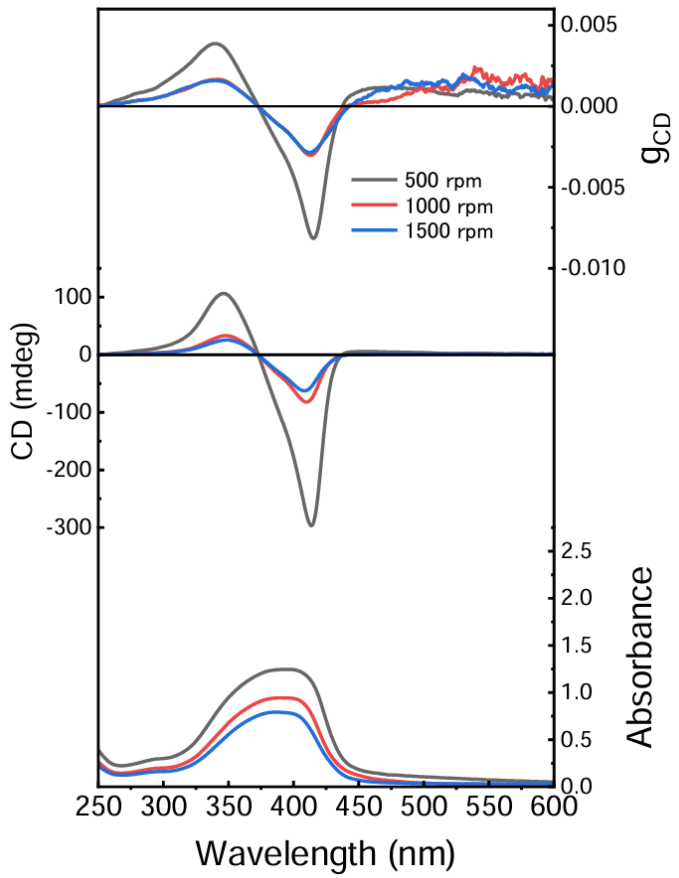

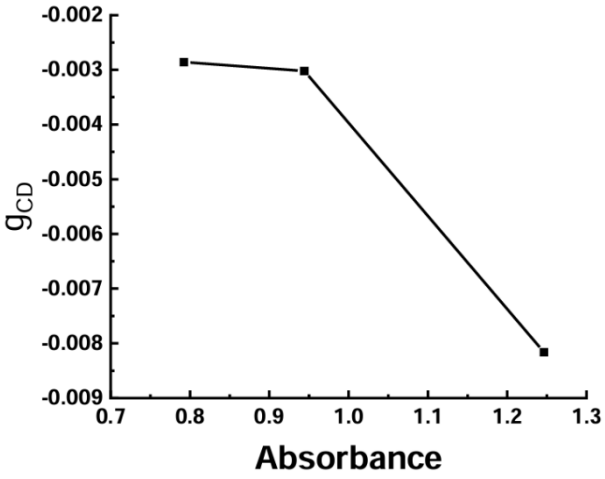

Fig. 4.5 The g_{CD} and CD spectra of PFO/BINOL thin films with different thickness.

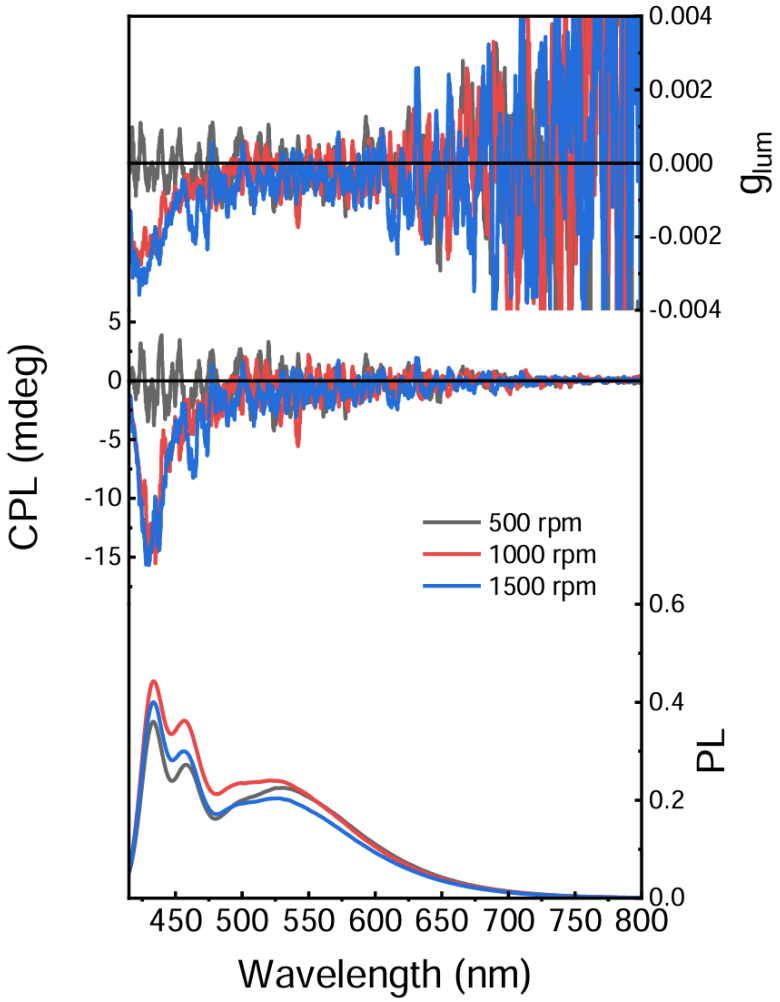

Fig. 4.6 CPL spectra of PFO/BINOL thin films with different thickness.

To evaluate the effect of film thickness on chiroptical properties, spin-coating speeds were varied at 500, 1000, and 1500 rpm for 90 seconds. CD and CPL spectra revealed

that the film fabricated at 500 rpm exhibited the highest chiroptical properties. In comparison, films prepared at 1000 and 1500 rpm showed reduced absorbance values of 0.94 and 0.79, respectively, corresponding to approximately 75% and 63% of the absorbance observed at 500 rpm. The maximum g_{CD} value was measured to be -8.0 × 10^{-3} at 415 nm. This suggests that film thickness has a greater impact on CD than annealing temperature alone.

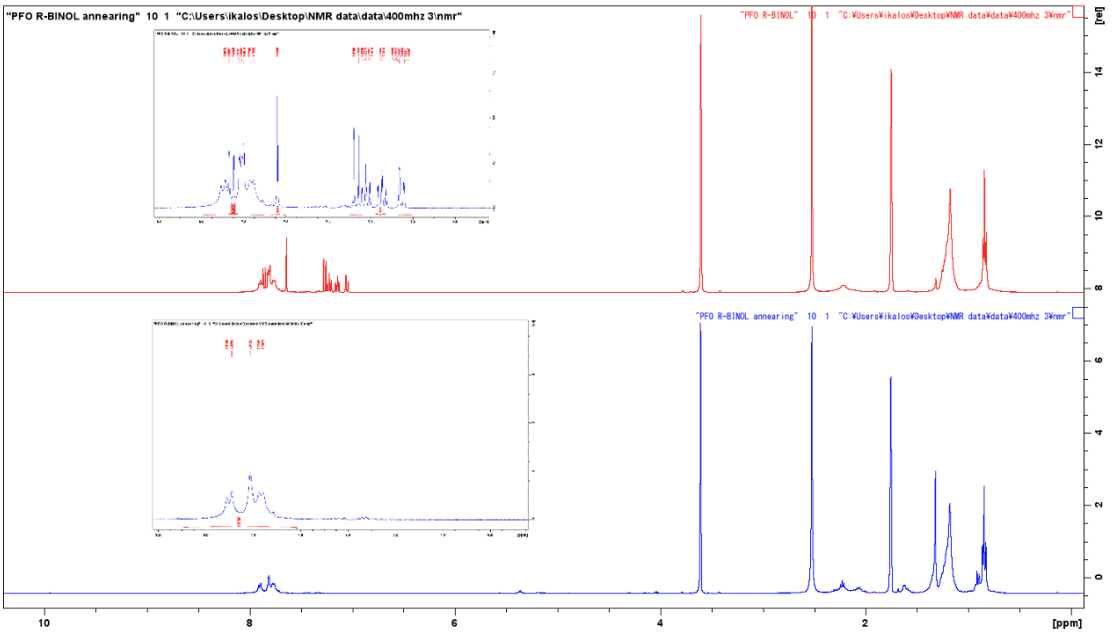

Fig. 4.7 NMR spectra of PFO/BINOL before and after annealing.

Previous chapters have reported that thermal annealing can lead to the sublimation of BINOL in F8BT/BINOL systems. To confirm whether a similar phenomenon occurs

in the PFO/BINOL films, we characterized ^{1}H NMR spectra of drop-cast films before and after annealing at 140 ℃. The characteristic peak of BINOL at approximately 7.3 ppm was observed in the unannealed sample, and it was disappeared completely after annealing. This confirms that BINOL underwent complete sublimation during the annealing process, even in relatively thick films. BINOL showed similar behavior at different matrix, indicating the general performance of high-temperature sublimation.

4.3.2 Effect of crystalline phase transition on PFO/BINOL

It is well known that polyfluorene derivatives can adopt multiple crystalline phases, among which the β-phase exhibits superior chiroptical performance.[106] To investigate whether a similar effect can be observed in PFO/BINOL systems, SVE was applied to induce a phase transition of PFO from α-phase to β-phase. Sample preparation method was illustrated in Chapter 4.2.2, we performed SVE treatment on samples with different annealing temperatures.

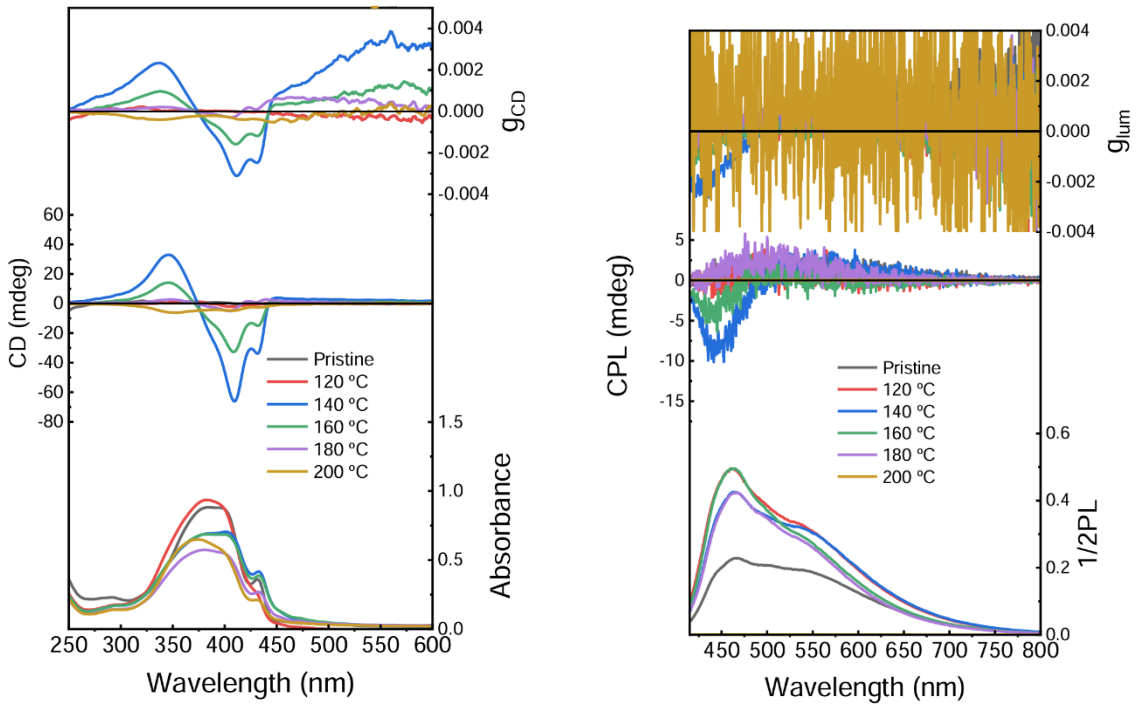

Fig. 4.8 CD and CPL spectra of PFO/BINOL thin films with different annealing temperatures after SVE treatment.

CD and CPL spectra are shown in Fig. 4.8. The emergence of a shoulder peak at around 440 nm in CD spectra is the characteristic β-phase peak of PFO. This phenomenon indicates the successful induction of β-phase PFO. However, the overall g_{CD} value remained very low (~3.0 × 10^{-3}), suggesting limited enhancement from the phase transition.

Similarly, the g_{lum} value remained low after SVE treatment (approximately 2.0 × 10^{-3}), indicating that while the spectral shape changed with β-phase formation, the degree

of circular polarization did not significantly improved.

4.4 Conclusions

In this study, we investigated the chiral induction behavior between PFO and BINOL. Similar to F8BT, PFO could be induced by BINOL after annealing. The optimized concentration of BINOL was 22.8 wt%, the optimized annealing temperature was 140 ℃ and thicker films showed higher g values. NMR also proved BINOL completely sublimated after annealing, left the neat PFO in the films.

To explore the influence of crystalline phase transitions, SVE was used to convert the α-phase to the β-phase of PFO. Although β-phase features were observed in the CD and CPL spectra, the overall g values remained low. Although β-phase didn’t obviously enhance CD or CPL intensity, it can change the CD and CPL spectral shape of PFO.

Chapter 5
Circularly polarized Förster resonance energy transfer (C-FRET) of F8BT induced by BINOL derivatives

5.1 Introduction

CPL and its electroluminescent counterpart (CPEL) have garnered significant attention due to their potential applications. Among the various strategies to achieve CPL, chiral induction remains one of the most widely adopted approaches owing to its simplicity and versatility. However, the realization of red-emitting CPL remains particularly challenging due to the limited availability of suitable chiral red emitters and the tendency for emission quenching at longer wavelengths.

To address this issue, energy transfer mechanisms, particularly Förster resonance energy transfer (FRET), have emerged as a promising pathway. FRET is a non-radiative energy transfer mechanism that occurs between a donor and an acceptor fluorophore through long-range dipole-dipole interactions. Effective energy transfer between donor-acceptor pairs requires the fulfillment of three primary conditions: (1) A substantial spectral overlap between the emission spectrum of the donor and the absorption spectrum

of the acceptor; (2) An appropriate spatial and orientational arrangement of the donor and acceptor molecules; (3) A sufficiently close intermolecular distance, typically within the range of 10–100 Å.

Accordingly, the energy transfer efficiency (E) is strongly dependent on three key factors: the degree of spectral overlap, the relative orientation of the transition dipole moments, and the distance between donor and acceptor. This relationship can be quantitatively described by the Förster theory as follows:

$$E = \frac{R_0^6}{R_0^6 + r^6} \tag{5-1}$$

Here, where R_0 represents the Förster distance, defined as the distance at which the energy transfer efficiency is 50%, and r represents the actual distance between the donor and acceptor centers.

FRET plays a pivotal role in modulating both the emission color and PLQY of composite luminescent systems. By carefully selecting donor-acceptor pairs with suitable spectral overlap, excitation energy can be efficiently transferred from a high-absorption donor to a high-efficiency acceptor, thus tuning the emission wavelength and enhancing the radiative decay pathway.

This energy migration mechanism effectively reduces the probability of non-

radiative recombination at the donor site, especially when the donor has a relatively low PLQY. Simultaneously, it enables the harvesting of excitation energy by acceptor molecules that may otherwise exhibit low absorption cross-sections, enhancing their emission intensity. Furthermore, FRET can help suppress concentration quenching in the donor matrix by delocalizing the excitons, which is particularly beneficial for achieving bright emission in OLEDs. In this chapter, we present a system that integrates chiral and energy transfer simultaneously, referred to as circularly polarized Förster resonance energy transfer (C-FRET). This approach enables the efficient relay of both excitation energy and molecular chirality from a chiral host to a red-emitting guest.

Building on previous success with F8BT/BINOL systems that demonstrated strong green CPEL, we replaced BINOL with a more effective chiral inducer, R5011, which exhibits a stronger chiral induction capability to F8BT. By doping F8BT with 0.75 mol% of the red-emitting molecule DBP, we achieved significant enhancement in chiroptical performance, with the asymmetric factors $|g_{CD}|$ and $|g_{lum}|$ reaching up to 0.2, representing an order-of-magnitude improvement from the 10^{-3} level observed in BINOL systems.

Besides, PLQY of this system was improved compared to F8BT/BINOL system. By adding the chiral inducer 5011, PLQY of F8BT increased from 33% to 42% after

annealing. After doping with the energy acceptor DBP, the PLQY is further increased to 55%. The improvement of PLQY is beneficial to the potential as the emitting layer of CP-OLEDs.

Through this work, we demonstrate that C-FRET is a robust and versatile strategy for realizing high-performance red CPL materials and lay the groundwork for the development of next-generation red CP-OLEDs with tunable chiral and optical properties.

5.2 Experimental section

5.2.1 Materials and instruments

In addition to the materials previously described in Chapter 2, the following materials were used in the film preparation and device fabrication processes throughout the rest of this study. Dibenzo{[f,f']-4,4',7,7'-tetraphenyl}diindeno[1,2,3-cd :1',2',3'-lm]perylene (DBP, sublimed purity > 99%) were purchased from Luminescence Technology Corp. Chiral dopant R/S5011 (GC purity > 98 %) were obtained from Daken Chemical. All materials and reagents were used without further purification.

5.2.2 Sample preparation

F8BT/5011 solutions (10 mg/mL) were prepared with doping concentrations of 5011 ranging from 10 to 50 wt% relative to F8BT. Similarly, F8BT/5011/DBP solutions (10 mg/mL) were prepared by doping DBP at concentrations ranging from 0.25 to 1.5 mol% relative to F8BT. All solutions were stirred at 80 °C for 12 hours to ensure complete dissolution. Thin films were fabricated by spin-coating 100 μL of the prepared solutions onto quartz substrates at 1000 rpm for 90 seconds. The films were subsequently annealed at various temperatures (100–220 °C) using either a hot plate or a laboratory oven to induce structural and morphological changes.

5.2.3 Characterization methods

All characterization instruments and methods were the same as described in Chapter 2.

5.3 Results and discussion

5.3.1 FRET between F8BT and DBP

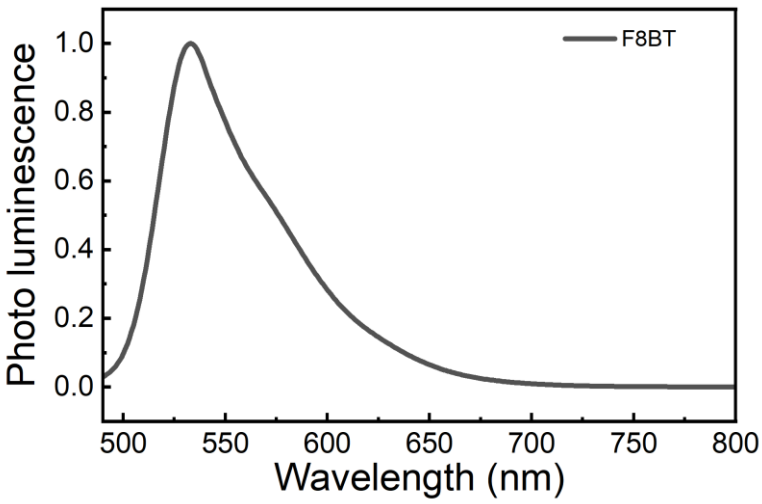

Fig. 5.1 PL spectra of F8BT thin film.

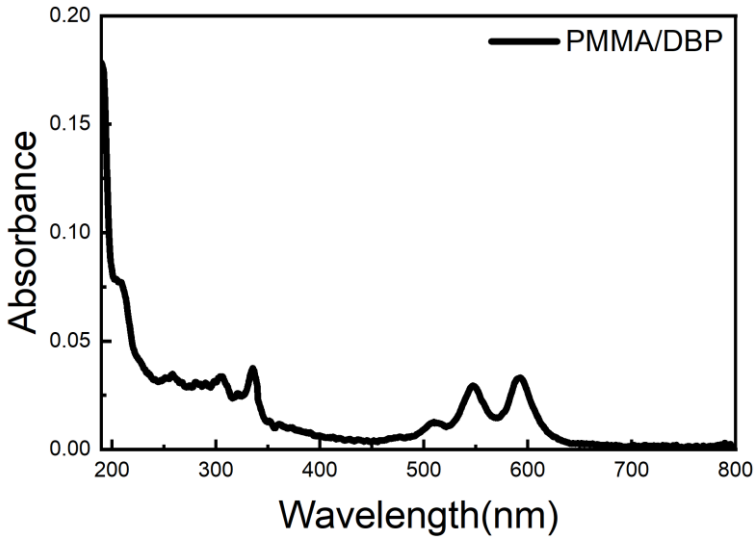

Fig. 5.2 Absorption spectra of DBP/PMMA thin film.

The fundamental basis of C-FRET lies in the well-established FRET mechanism. A

critical precondition for efficient FRET is spectral overlap between the emission spectrum of the donor (host) and the absorption spectrum of the acceptor (guest). This spectral alignment ensures appropriate energy level matching, allowing non-radiative energy transfer via dipole-dipole coupling. In the context of C-FRET, this requirement is manifested as a significant overlap between the fluorescence peak of the chiral donor material and the absorption band of the achiral or chiral acceptor, enabling simultaneous transfer of energy and chirality. The photoluminescence spectrum of F8BT and the absorption spectrum of DBP are shown in Fig.5.1 and Fig.5.2. To investigate the solid-state absorption characteristics of the small-molecule emitter DBP, which is difficult to form uniform films, the compound was doped into a transparent PMMA for spectroscopic characterization. As shown in Fig 5.2, the absorption spectrum of DBP exhibits absorption peaks centered around 550 nm and 600 nm. In comparison, the PL emission peak of F8BT is located at approximately 540 nm. The significant spectral overlap between the emission of F8BT and the absorption of DBP indicates that the system satisfies the fundamental spectral resonance condition for efficient FRET. This alignment confirms that energy transfer from F8BT (donor) to DBP (acceptor) is feasible within the composite system, forming a solid foundation for C-FRET-based circularly polarized emission.

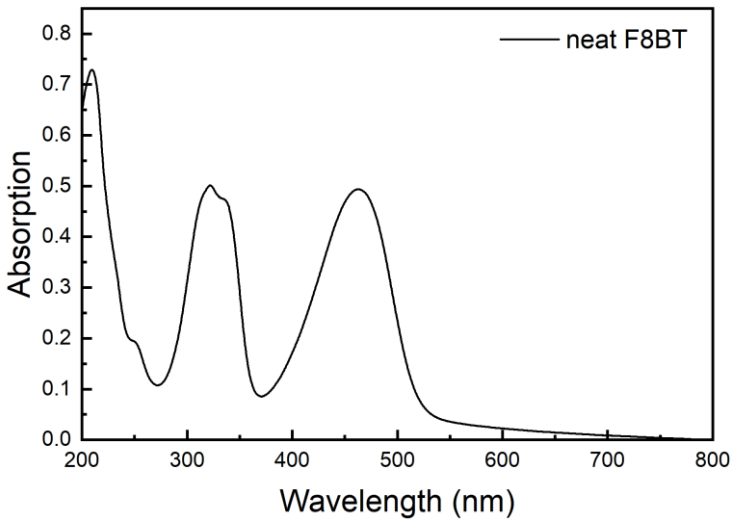

Fig. 5.3 Absorption spectra of F8BT thin film.

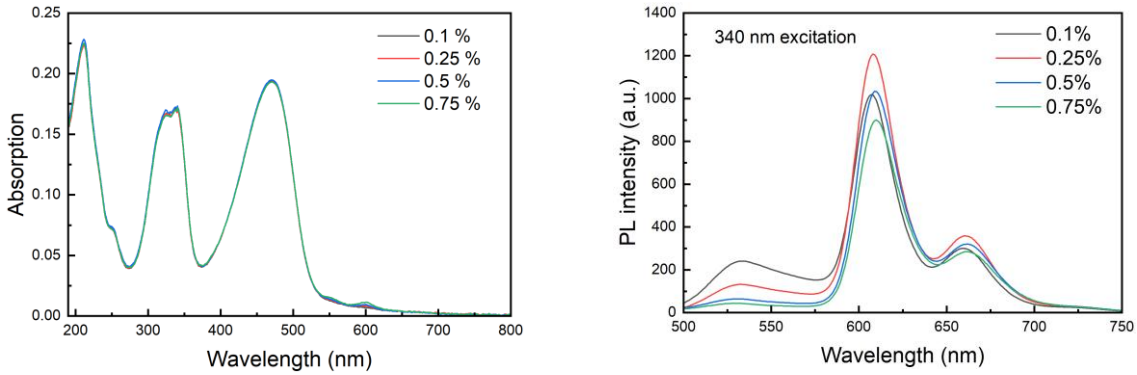

Fig. 5.4 Absorption and PL spectra of F8BT/DBP thin films, the mole ratio of DBP range from 0.1%-0.75%.

Based on the absorption spectrum of F8BT (Fig 5.3), which exhibits two prominent

absorption peaks at 340 nm and 450 nm, these wavelengths were selected as excitation wavelength for F8BT/DBP films. A series of blend films were prepared with DBP molar ratios ranging from 0.1% to 0.75%. The corresponding UV-Vis absorption and PL spectra are shown in Fig 5.4.

As shown in the PL spectra, the emission peak of F8BT at 540 nm progressively decreases with increasing DBP ratio, while new emission peaks emerge at 625 nm and 675 nm, corresponding to the characteristic fluorescence of DBP. This spectral evolution provides clear evidence of FRET from F8BT to DBP.

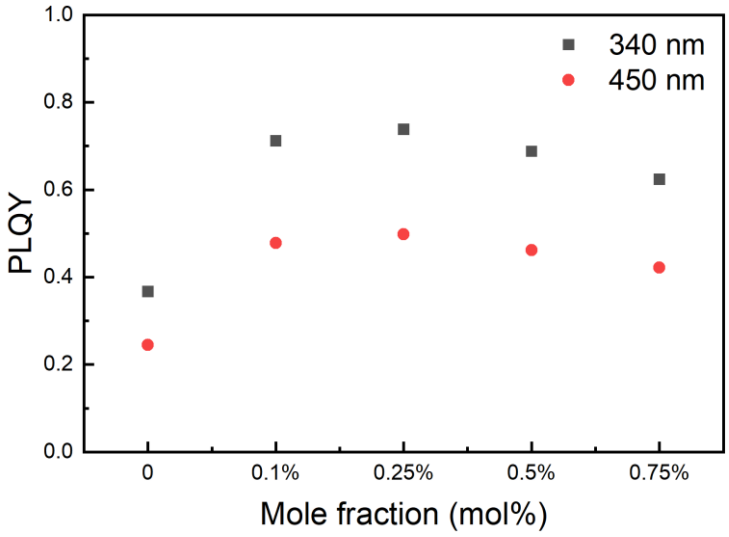

Fig. 5.5 PLQY of F8BT/DBP thin films, the mole ratio of DBP range from 0.1%-0.75%.

PLQY of the blend films were also measured (Fig. 5.5), notably, the sample mixed

0.25% DBP exhibited the highest PLQY (approximately 77%) under 340 nm excitation, which is more than double the value observed for pristine F8BT. This enhancement highlights the beneficial of FRET and optimized dopant concentration.

Table 5.1 The specific mixing ratios of 5011 and DBP to F8BT in thin films, and the annealing condition.

Sample ID	Weight fraction of R5011 (wt%)	Mole fraction of DBP (mol%)	Annealing condition
241218B	30.0	0	150 ℃; 10 min
241218D		0.25	
241218E		0.50	
241218F		0.75	
241218G		1.00	
241218H		1.25	

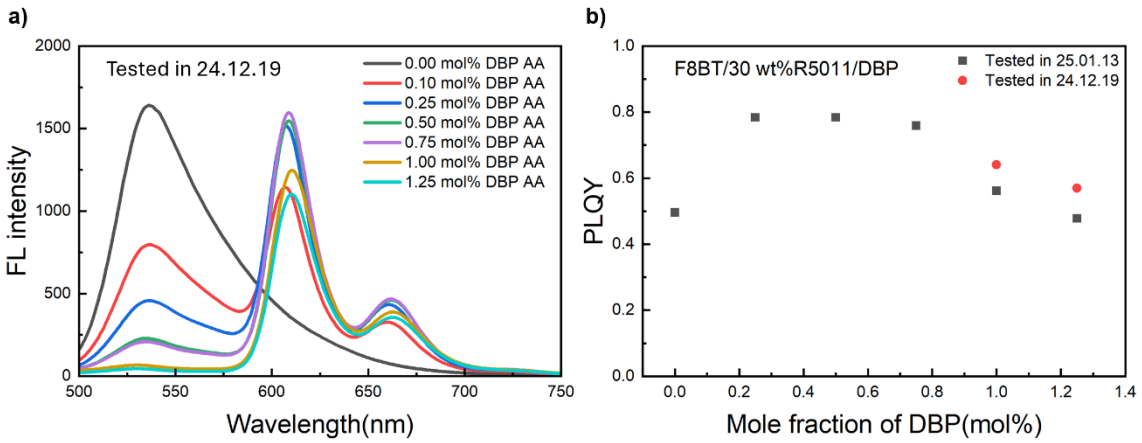

Fig. 5.6 PL spectra and PLQY of F8BT/5011/DBP thin films, the mole ratio of DBP ranges from 0-1.25%.

To verify that the introduction of the chiral inducer 5011 does not interfere with the energy transfer process between F8BT and DBP, we blended 30 wt% of R5011 into the films and carried out PL and PLQY measurements. The results are presented in Fig. 5.6.

In the F8BT/R5011/DBP system, a DBP concentration of 0.75 mol% yielded the strongest red emission, indicating efficient energy transfer was preserved despite the presence of the chiral inducer. However, when the DBP doping level was increased to 1.0 mol%, a significant decrease in PLQY was observed under 340 nm excitation. This reduction is likely due to concentration-induced quenching or phase separation effects. Therefore, in order to achieve high PLQY, which is crucial for realizing high EQE in OLEDs, the optimal DBP doping concentration is determined to be 0.75 mol% in the presence of 5011.

5.3.2 C-FRET between F8BT and DBP

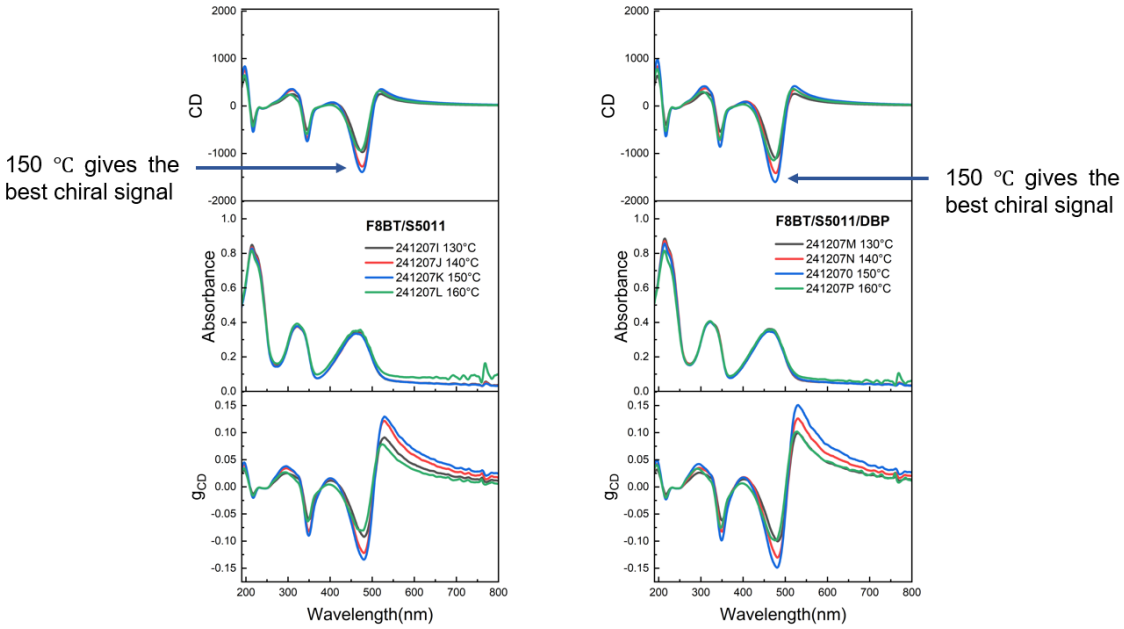

Fig. 5.7 CD spectra of F8BT/5011 and F8BT/5011/DBP thin films after different annealing temperatures.

CD spectra of F8BT/5011 and F8BT/5011/DBP films after annealing at various temperatures are shown in Fig. 5.7. Due to the relatively low doping concentration of DBP (0.75 mol%), the presence or absence of DBP does not significantly affect the overall CD spectral features. Both systems exhibit similar spectral profiles. Importantly, for both F8BT/5011 and F8BT/5011/DBP films, the strongest CD signals were observed after annealing at 150 °C, indicating optimal chiral organization at this temperature. The corresponding g_{CD} in both cases exceeded 0.1, confirming a high degree of induced

chiroptical activity within the polymer matrix.

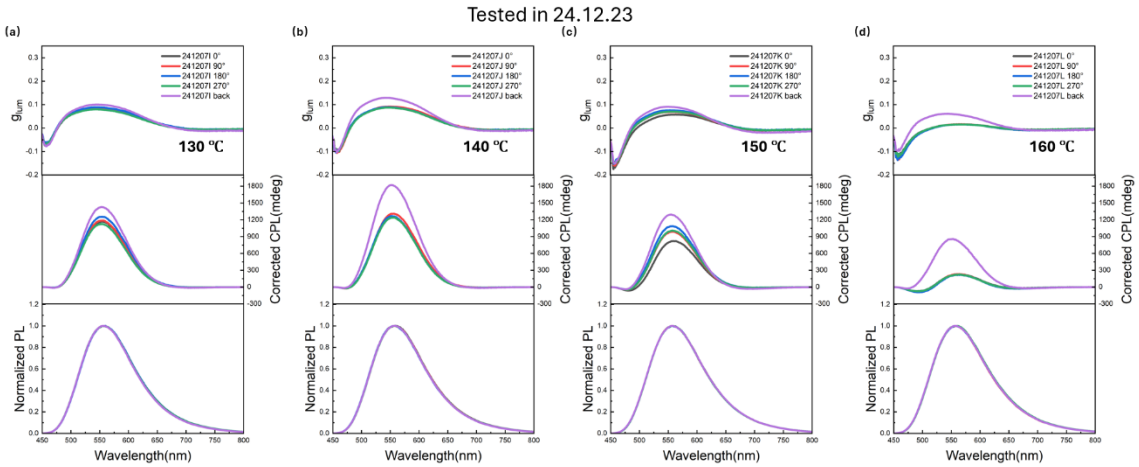

Fig. 5.8 CPL spectra of F8BT/5011 thin films after annealing at different temperatures.

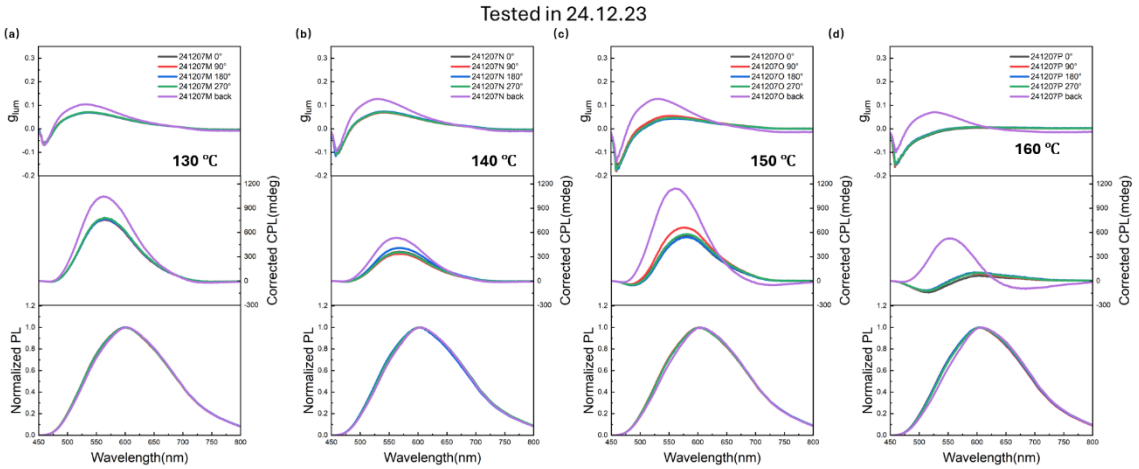

Figure 5.9 CPL spectra of F8BT/5011/DBP thin films after annealing at different temperatures.

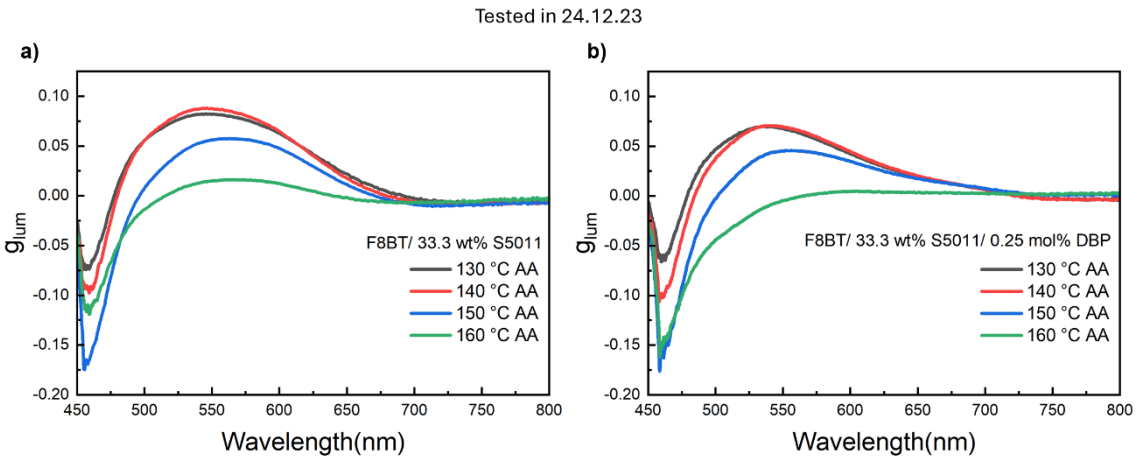

Fig. 5.10 The g_{lum} of F8BT/5011 and F8BT/5011/DBP thin films after annealing at various temperatures.

CPL spectra of F8BT/5011 and F8BT/5011/DBP films annealed at various temperatures are shown in Fig. 5.8 and 5.9. The F8BT/5011 films showed the CPL peak at around 550 nm, corresponded well with the F8BT/BINOL system. The F8BT/5011/DBP films showed the CPL peak at around 600 nm. In contrast to the CD spectra, the CPL spectra of the F8BT/5011/DBP blend films exhibited a distinct red-shift upon DBP doping, providing compelling evidence for the occurrence of C-FRET. The comparison between the CPL and PL spectra reveals that the CPL emission peak is blue-shifted relative to the PL peak, with its maximum intensity located between the emission wavelengths of F8BT and DBP.

This spectral behavior suggests a possible decoupling of chiral and energy transfer dynamics within the system. Specifically, the observation implies that energy transfer from F8BT to DBP is more efficient or complete than the associated chiral transfer, resulting in CPL emission that does not fully coincide with the PL of the final energy acceptor.

Furthermore, analysis of the g_{lum} values across different annealing temperatures revealed that both F8BT/5011 and F8BT/5011/DBP films exhibited their highest asymmetric factors after annealing at 130 °C and 140 °C, respectively. Notably, these optimal temperatures differ from those identified in the CD spectra, where maximum g_{CD} was observed at 150 °C. This difference indicates that the optimal thermal conditions for inducing ground-state chirality (CD) may not necessarily align with those that maximize excited-state chiral emission (CPL), likely due to differences in molecular orientation, aggregation, or exciton dynamics in the emissive state.

5.3.3 Increased PLQY by chiral inducer 5011 and C-FRET

In a previous chapter, we demonstrated that in the F8BT/BINOL system, the sublimation of BINOL at elevated temperatures not only removed the chiral dopant but

also contributed to an enhancement in photoluminescence quantum yield (PLQY). This sublimation behavior is not unique to BINOL but is rather a common characteristic of small-molecule additives. Similarly, the chiral inducer 5011 exhibits sublimation behavior, albeit requiring a higher temperature (~250 °C).

To explore this effect, we prepared both F8BT/5011 and F8BT/5011/DBP blend films and evaluated their PLQYs under three conditions: before annealing, after annealing at 150 °C, and after high-temperature annealing at 250 °C to promote sublimation of 5011. The PLQY results are summarized in Fig 5.11.

Table 5.2 The PLQY of F8BT, F8BT/5011 and F8BT/5011/DBP 5011 films before annealing, after annealing at 150 ℃ and after second annealing at 250 ℃.

Before annealing:

Sample	340 nm	450 nm
F8BT	0.373	0.254
F8BT/R5011	0.465	0.317
F8BT/R5011/DBP	0.813	0.557

First annealing: 150 ℃; 10 min

Sample	340 nm	450 nm
F8BT	0.483	0.335
F8BT/R5011	0.615	0.422
F8BT/R5011/DBP	0.807	0.555

Second annealing: 250 ℃; 5 min

Sample	340 nm	450 nm
F8BT	0.336	0.235
F8BT/R5011	0.342	0.273
F8BT/R5011/DBP	0.627	0.434

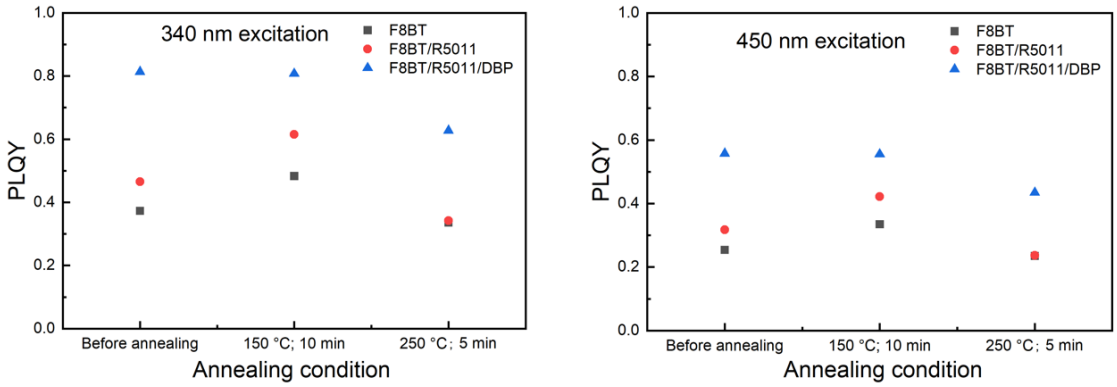

Fig. 5.11 The summarized PLQY of F8BT, F8BT/5011 and F8BT/5011/DBP 5011 films before annealing, after annealing at 150 ℃ and after second annealing at 250 ℃.

Overall, PLQY under 340 nm excitation was consistently higher than that under 450 nm excitation, regardless of processing conditions. Among the three thermal treatments, 150 °C annealing yielded the highest PLQY for all samples. In contrast, high-temperature sublimation at 250 °C led to a marked decrease in PLQY, even falling below the pre-annealed values. Notably, the PLQY of F8BT/5011 was higher than that of pristine F8BT, indicating that 5011 contributes to PL enhancement, potentially through morphological modification or suppression of non-radiative decay.

Following sublimation, the PLQYs of both F8BT/5011 and F8BT/5011/DBP

decreased significantly, suggesting that 5011 not only enhances the intrinsic PL efficiency of F8BT, but also plays a role in facilitating energy transfer from F8BT to DBP. While the exact mechanism behind this PLQY enhancement remains unclear, it is well established that external quantum efficiency (EQE) is generally proportional to PLQY. Therefore, understanding and leveraging this behavior may hold significant implications for the future design and optimization of circularly polarized OLEDs (CP-OLEDs).

5.4 Conclusions

In this chapter, we successfully realized C-FRET in F8BT chiral inducing system, utilizing the small-molecule chiral inducer R5011 and the red-emitting acceptor DBP. The energy and chirality could be simultaneously transferred from the chiral F8BT host to the achiral DBP guest, enabling red CPL emission.

The spectral overlap between the emission of F8BT and the absorption of DBP face the requirement of FRET. When DBP is doped into films, the luminescence intensity of F8BT decreased while the luminescence intensity of DBP increaseed. The optimized DBP doping ratio was identified as 0.75 mol%, which yielded the highest red emission and PLQY in the presence of 30 wt% R5011.

Moreover, CD and CPL spectra revealed successful C-FRET between F8BT and DBP. But the optimized annealing temperatures from CD and CPL spectra showed slightly difference (140 ℃ and 150 ℃). The wavelength difference between CPL and PL spectra suggests a possible decoupling of chiral and energy transfer dynamics within the system.

Importantly, the chiral dopant R5011 not only served as an efficient chirality inducer but also contributed significantly to enhancing the PLQY of both F8BT and F8BT/DBP systems. While sublimation of 5011 at 250 °C resulted in a loss of this enhancement. This PLQY enhancement, in turn, holds direct implications for improving the EQE of future CP-OLED devices.

Chapter 6
Conclusion

This study proposed a new way to realize CP-OLEDs by sublimable chiral inducers to avoid the negative impact of chiral inducers on the device performance.

In chapter 2, we doped the axially chiral small molecule BINOL into thin films of the achiral conjugated polymer F8BT. Upon annealing the films, the CD signal associated with BINOL disappeared and a clear CD signal from F8BT appeared, indicating the induction of chiroptical properties in F8BT. NMR spectra confirmed the complete removal of BINOL by sublimation during annealing, resulting in the formation of pure F8BT films. The red shift of F8BT in absorption spectra and the fibrous morphology in AFM after annealing indicated that the chiroptical properties of F8BT were caused by intermolecular exciton coupling due to aggregation. PLQY of as-prepared F8BT/BINOL films was remarkably low but after annealing it increased to that of pure F8BT films, suggesting that the removal of chiral inducers by high-temperature sublimation realized both high g factor and PLQY simultaneously.

In chapter 3, we applied this thin film to the emitting layer of CP-OLEDs. The device achieved a maximum EQE of 1.20%, The $|g_{EL}|$ of 7×10^{-3} was achieved without any

optimization of the device structures. This study demonstrates for the first time a way to realize CP-OLEDs by sublimable chiral inducers.

In chapter 4, the generality of the sublimation-assisted chiral induction strategy was also investigated. We confirmed that BINOL is capable of inducing CPL not only in F8BT but also in PFO. Compared to F8BT, PFO exhibited a g_{lum} value one order of magnitude lower. In addition, the CPL emission of PFO could be further red-shifted through solvent vapor annealing, which induced the β-phase crystalline structure. Although β-phase didn't obviously enhance CD or CPL intensity, it can change the CD and CPL spectral shape of PFO.

In chapter 5, the chiral F8BT system was further extended to realize C-FRET. By replacing BINOL with a more efficient chiral inducer, R5011, and doping the blend with a red-emitting molecule DBP as both the energy and chirality acceptor, red CPL emission was successfully achieved. Notably, we also discovered that R5011 contributed to a significant enhancement in the PLQY of the films. These studies provide a new method for the preparation of high-efficiency CP-OLEDs.

In summary, the strategy of realizing CPL by thermally removing chiral inducers via sublimation offers a simple, effective, and broadly applicable approach to improving

luminescence efficiency. Its versatility across different polymer hosts and compatibility with solution processing make it a promising candidate for further exploration.

Bibliography

1. Richardson, F. S. & Riehl, J. P. Circularly polarized luminescence spectroscopy. *Chem. Rev.* **77**, 773–792 (1977).

2. Riehl, J. P. & Richardson, F. S. Circularly polarized luminescence spectroscopy. *Chem. Rev.* **86**, 1–16 (1986).

3. Jiang, W. *et al.* Chiral acidic amino acids induce chiral hierarchical structure in calcium carbonate. *Nat. Commun.* **8**, 15066 (2017).

4. Li, Z., Liu, W., Cheng, H., Chen, S. & Tian, J. Spin-selective transmission and devisable chirality in two-layer metasurfaces. *Sci. Rep.* **7**, 8204 (2017).

5. Yao, X., Hu, Y., Cao, B., Peng, R. & Ding, J. Effects of surface molecular chirality on adhesion and differentiation of stem cells. *Biomaterials* **34**, 9001–9009 (2013).

6. Liu, M., Zhang, L. & Wang, T. Supramolecular Chirality in Self-Assembled Systems. *Chem. Rev.* **115**, 7304–7397 (2015).

7. Cameron, R. P., Yao, A. M. & Barnett, S. M. Diffraction gratings for chiral molecules and their applications. *J. Phys. Chem. A* **118**, 3472–3478 (2014).

8. Zhang, J. *et al.* Multiscale deformations lead to high toughness and circularly polarized emission in helical nacre-like fibres. *Nat. Commun.* **7**, 10701 (2016).

9. Carr, R., Evans, N. H. & Parker, D. Lanthanide complexes as chiral probes exploiting circularly polarized luminescence. *Chem. Soc. Rev.* **41**, 7673–7686 (2012).

10. Sánchez-Carnerero, E. M. *et al.* Circularly polarized luminescence by visible-light absorption in a chiral O-BODIPY dye: unprecedented design of CPL organic molecules from achiral chromophores. *J. Am. Chem. Soc.* **136**, 3346–3349 (2014).

11. Kumar, J., Nakashima, T. & Kawai, T. Circularly polarized luminescence in chiral molecules and supramolecular assemblies. *J. Phys. Chem. Lett.* **6**, 3445–3452 (2015).

12. Zhang, Y., Yu, W., Li, H., Zheng, W. & Cheng, Y. Induced CPL-Active Materials Based on Chiral Supramolecular Co-Assemblies. *Chemistry – A European Journal* **29**, e202204039 (2023).

13. Wagenknecht, C. *et al.* Experimental demonstration of a heralded entanglement source. *Nat. Photonics* **4**, 549–552 (2010).

14. Kim, D.-Y. Potential application of spintronic light-emitting diode to binocular vision for three-dimensional display technology. *J. Korean Phys. Soc* **49**, 505 (2006).

15. Heffern, M. C., Matosziuk, L. M. & Meade, T. J. Lanthanide probes for

bioresponsive imaging. *Chem. Rev.* **114**, 4496–4539 (2014).

16. Brandt, J. R., Salerno, F. & Fuchter, M. J. The added value of small-molecule chirality in technological applications. *Nat. Rev. Chem.* **1**, 1–12 (2017).

17. Sang, Y., Han, J., Zhao, T., Duan, P. & Liu, M. Circularly polarized luminescence in nanoassemblies: generation, amplification, and application. *Adv. Mater.* **32**, 1900110 (2020).

18. Nikolova, L. *et al.* Polarization holographic gratings in side-chain azobenzene polyesters with linear and circular photoanisotropy. *Appl. Opt.* **35**, 3835–3840 (1996).

19. Stalder, M. & Schadt, M. Linearly polarized light with axial symmetry generated by liquid-crystal polarization converters. *Opt. Lett.* **21**, 1948–1950 (1996).

20. Wong, K.-L., Bünzli, J.-C. G. & Tanner, P. A. Quantum yield and brightness. *J. Lumin.* **224**, 117256 (2020).

21. Arrico, L., Di Bari, L. & Zinna, F. Quantifying the overall efficiency of circularly polarized emitters. *Chem. – Eur. J.* **27**, 2920–2934 (2021).

22. Tang, C. W. & VanSlyke, S. A. Organic electroluminescent diodes. *Appl. Phys. Lett.* **51**, 913–915 (1987).

23. Hung, L. S. & Chen, C. H. Recent progress of molecular organic

electroluminescent materials and devices. *Mater. Sci. Eng.: R: Rep.* **39**, 143–222 (2002).

24. Geffroy, B., le Roy, P. & Prat, C. Organic light-emitting diode (OLED) technology: materials, devices and display technologies. *Polym. Int.* **55**, 572–582 (2006).

25. Wei, Q. *et al.* Small-molecule emitters with high quantum efficiency: mechanisms, structures, and applications in OLED devices. *Adv. Opt. Mater.* **6**, 1800512 (2018).

26. Forrest, S. r., Bradley, D. d. c. & Thompson, M. e. Measuring the efficiency of organic light-emitting devices. *Adv. Mater.* **15**, 1043–1048 (2003).

27. Shinar, R. & Shinar, J. Light extraction from organic light emitting diodes (OLEDs). *J. Phys.: Photonics* **4**, 32002 (2022).

28. Kim, K.-H. & Kim, J.-J. Origin and control of orientation of phosphorescent and TADF dyes for high-efficiency OLEDs. *Adv. Mater.* **30**, 1705600 (2018).

29. Kim, S.-Y. *et al.* Organic light-emitting diodes with 30% external quantum efficiency based on a horizontally oriented emitter. *Adv. Funct. Mater.* **23**, 3896–3900 (2013).

30. Kim, J.-S., Ho, P. K. H., Greenham, N. C. & Friend, R. H. Electroluminescence emission pattern of organic light-emitting diodes: implications for device efficiency calculations. *J. Appl. Phys.* **88**, 1073–1081 (2000).

31. Furno, M., Meerheim, R., Hofmann, S., Lüssem, B. & Leo, K. Efficiency and rate of spontaneous emission in organic electroluminescent devices. *Phys. Rev. B* **85**, 115205 (2012).

32. Brütting, W., Frischeisen, J., Schmidt, T. D., Scholz, B. J. & Mayr, C. Device efficiency of organic light-emitting diodes: progress by improved light outcoupling. *Phys. Status Solidi (a)* **210**, 44–65 (2013).

33. Zhao, W. *et al.* Rational molecular design for achieving persistent and efficient pure organic room-temperature phosphorescence. *Chem* **1**, 592–602 (2016).

34. Ma, D., Tsuboi, T., Qiu, Y. & Duan, L. Recent progress in ionic iridium(III) complexes for organic electronic devices. *Adv. Mater.* **29**, 1603253 (2017).

35. Chen, J. *et al.* Red/Near-Infrared Thermally Activated Delayed Fluorescence OLEDs with Near 100 % Internal Quantum Efficiency. *Angewandte Chemie* **131**, 14802–14807 (2019).

36. Miwa, T. *et al.* Blue organic light-emitting diodes realizing external

quantum efficiency over 25% using thermally activated delayed fluorescence emitters OPEN. *Scientific Reports* **7**, 1–8 (2017).

37. Greenham, N. C., Friend, R. H. & Bradley, D. D. C. Angular dependence of the emission from a conjugated polymer light-emitting diode: implications for efficiency calculations. *Adv. Mater.* **6**, 491–494 (1994).

38. Tsutsui, T., Yahiro, M., Yokogawa, H., Kawano, K. & Yokoyama, M. Doubling coupling-out efficiency in organic light-emitting devices using a thin silica aerogel layer. *Adv. Mater.* **13**, 1149–1152 (2001).

39. Wei, M.-K. *et al.* Emission characteristics of organic light-emitting diodes and organic thin-films with planar and corrugated structures. *Int. J. Mol. Sci.* **11**, 1527–1545 (2010).

40. Li, M. & Chen, C.-F. Advances in circularly polarized electroluminescence based on chiral TADF-active materials. *Org. Chem. Front.* **9**, 6441–6452 (2022).

41. Zhang, D.-W., Li, M. & Chen, C.-F. Recent advances in circularly polarized electroluminescence based on organic light-emitting diodes. *Chem. Soc. Rev.* **49**, 1331–1343 (2020).

42. Cahn, R. S., Ingold, C. & Prelog, V. Specification of molecular chirality.

Angew. Chem., Int. Ed. Engl. **5**, 385–415 (1966).

43. Dhbaibi, K. *et al.* Achieving high circularly polarized luminescence with push–pull helicenic systems: from rationalized design to top-emission CP-OLED applications. *Chem. Sci.* **12**, 5522–5533 (2021).

44. Wei, Q. *et al.* Conjugation-induced thermally activated delayed fluorescence (TADF): from conventional non-TADF units to TADF-active polymers. *Adv. Funct. Mater.* **27**, 1605051 (2017).

45. Zhang, D.-W. *et al.* D–π*–a type planar chiral TADF materials for efficient circularly polarized electroluminescence. *Mater. Horiz.* **8**, 3417–3423 (2021).

46. Peeters, E. *et al.* Circularly polarized electroluminescence from a polymer light-emitting diode. *J. Am. Chem. Soc.* **119**, 9909–9910 (1997).

47. Kulkarni, C. *et al.* Molecular design principles for achieving strong chiroptical properties of fluorene copolymers in thin films. *Chem. Mater.* **31**, 6633–6641 (2019).

48. Oda, M. *et al.* Circularly polarized electroluminescence from liquid-crystalline chiral polyfluorenes. *Adv. Mater.* **12**, 362–365 (2000).

49. Oda, M. *et al.* Chiroptical properties of chiral substituted polyfluorenes. *Macromolecules* **35**, 6792–6798 (2002).

50. Di Nuzzo, D. *et al.* High Circular Polarization of Electroluminescence Achieved via Self-Assembly of a Light-Emitting Chiral Conjugated Polymer into Multidomain Cholesteric Films. *ACS Nano* **11**, 12713–12722 (2017).

51. Bünzli, J.-C. G. & Piguet, C. Taking advantage of luminescent lanthanide ions. *Chem. Soc. Rev.* **34**, 1048–1077 (2005).

52. Han, J. *et al.* Recent progress on circularly polarized luminescent materials for organic optoelectronic devices. *Adv. Opt. Mater.* **6**, 1800538 (2018).

53. Zhou, Y., Li, H., Zhu, T., Gao, T. & Yan, P. A highly luminescent chiral tetrahedral Eu4L4(L′)4 cage: chirality induction, chirality memory, and circularly polarized luminescence. *J. Am. Chem. Soc.* **141**, 19634–19643 (2019).

54. Liu, D. *et al.* Chiral BINAPO-controlled diastereoselective self-assembly and circularly polarized luminescence in triple-stranded europium(III) podates. *Inorg. Chem.* **57**, 8332–8337 (2018).

55. Lunkley, J. L., Shirotani, D., Yamanari, K., Kaizaki, S. & Muller, G. Extraordinary circularly polarized luminescence activity exhibited by cesium tetrakis(3-heptafluoro-butylryl-(+)-camphorato) Eu(III) complexes in EtOH and CHCl3 solutions. *J. Am. Chem. Soc.* **130**, 13814–13815 (2008).

56. Whitehead, K. S., Grell, M., Bradley, D. D. C., Jandke, M. & Strohriegl,

P. Highly polarized blue electroluminescence from homogeneously aligned films of poly(9,9-dioctylfluorene). *Appl. Phys. Lett.* **76**, 2946–2948 (2000).

57. Yang, Y., da Costa, R. C., Smilgies, D.-M., Campbell, A. J. & Fuchter, M. J. Induction of Circularly Polarized Electroluminescence from an Achiral Light-Emitting Polymer via a Chiral Small-Molecule Dopant. *Advanced Materials* **25**, 2624–2628 (2013).

58. Wan, L. *et al.* Inverting the Handedness of Circularly Polarized Luminescence from Light-Emitting Polymers Using Film Thickness. *ACS Nano* **13**, 8099–8105 (2019).

59. Lee, D.-M., Song, J.-W., Lee, Y.-J., Yu, C.-J. & Kim, J.-H. Control of Circularly Polarized Electroluminescence in Induced Twist Structure of Conjugate Polymer. *Advanced Materials* **29**, 1700907 (2017).

60. Jung, J.-H., Lee, D.-M., Kim, J.-H. & Yu, C.-J. Circularly polarized electroluminescence by controlling the emission zone in a twisted mesogenic conjugate polymer. *J. Mater. Chem. C* **6**, 726–730 (2018).

61. Cheng, J. *et al.* Induction of circularly polarized electroluminescence from achiral poly(fluorene-alt-benzothiadiazole) by circularly polarized light. *J. Mater. Chem. C* **8**, 6521–6527 (2020).

62. Di Nuzzo, D. *et al.* High Circular Polarization of Electroluminescence Achieved via Self-Assembly of a Light-Emitting Chiral Conjugated Polymer into Multidomain Cholesteric Films. *ACS Nano* **11**, 12713–12722 (2017).

63. Yan, H. *et al.* Enhancing hole carrier injection via low electrochemical doping on circularly polarized polymer light-emitting diodes. *J. Mater. Chem. C* **10**, 9512–9520 (2022).

64. Wan, L. *et al.* Highly Efficient Inverted Circularly Polarized Organic Light-Emitting Diodes. *ACS Appl. Mater. Interfaces* **12**, 39471–39478 (2020).

65. Razzell-Hollis, J., Thiburce, Q., Tsoi, W. C. & Kim, J.-S. Interfacial Chemical Composition and Molecular Order in Organic Photovoltaic Blend Thin Films Probed by Surface-Enhanced Raman Spectroscopy. *ACS Appl. Mater. Interfaces* **8**, 31469–31481 (2016).

66. Li, C.-Y. *et al.* Real-time detection of single-molecule reaction by plasmon-enhanced spectroscopy. *Science Advances* **6**, eaba6012 (2020).

67. Zhang, X., Xu, Z., Zhang, Y., Quan, Y. & Cheng, Y. High brightness circularly polarized electroluminescence from conjugated polymer F8BT induced by chiral binaphthyl-pyrene. *J. Mater. Chem. C* **8**, 15669–15676 (2020).

68. Zhang, X., Xu, Z., Zhang, Y., Quan, Y. & Cheng, Y. Controllable

Circularly Polarized Electroluminescence Performance Improved by the Dihedral Angle of Chiral-Bridged Binaphthyl-Type Dopant Inducers. *ACS Appl. Mater. Interfaces* **13**, 55420–55427 (2021).

69. Yuan, C., Eguchi, K. & Murata, H. BINOL induces chirality in polyfluorene-based electroluminescent polymers in solid state. *Jpn. J. Appl. Phys.* **63**, 02SP10 (2023).

70. Jespersen, K. G. *et al.* The electronic states of polyfluorene copolymers with alternating donor-acceptor units. *J. Chem. Phys.* **121**, 12613–12617 (2004).

71. Donley, C. L. *et al.* Effects of packing structure on the optoelectronic and charge transport properties in poly(9,9-di-n-octylfluorene-alt-benzothiadiazole). *J. Am. Chem. Soc.* **127**, 12890–12899 (2005).

72. Zhang, X., Xu, Z., Zhang, Y., Quan, Y. & Cheng, Y. High brightness circularly polarized electroluminescence from conjugated polymer F8BT induced by chiral binaphthyl-pyrene. *J. Mater. Chem. C* **8**, 15669–15676 (2020).

73. Morgenroth, M., Scholz, M., Lenzer, T. & Oum, K. Ultrafast UV–vis transient absorption and circular dichroism spectroscopy of a polyfluorene copolymer showing large chiral induction. *J. Phys. Chem. C* **124**, 10192–10200 (2020).

74. Zhang, X., Xu, Z., Zhang, Y., Quan, Y. & Cheng, Y. Controllable

circularly polarized electroluminescence performance improved by the dihedral angle of chiral-bridged binaphthyl-type dopant inducers. *ACS Appl. Mater. Interfaces* **13**, 55420–55427 (2021).

75. Song, I., You, L., Chen, K., Lee, W.-J. & Mei, J. Chiroptical Switching of Electrochromic Polymer Thin Films. *Advanced Materials* **36**, 2307057 (2024).

76. Song, I. *et al.* Helical polymers for dissymmetric circularly polarized light imaging. *Nature* **617**, 92–99 (2023).

77. Zhao, T. *et al.* Enhanced circularly polarized luminescence from reorganized chiral emitters on the skeleton of a zeolitic imidazolate framework. *Angew. Chem.* **131**, 5032–5036 (2019).

78. Zhang, X., Xu, Z., Zhang, Y., Quan, Y. & Cheng, Y. High brightness circularly polarized electroluminescence from conjugated polymer F8BT induced by chiral binaphthyl-pyrene. *J. Mater. Chem. C* **8**, 15669–15676 (2020).

79. Xie, R. *et al.* Glass transition temperature from the chemical structure of conjugated polymers. *Nat. Commun.* **11**, 893 (2020).

80. Li, S. *et al.* Different phase-dominated chiral assembly of polyfluorenes induced by chiral solvation: axial and supramolecular chirality. *RSC Adv.* **9**, 38257–38264 (2019).

81. Donley, C. L. *et al.* Effects of Packing Structure on the Optoelectronic and Charge Transport Properties in Poly(9,9-di-n-octylfluorene-alt-benzothiadiazole). *J. Am. Chem. Soc.* **127**, 12890–12899 (2005).

82. Jespersen, K. G. *et al.* The electronic states of polyfluorene copolymers with alternating donor-acceptor units. *The Journal of Chemical Physics* **121**, 12613–12617 (2004).

83. Schmidtke, J. P., Kim, J.-S., Gierschner, J., Silva, C. & Friend, R. H. Optical Spectroscopy of a Polyfluorene Copolymer at High Pressure: Intra- and Intermolecular Interactions. *Phys. Rev. Lett.* **99**, 167401 (2007).

84. Albano, G., Pescitelli, G. & Di Bari, L. Chiroptical Properties in Thin Films of π-Conjugated Systems. *Chem. Rev.* **120**, 10145–10243 (2020).

85. Berova, N., Bari, L. D. & Pescitelli, G. Application of electronic circular dichroism in configurational and conformational analysis of organic compounds. *Chem. Soc. Rev.* **36**, 914–931 (2007).

86. Brixner, T., Hildner, R., Köhler, J., Lambert, C. & Würthner, F. Exciton transport in molecular aggregates – from natural antennas to synthetic chromophore systems. *Adv. Energy Mater.* **7**, 1700236 (2017).

87. Wan, L., Shi, X., Wade, J., Campbell, A. J. & Fuchter, M. J. Strongly

Circularly Polarized Crystalline and β-Phase Emission from Poly(9,9-dioctylfluorene)-Based Deep-Blue Light-Emitting Diodes. *Advanced Optical Materials* **9**, 2100066 (2021).

88. Sang, Y. & Liu, M. Hierarchical self-assembly into chiral nanostructures. *Chem. Sci.* **13**, 633–656 (2022).

89. Green, M. M. *et al.* Majority rules in the copolymerization of mirror image isomers. *J. Am. Chem. Soc.* **117**, 4181–4182 (1995).

90. List, N. H., Kauczor, J., Saue, T., Jensen, H. J. A. & Norman, P. Beyond the electric-dipole approximation: a formulation and implementation of molecular response theory for the description of absorption of electromagnetic field radiation. *J. Chem. Phys.* **142**, 244111 (2015).

91. Wade, J. *et al.* Natural optical activity as the origin of the large chiroptical properties in π-conjugated polymer thin films. *Nat Commun* **11**, 6137 (2020).

92. Yu, C.-J. *et al.* Circularly Polarized Emission from Mixture of Vacuum-Evaporated Mesogenic Luminophores. *Advanced Optical Materials* **10**, 2101674 (2022).

93. Lee, J. *et al.* Modification of an ITO anode with a hole-transporting

SAM for improved OLED device characteristics. *J. Mater. Chem.* **12**, 3494–3498 (2002).

94. Liu, S. *et al.* Efficient ITO-free organic light-emitting devices with dual-functional PSS-rich PEDOT:PSS electrode by enhancing carrier balance. *J. Mater. Chem. C* **7**, 5426–5432 (2019).

95. Salsberg, E. & Aziz, H. Degradation of PEDOT:PSS hole injection layers by electrons in organic light emitting devices. *Org. Electron.* **69**, 313–319 (2019).

96. Nardes, A. M. *et al.* Conductivity, work function, and environmental stability of PEDOT:PSS thin films treated with sorbitol. *Org. Electron.* **9**, 727–734 (2008).

97. Mucur, S. & TekiN, E. Annealing effect of gold thin films on the light output performances of organic light emitting diodes. *Turk. J. Phys.* **42**, 1–12 (2018).

98. Lee, S., Lee, B. R., Kim, J.-S. & Song, M. H. Combination effect of polar solvent treatment on ZnO and polyfluorene-based polymer blends for highly efficient blue-based hybrid organic–inorganic polymer light-emitting diodes. *J. Mater. Chem. C* **2**, 8673–8677 (2014).

99. Zhang, H. *et al.* Polarized red, green, and blue light emitting diodes

fabricated with identical device configuration using rubbed PEDOT:PSS as alignment layer*. *Chin. Phys. B* **28**, 78108 (2019).

100. Zhang, Q. *et al.* Concurrent optical gain optimization and electrical tuning in novel oligomer:polymer blends with yellow-green laser emission. *Adv. Sci.* **6**, 1801455 (2019).

101. Heil, H. *et al.* Mechanisms of injection enhancement in organic light-emitting diodes through an Al/LiF electrode. *J. Appl. Phys.* **89**, 420–424 (2001).

102. Wu, C.-I., Lee, G.-R. & Pi, T.-W. Energy structures and chemical reactions at the Al/LiF/Alq3 interfaces studied by synchrotron-radiation photoemission spectroscopy. *Appl. Phys. Lett.* **87**, 212108 (2005).

103. Ofuonye, B. *et al.* Electrical and microstructural properties of thermally annealed Ni/Au and Ni/Pt/Au schottky contacts on AlGaN/GaN heterostructures. *Semicond. Sci. Technol.* **29**, 95005 (2014).

104. Yamashita, D., Ishizaki, A. & Yamamoto, T. In situ measurements of work function of indium tin oxide after UV/ozone treatment. *Mater. Trans.* **56**, 1445–1447 (2015).

105. Park, J. H. *et al.* Characteristics of transparent encapsulation materials for OLEDs prepared from mesoporous silica nanoparticle-polyurethane acrylate resin

composites. *Composites, Part B* **175**, 107188 (2019).

106. Shi, X. *et al.* Relating chain conformation to the density of states and charge transport in conjugated polymers: the role of the $\ensuremath{\beta}$-phase in poly(9,9-dioctylfluorene). *Phys. Rev. X* **9**, 21038 (2019).

Acknowledgements

This doctoral study would not be possible without the help from a lot of peoples. I would like to express my deepest gratitude for them.

First, I would like to express my deepest gratitude to my supervisor Murata sensei, for his continuous support and invaluable guidance throughout my doctoral study. From my application to JAIST and scholarship preparation, to experimental design, conference presentations, and journal publications. His attitude toward scientific research has deeply influenced me and taught me the importance of responsibility and honesty in academia.

I am also grateful to Eguchi sensei for his support in experiments and laboratory management. I want to say thank you to my sub supervisor Okeyoshi sensei and my minor research supervisor Yamaguchi sensei, for their valuable guidance and help throughout my graduation process. Besides, I would like to thank Ikai sensei from Nagoya University and Nishimura sensei from Kanazawa University for their generous support in CPL measurements.

My sincere appreciation also goes to my colleagues and friends: Zhang, Hu, Abe, and Sun, for their helpful discussions and assistance during experiments. Their collaboration and friendship have made my research journey more smoothly and enjoyable.

Beyond academia, I am deeply thankful to my parents and friends for their encouragement and emotional support, especially during times of difficulty and self-doubt. Most of all, I would like to express my heartfelt gratitude and love to my girlfriend, Yitong Yao, who has stood by me unconditionally through every stage of this journey. Despite the challenges of such a long-distance relationship, her presence has been my greatest source of strength. I truly believe that we will walk through life together.

Published Journal Papers

[1] **Chenyuhe Yuan**, Keitaro Eguchi, Hideyuki Murata*, “BINOL induces chirality in polyfluorene-based electroluminescent polymers in solid state”, *Japanese Journal of Applied Physics*, **63** 02SP10, December 2023.

[2] **Chenyuhe Yuan**, Miyu Abe, Haoran Sun, Keitaro Eguchi, Tomoyuki Ikai, Hideyuki Murata*, “Chiral induced circularly polarized luminescence with the removal of chiral inducer through sublimation”, (In preparation)

Conferences

1. MRS 2024 Fall Meeting **(December 2024)**

   Poster presentation

   "Efficiency Enhancement of Circularly Polarized Electroluminescence by Eliminating Chiral Inducers".

   Chenyuhe Yuan, Miyu Abe, Haoran Sun, Tomoyuki Ikai, Keitaro Eguchi and Hideyuki Murata*

2. 34th International Symposium on Chirality (Chirality 2024) **(August 2024)**

   Poster presentation

   "Achieving Circularly Polarized Electroluminescence by Sublimable Chiral Inducers".

   Chenyuhe Yuan, Miyu Abe, Haoran Sun, Tomoyuki Ikai, Keitaro Eguchi and Hideyuki Murata*

3. The 11th International Conference on Molecular Electronics & Bioelectronics (M&BE11) **(June 2024)**

   Oral presentation

"High Efficiency Circularly Polarized Luminescence Derived from Removing Chiral Inducer".

Chenyuhe Yuan, Miyu Abe, Tomoyuki Ikai, Keitaro Eguchi and Hideyuki Murata*

4. 19th International Conference on Chiroptical Spectroscopy (CD 2023) (**September 2023**)

   Poster presentation

   "Axially chiral small molecules induce chirality in polyfluorene-based electroluminescent polymers in solid state".

   Chenyuhe Yuan, Keitaro Eguchi and Hideyuki Murata*

5. The 9th International Symposium on Organic and Inorganic Electronic Materials and Related Nanotechnologies (EM-NANO 2023) (**June 2023**)

   Poster presentation

   "Axially chiral small molecules induce chirality in polyfluorene-based electroluminescent polymers in solid state".

   Chenyuhe Yuan, Keitaro Eguchi and Hideyuki Murata*